

Techno-Economic Optimization of Liquid Hydrogen Refueling Station for Heavy-Duty Transportation

by

Shardul Vikram Singh

A thesis submitted in partial fulfillment
of the requirements for the degree of

Master of Science

Mechanical Engineering

at the

University of Wisconsin- Madison

2025

Date of Final Oral Exam: December 17, 2025

Final Oral Committee:

Luca Mastropasqua, Mechanical Engineering

Franklin Miller, Mechanical Engineering

Mike Wagner, Mechanical Engineering

© Copyright by Shardul Vikram Singh 2025

All rights reserved.

Acknowledgements

I would first like to express my deepest gratitude to my advisor, Dr. Luca Mastropasqua, for his constant guidance, patience, and support throughout this work. His technical insight, high standards, and encouragement have shaped not only this thesis but also the way I think about research and engineering. I am especially grateful that he believed in me from the beginning, trusted me with this project, and gave me the freedom to explore my ideas while always providing steady and thoughtful direction when I needed it. I am also thankful for the opportunities he provided to present and discuss this research at conferences and technical meetings, which greatly broadened my perspective and confidence as a young researcher. The time he invested in detailed feedback, one-on-one meetings, and long technical conversations has had a lasting impact on both this thesis and my growth as an engineer.

I would also like to sincerely thank my thesis committee members, Dr. Franklin Miller and Dr. Mike Wagner, for their time, thoughtful feedback, and valuable suggestions. Their perspectives and comments helped strengthen the technical quality and clarity of this work.

I would also like to sincerely thank my sponsor, Plug Power Inc., for supporting this work and providing the opportunity to engage with problems of direct industrial relevance. I am grateful to Luke Wentlent and Rohit Singla for their mentorship, valuable feedback, and continuous support during my time as a Graduate Research Assistant. Their practical insights and encouragement significantly contributed to the direction and impact of this research.

I am profoundly thankful to my family, whose unconditional love, sacrifices, and belief in me have made this journey possible. Their support emotionally and morally has been my anchor during the most demanding phases of this work. I also want to thank my friends for standing by me, listening to my ideas and problems, and reminding me to maintain balance and perspective.

I would like to acknowledge the HERD Lab and all its lab members for creating a collaborative and motivating research environment. The discussions, shared challenges, and informal problem-solving sessions have all contributed in meaningful ways to this thesis. Working alongside such dedicated and talented colleagues has been both inspiring and enjoyable.

Finally, I am grateful to the Department of Mechanical Engineering at the University of Wisconsin-Madison for providing excellent coursework, facilities, and an intellectually stimulating environment that enabled this research. The support from faculty and staff has been instrumental in my academic and professional growth during my time here.

Contents

List of Figures

List of Tables

Nomenclature

Abstract

1. Introduction
 - 1.1. Transportation Sector and decarbonization challenges
 - 1.2. Hydrogen Properties
 - 1.3. Hydrogen as Fuel
 - 1.4. Fuel Cell Electric Vehicles
 - 1.5. Hydrogen Refueling Protocols
 - 1.6. Hydrogen Refueling Infrastructure
 - 1.7. High Pressure Gaseous Hydrogen Tanks
 - 1.8. Electrolytic Hydrogen Production
 - 1.9. Optimization for Hydrogen Stations
 - 1.10. Challenges
 - 1.11. Objectives
2. Systems Components and Modelling
 - 2.1. Assumptions
 - 2.2. PEM Electrolyzer
 - 2.3. Hydrogen Liquefaction
 - 2.4. 2-phase Cryogenic Storage
 - 2.5. Cryogenic Hydrogen Pumps
 - 2.6. Compressors
 - 2.7. Energy Modelling
3. Optimization Model
 - 3.1. MILP and Solver
 - 3.2. Methodology
 - 3.3. Decision Variables
 - 3.3.1. Binary decision variables
 - 3.3.2. Continuous decision variables
 - 3.3.3. Continuous design variables
 - 3.4. Constraints
 - 3.5. Capacity Factor
 - 3.6. Capital and Operating Cost (CAPEX & OPEX) Modeling

3.7. Objective Function

4. Results and Discussion

4.1. Vehicle Arrival and Variable Station Demand

4.2. PEM Electrolyzer Hydrogen Production

4.3. H2Fills Vehicle Tank Refueling Simulation

4.4. Cryogenic Tank Modelling Results

4.5. Linear fits for the cryogenic tank

4.6. Subsystem 1 Optimization - Dispensing

4.6.1. With main pump and main compressor

4.6.2. Sensitivity analysis of objective weightage

4.6.3. With main pump and no main compressor

4.6.4. Optimization results

4.7. Subsystem 1 and 2 Optimization

4.7.1. Steady grid with Solar

4.7.2. Grid Outage with Solar

4.7.3. Optimization results

4.8. Economic Analysis

5. Conclusions

6. Future Work

6.1. Variable vehicle SOC modelling

6.2. Multi-stage Buffer storage

6.3. Data driven convex optimization - Cryogenic tank

References

Appendix

List of Figures


Figure 1. Medium and Heavy-Duty Vehicle market segmentation by vehicle class.....	13
Figure 2. Energy density comparison of hydrogen with other common gases and liquids.[7]	15
Figure 3. Hyundai Xcient North America Specifications.....	16
Figure 4. Allowable SOC as per pressure and temperature of vehicle tank during refueling.[13]17	
Figure 5. PV-Grid Integrated Liquid Hydrogen Refueling Station for 700 bar heavy-duty vehicle refueling	23
Figure 6. PEM Electrolyzer Balance of Plant Simulink Model. [31].....	25
Figure 7. Simplified diagram of simple Claude based hydrogen liquefaction process with critical para-hydrogen properties. [30].....	27
Figure 8. Simple illustration showing the mass and energy conservation for a 2-phase cryogenic hydrogen. Modified from [34]	29
Figure 9. (a) Isentropic efficiency and evaporation loss [35] (b) Specific work consumption for different cryogenic pumps and mass flowrates under different delivery pressures.[36]	31
Figure 10. Cryogenic pump boil-off and station size curve fitting for 350 and 700 bar dispensing. Produced using experimental data from [38]	32
Figure 11. Boil-off contribution from cryogenic pump mechanisms for 350 bar refueling. [38].	33
Figure 12.(a) HRS component cost contribution. (b) LCOH comparison for pump and compressor based stations for low and high station demand. [16].....	34
Figure 13. Hourly vehicle refueling count and cumulative hydrogen station demand	50
Figure 14. Gaseous hydrogen production rate from 1MW PEM electrolyzer following the hourly solar power variable input.	51
Figure 15. NREL single tank HRS detailed model schematic from H2Fills simulation.....	52
Figure 16. Hydrogen Mass flow rate and Temperature for Vehicle Tank Refilling from H2Fills.	53
Figure 17. Hydrogen Vehicle Tank Pressure, State of Charge and Precooling Energy requirement for Refilling from H2Fills	53
Figure 18. Temperature transition of liquid, vapor and interface film in the cryogenic tank.....	54
Figure 19. (a)Vapor and liquid specific internal energy (b) Tank Pressure (c) Liquid Hydrogen mass (d) Vapor mass from the cryogenic tank simulation.....	55
Figure 20. Multiple linear regression: cryogenic tank pressure, vapor mass and liquid mass	57
Figure 21. Case 1: (a) Liquid and vapor mass impact on cryogenic tank pressure. (b) Optimized Main pump and compressor flow rates. (c) 900 bar buffer tank mass and pressure dynamics. (d) Stacked plot showing electrical power demand for each dispensing component.....	58
Figure 22. Objective function weight comparison for relative CAPEX and energy demand for case 1.....	60
Figure 23. Case 2: (a) Liquid and vapor mass impact on cryogenic tank pressure. (b) Optimized Main pump and vent valve flow rates. (c) 900 bar buffer tank mass and pressure dynamics. (d) Stacked plot showing electrical power demand for each dispensing component.....	62

Figure 24. CAPEX contribution of dispensing components and comparison of cases 1 and 2. ...	64
Figure 25. System electrical power supply with intermittent solar supply and steady grid with varying cost.....	65
Figure 26.(a) System electrical power supply with intermittent solar supply and 1 hour grid outage with daily varying cost. (b) Electrolyzer mass flow split between 350 bar buffer tank and liquefier. (c) Buffer tank mass and pressure dynamics.....	67
Figure 27. Total Plant CAPEX comparison for (pump-only case) for steady grid and grid outage cases.	68
Figure 28. Levelized cost of hydrogen (LCOH) for steady grid case and contribution of CAPEX and OPEX.	70
Figure 29. Variable initial vehicle tank pressure and SOC modelling.....	74
Figure 31. CEPCI values change with time	81
Figure 32. SAE protocol lookup table for vehicle refueling pressure ramp rate. [54]	82

List of Tables

Table 1. Gaseous and Liquid Hydrogen Properties	14
Table 2. 700 bar Hydrogen Refueling Protocol as per SAEJ2601-2.....	17
Table 3. List of modelling assumptions for each HRS component	23
Table 4. List of binary decision variables for MILP optimization.....	40
Table 5. List of continuous decision variables for MILP optimization.	40
Table 6. List of continuous design decision variables for MILP optimization.....	41
Table 7. H2Fills modelling input parameters for HRS.....	52
Table 8. H2Fills modelling input parameters for vehicle tank.....	52
Table 9. The key inputs for the 2-phase cryogenic storage tank model	54
Table 10. Key design optimization results for cases 1 and 2.	63
Table 11. Key operational optimization results for case 1 and 2.....	63
Table 12. Key hydrogen production design optimization results for steady grid and outage cases.	68
Table 13. Economic parameters considered for the LCOH calculations.....	69
Table 14. Multilinear regression relations for vapor mass and pressure with change in liquid mass and inlet/outlet flow rates	75

Nomenclature

t	Time step (minutes)
xx_{pp}	Main cryogenic pump ON/OFF state
xx_{cc}	Main compressor ON/OFF state
$oorn_{pp}$	Pump start-up flag
$oorn_{pp}$	Pump shut-down flag
$oorn_{cc}$	Compressor start-up flag
$oorn_{cc}$	Compressor shut-down flag
zz_{cc}	Electrolyzer to 350-bar buffer flow ON/OFF
\dot{m}_{pp}	Pump mass flow rate (kg/s)
\dot{m}_{cc}	Compressor mass flow rate
\dot{m}_{EEEE}	Hydrogen production rate from electrolyzer (kg/s)
\dot{m}_{EEEEEE}	Electrolyzer mass flow routed to liquefier (kg/s)
\dot{m}_{EEEEEE}	Electrolyzer mass flow routed to 350-bar buffer (kg/s)
\dot{m}_{EEEE}	Flow from 350-bar buffer to liquefier (kg/s)
$\dot{m}_{EEEELLLLLLLLLLLL}$	Liquefier design mass-flow rate (kg/s)
\dot{m}_{boil}	Boil-off mass flow in the cryogenic tank
$\dot{m}_{DLLLLDDDDDDDD}$	Station dispensing flow required by refueling events (kg/s)
MM_{350}	Mass in 350-bar buffer tank (kg)
MM_{900}	Mass in 900-bar buffer tank (kg)
MM_{liq}	Liquid hydrogen mass in cryogenic tank (kg)
MM_{vap}	Vapor hydrogen mass in cryogenic tank (kg)
$MM_{liq,0}$	Initial liquid inventory in cryogenic tank (kg)
MM_{tank}	Cryogenic tank nameplate capacity (kg)
TT	Temperature (K)
$MM_{900, min}, MM_{900, max}$	Usable mass bounds in 900-bar buffer (kg)
PP_{tank}	Cryogenic tank pressure (psi)
$PP_{min, tank}, PP_{max, tank}$	Cryogenic tank pressure band (psi)
$PP_{DLLLLDD,900}, PP_{DDDDmm,900}$	900-bar buffer pressure window (bar)
$PP_{DLLLLDD,350}, PP_{DDDDmm,350}$	350-bar buffer pressure window (bar)
$PP_{ssLLcc,ccccDDpp}, PP_{DLLLLss,ccccDDpp}$	Compressor suction/discharge pressures (bar)
$PP_{ssLLcc,ppLLDDpp}, PP_{DLLLLss,ppLLDDpp}$	Pump suction/discharge pressures (bar)
ee	Electrolyzer electrical input (MW)
EE	Electrolyzer nameplate capacity (MW)
pp_{SS}^{DDaa}	Solar PV power available (MW)
pp_{SS}	Solar PV power used (MW)
pp_{GG}	Grid power used (MW)
	Grid capacity (MW)
pp_{HRS}	Total HRS electrical load (MW)
pp_{pump}	Pump power (MW)
pp_{boost}	Booster compressor power (MW)
pp_{comp}	Main compressor power (MW)
$pp_{ppLLDDpp,tiLL}$	Transfer pump power (MW)

PPE	Liquefier electrical power (MW)
$P_{vap}P$	Pump-line vaporizer power (MW)
$P_{vap}C$	Compressor-line vaporizer power (MW)
V_{350}	350-bar buffer tank volume (m ³)
V_{900}	900-bar buffer tank volume (m ³)
$cccp_{cc}$	Compressor nameplate capacity (kg/s)
$cccp_{pp}$	Pump nameplate capacity (kg/s)
r_{pp}, r_{cc}	Ramp fraction per minute pump, compressor
w	Specific work (J/kg)
ρ_{H_2}	Hydrogen density (kg/ m ³)
η	Efficiency
h	Specific enthalpy (J/kg)
s	Specific entropy (J/kg·K)
CC	Cost terms (component CAPEX, OPEX terms in objective)
CF	Capacity Factor

Acronyms

HRS	Hydrogen Refueling Station
FCEV	Fuel Cell Electric Vehicle
PEM	Proton Exchange Membrane
MILP	Mixed Integer Linear Programming
PV	Photovoltaic
CAPEX	Capital Expenditure
OPEX	Operating Expenditure
LCOH	Levelized Cost of Hydrogen
DOE	U.S. Department of Energy
NREL	National Renewable Energy Lab
LH ₂	Liquid Hydrogen
CGH ₂	Compressed Gaseous Hydrogen
MPa	Megapascal
TPD	Tons per Day
SOC	State of Charge
REFPROP	NIST Reference Thermophysical Properties database
MEA	Membrane Electrode Assembly
GDL	Gas Diffusion Layer
PBU	Pressure Build-Up unit
ToU / ToD	Time-of-Use / Time-of-Day
HDPE	High-Density Polyethylene
GHG	Greenhouse Gas
CO ₂	Carbon Dioxide
SEC	Specific Energy Consumption (kWh/kg)
HDSAM	Hydrogen Delivery Scenario Analysis Model
CEPCI	Chemical Engineering Plant Cost Index

Abstract

The decarbonization of heavy-duty transportation remains a critical challenge in achieving global net-zero targets due to high energy demands and limited zero-emission alternatives. Hydrogen fuel cell vehicles (FCEVs) offer a promising solution, but widespread adoption is constrained by the cost, complexity, and reliability of hydrogen refueling infrastructure. This thesis develops a techno-economic optimization framework for a fully integrated liquid hydrogen refueling station (HRS) that combines grid electricity with on-site renewable hydrogen production via PEM electrolysis liquefaction, cryogenic storage, and 700-bar dispensing. A mixed-integer linear programming (MILP) model is formulated to co-optimize equipment sizing and operational scheduling under realistic constraints, minimizing energy consumption, boil-off losses, and capital expenditure while ensuring reliable hydrogen delivery.

The proposed system architecture is evaluated through detailed component modeling and optimization across two configurations: pump plus compressor and pump-only dispensing. Results indicate that a pump-only design achieves comparable throughput with 7.2% lower CAPEX and 3.1% lower energy demand, with modest venting losses. PEM electrolyzer and Liquefaction dominates energy consumption, highlighting the need for efficiency improvements. Economic analysis using discounted cash-flow methods yields a Levelized Cost of Hydrogen (LCOH) of \$9.34/kg at 2 metric tons per day, aligning with DOE and NREL projections for near-term heavy-duty hydrogen infrastructure. The optimized design demonstrates high-capacity factors (>97%) and operational resilience under grid outages through strategic buffer storage management. These findings establish a pathway for cost-effective, self-sustaining hydrogen refueling hubs that reduce supply-chain dependence and enable scalable deployment for heavy-duty transportation.

Chapter 1. Introduction

1.1. Transportation Sector and decarbonization challenges

The transport sector is a central pillar of the global energy system and a major driver of greenhouse gas (GHG) emissions. Recent reports indicate that transport-related CO₂ emissions rebounded strongly after the COVID-19 pandemic and reached around 7.7 gigatons (Gt) CO₂ again in 2021. The transport sector contributes around 15% of total global greenhouse gas emissions with around 72% coming from road transport (~ 10% of global GHG emissions). [1] [2]

Despite increasing policy attention, decarbonizing the transport sector remains one of the most challenging elements of the global net-zero transition. Some reports show that to align with goals of limiting global temperature rise of 1.5 °C , transport CO₂ emissions must peak immediately and decline rapidly. [3] Recent work on “hard-to-abate” sectors lists heavy duty road transportation, shipping, and aviation alongside iron and steel and chemicals as sectors that collectively account for around one-fifth of global CO₂ emissions and face particularly high abatement costs and technology uncertainties. Heavy duty transportation trucks have around 9% share of global vehicles yet they are responsible for around a quarter of total transportation CO₂ emissions. [4]

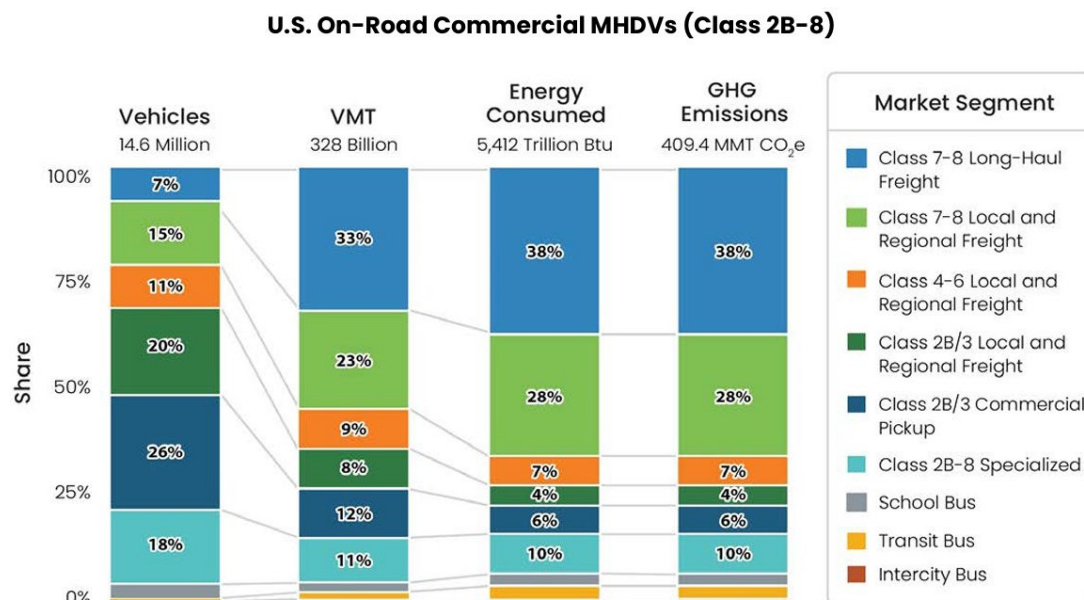


Figure 1. Medium and Heavy-Duty Vehicle market segmentation by vehicle class.

Figure 1 summarizes the distribution of vehicles, vehicle-miles traveled (VMT), energy consumption, and greenhouse gas (GHG) emissions across U.S. commercial medium- and heavy-duty vehicle (MHDV) classes.[5] The most important fact shown is the dominance of Class 7-8 long-haul freight trucks, which represent only 7% of the vehicle stock, yet contribute 33% of total VMT, 38% of total energy consumption, and 38% of total GHG emissions. This highlights the intensive duty cycle and fuel use of long-haul freight operations. Similarly, Class 7-8 local and

regional freight trucks account for 15% of vehicles but contribute 28% of energy use and emissions.

These analysis underscores why heavy-duty trucking is a primary target for hydrogen fuel-cell electrification and other zero-emission technologies, since decarbonizing even a small share of these vehicles produces outsized reductions in national transportation emissions.

1.2. Hydrogen Properties

Hydrogen possesses several unique thermophysical and energetic properties that distinguish it from conventional fuels. At ambient conditions (20°C, 1 atm), hydrogen is a colorless, odorless, non-toxic, and highly combustible diatomic gas with exceptionally low molecular weight (2.016 g/mol). Its small size and high mobility result in a diffusion rate of roughly 0.61 cm²/s, which is almost an order of magnitude higher than many hydrocarbon gases. This rapid diffusivity enables fast dispersion in the event of a leak, contributing positively to safety, although it also makes high-integrity containment essential.

Table 1. Gaseous and Liquid Hydrogen Properties.

Properties	CGH2	CGH2	LH2
Pressure [bar]	350	700	1
Temperature [K]	298	298	20.3
Volumetric density [kg/m ³]	23.2	39.2	70.9
Specific energy [Volume] [kWh/L]	0.78	1.31	2.36

As shown in table 1, raising the gas pressure from 35 to 70 MPa almost doubles the volumetric energy density while liquefaction at near ambient pressure approximately triples it relative to 35 MPa compressed gas. This is the reason liquid hydrogen is attractive energy storage option wherever space is constrained, or large amounts of hydrogen must be transported.

Hydrogen Molecule occurs in two isomeric forms, para-hydrogen and ortho-hydrogen with a different nuclear spin states of the protons in each atom. With decrease in temperature, the tendency of a hydrogen molecule being in a para state increase. At the ambient temperatures the normal hydrogen consists of 75% ortho and 25% para hydrogen while at temperatures <33K it can be assumed as pure para hydrogen. The intermolecular forces are slightly stronger for the ortho than those between para hydrogen molecules. The quantum mechanical rules tells us that the conversion of molecular angular momentum during the transition of ortho to para hydrogen is forbidden and requires external catalyst to facilitate the conversion. The conversion of normal hydrogen to para hydrogen is exothermic in nature releasing 525 kJ/kg of heat and this is larger than the enthalpy of vaporization at liquid hydrogen's normal boiling point of 448 kJ/kg. Excessive amounts of boil off can be generated if normal hydrogen is liquefied too rapidly leading to over-pressurization of the cryogenic tanks. [6]

1.3. Hydrogen as fuel

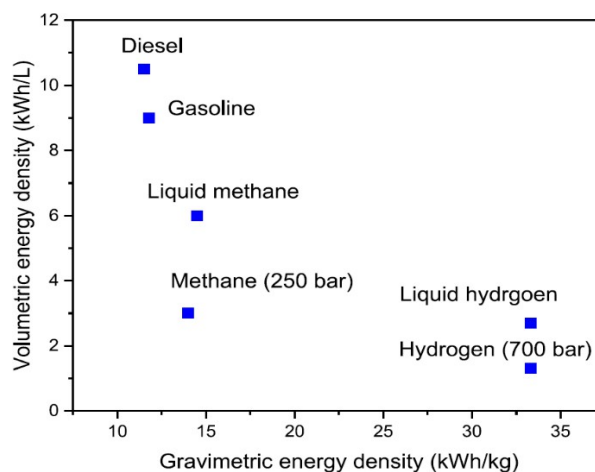


Figure 2. Energy density comparison of hydrogen with other common gases and liquids.[7]

As shown in figure 2, liquid hydrogen or 700 bar compressed gaseous hydrogen has the highest gravimetric energy density of any known substance, with a lower heating value (LHV) of approximately 120 kJ/g (33.3 kWh/kg). This is nearly three times the mass-based energy content of gasoline and more than six times that of compressed methane. The high gravimetric density is one of the strongest arguments for hydrogen fuel in sectors where weight is critical, such as heavy-duty trucking and long-range mobility.

However, hydrogen's volumetric energy density: the energy per liter of stored fuel is much lower than liquid hydrocarbons due to its low molecular density. Figure 2 illustrates this trade-off, while diesel and gasoline reach around 9-10 kWh/L, liquid hydrogen achieves only around 2.3 kWh/L, and 700-bar compressed hydrogen provides around 1.5 kWh/L. This highlights a fundamental engineering challenge showing hydrogen storage requires either high-pressure vessels (350-700 bar) or cryogenic liquefaction at -253°C, both of which add cost, energy consumption, and system complexity.

Hydrogen is the most abundant element of the universe and has been considered a promising energy source and an important chemical energy carrier capable of transforming the global energy landscape. Despite the challenges mentioned, there are compelling reasons why hydrogen remains a strong option for future decarbonized energy systems. Hydrogen provides zero tailpipe emissions, high gravimetric energy density, rapid refueling a

Natural resources are used globally and are depleting at an alarming rate due to increase in global economic activity and population. The consumption of fossil fuel is expected to rise by approximately 1.1 million barrels per day in 2025. [8]

1.4. Fuel Cell Electric Vehicles

Hydrogen is a primary energy carrier and may be used to power various sectors like transportation, energy and other industrial processes. Hydrogen fuel cell vehicles as an alternate to internal combustion vehicles offer a cleaner alternative as they produce no harmful pollutants and emit only water vapor. Within the hydrogen economy framework, hydrogen electric vehicles and a capillary network of hydrogen refueling stations are critical. [9]

The expansion of HRS is necessary for the adoption of hydrogen fuel cell vehicles both for personal transportation (light duty vehicles - LDV) and industrial transportation like forklifts, buses and heavy-duty trucks. Hydrogen vehicles provide an advantage of quick refueling in minutes compared to battery electric vehicles (BEV), which require higher recharging times. Hyundai report shows that Xcient truck can be refueled as quick as 8 minutes depending on the external tank temperature whereas the battery trucks like Tesla Semi can be charged up to 70% in 30 minutes using mega charger. [10] [11]

Hydrogen vehicle refueling takes place at 350 bar and 700 bar depending on the transportation application and region. The Hyundai Xcient truck uses 700 bar refueling for North America as shown in figure 3, whereas the same model uses 350 bar filling pressure in Europe. At 350 bar, the truck has 39.3 kg storage, while the 700 bar has 68.6 kg storage capacity. The 700 bar North America model of Hyundai Xcient provides an all-electric range of up to 450 miles with full load.

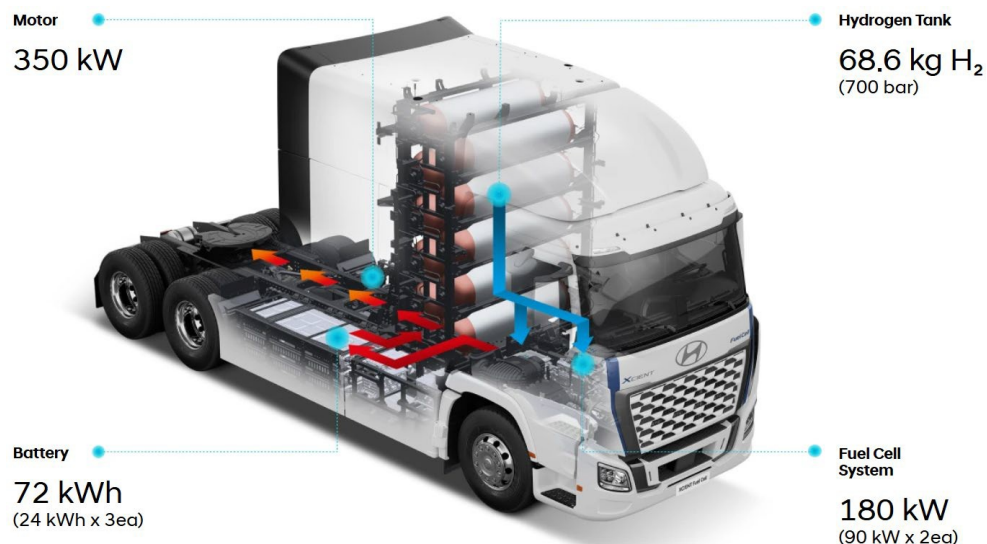


Figure 3. Hyundai Xcient North America Specifications

The Hyundai XCIENT Fuel Cell is a heavy-duty Class 8 (6×4) fuel-cell electric truck developed for long-haul freight applications. The truck uses two 90 kW hydrogen PEM fuel cell stacks that provide the main continuous power coupled to an electric motor rated at 350 kW driving the rear axles. Energy is stored on board in two forms, compressed hydrogen gas at 700 bar and lithium-

ion battery pack of 72kWh capacity. Battery is provided in FCEVs to size the fuel cell closer to average power required instead of the peak power requirement. During acceleration or hill climbs the battery supplies extra power so the motor can exceed the fuel cell ratings. This allows fuel cell to operate closer to an efficient operating point and avoid degradation. [12]

1.5. Hydrogen Refueling Protocols

The SAE J2601-2 protocol defines standardized fueling conditions to ensure safe, reliable, and time-efficient hydrogen dispensing for 700 bar heavy-duty vehicles as mentioned in table 2. The protocol prescribes strict limits on gas temperature, pressure, and mass flow rate to prevent over-pressurization and excessive thermal rise in the vehicle tank during fast filling shown in Figure 4. Together, these conditions form the basis for real world hydrogen refueling control algorithms and are essential for designing hydrogen refueling stations, thermal precooling and safety systems.

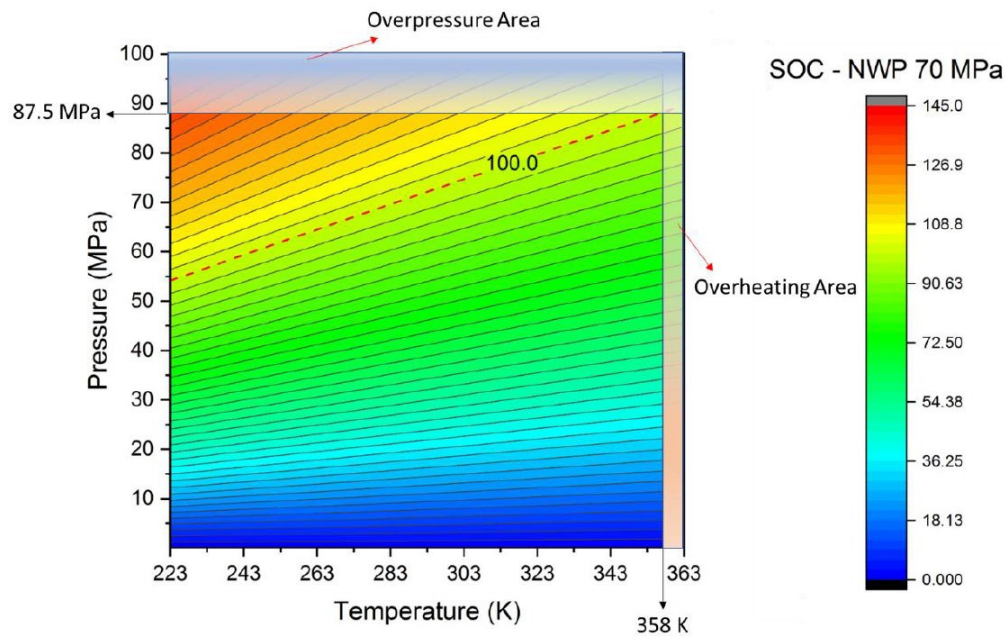


Figure 4. Allowable SOC as per pressure and temperature of vehicle tank during refueling.[13]

Table 2. 700 bar Hydrogen Refueling Protocol as per SAEJ2601-2.

Parameter	Limit
Minimum gas temperature	- 40°C
Maximum gas temperature	85°C
Minimum Dispenser Pressure	0.5 MPa
Maximum Dispenser Pressure (125% NWP)	87.5 MPa
Maximum Flow rate	0.06 kg/s

1.6. Hydrogen Refueling Infrastructure

The deployment of hydrogen refueling infrastructure is a critical enabler for fuel-cell electric vehicles (FCEVs), particularly in hard-to-electrify segments such as heavy-duty trucks and buses. Over the past decade, hydrogen refueling stations (HRS) have expanded from a handful of demonstration sites to an emerging global network.

The hydrogen produced from electrolysis is gaseous and it is stored in high pressure storage tanks to refuel vehicle tanks at 350 bar and 700 bar pressure. The boiling point of liquid hydrogen is -252.8 C at 1 bar and is required to be at cryogenic temperature. Hydrogen can be stored in tanks for several months as a reliable backup energy source. [14]

The HRS refueling involves gaseous hydrogen dispensing into the vehicle tank. Stations can have a gaseous or cryogenic on-site hydrogen storage. Gaseous stations with only compressor as dispensing system have certain limitations and contribute to high costs. Compressors require more maintenance and are energy intensive with limited capability of mass flow rate. This requires bigger high pressure cascade storage to meet the high vehicle refueling demand. This increases the station land area requirements around 10 m^2 per 130 kg of storage. [15] Multiple techno-economic studies and planning reports suggest that liquid hydrogen infrastructure becomes more attractive at higher station capacities (more than 1200 kg/day demand), while gaseous hydrogen delivery remains more suitable for low-demand sites. [16]

The IEA 2023 report shows that the fuel cell trucks demand is growing faster than light duty vehicles, increasing over 60% from the previous year. IEA 2025 mentions that hydrogen demand for transportation grew around 40% year-on-year and still being the minor part of the global hydrogen demand, around 0.1% of total consumption. Report shows that the stock of FC trucks in China have increased by 40% in 2024 compared to last year with 25% increase in global stock of FC buses. In Europe, the hydrogen consumption for transportation grew by over 50% due to rise in FC heavy duty trucks. [17] This shows a growing interest in hydrogen vehicles and to refuel these increasing vehicles we will need more refueling infrastructure globally.

All around the world, FCEV adoption is accelerating with the help of HRS pilot projects in Europe, North America, Japan, South Korea, China and India. Recent studies show that favorable government policies, industrial investment and consumer incentives are helping in growing the refueling network. [18] A report shows that there were around 1160 hydrogen refueling stations in operation worldwide at the end of 2024 representing increase compared to 2023. [19]

The major capital investment for HRS setup and installation is in equipment with hydrogen filling capacity and energy consumption being major part of operating costs. Therefore, reducing these is important to get desirable return on investment for the businesses.

Despite the high capital expenditure, operating costs and supply-chain challenges, significant opportunities exist for hydrogen refueling infrastructure, particularly in heavy-duty transport. Long-haul trucks have large daily energy demands and tight uptime constraints. Fast refueling and

high gravimetric energy density make hydrogen attractive in these segments compared with battery electric options that require very large battery packs and long charging times.

1.7. High Pressure Gaseous Hydrogen Tanks

Hydrogen needs to be stored at high pressure to minimize the storage size requirements. There are Type I to IV tanks categorized by International Standard Organization (ISO) and the American Society of Mechanical Engineers (ASME) based on different properties and pressure capacities. Type I and II typically have metallic cylinders and have lower pressure limits of less than 10 to 20 bar, making them less suitable for vehicle applications. Whereas Type III and IV tanks are made of metallic or polymer coated liners respectively with reinforced carbon fiber composites for better structural strength and lighter weight making this preferred choice for FCEVs. [20]

Type IV tanks have an operating pressure range of around 70 MPa and have higher strength-to-weight ratio with added advantage of corrosion resistance. These tanks have high-density polyethylene (HDPE) liners and have carbon fiber reinforced composites providing such advantages. These tanks are tested to perform safely as per the SAE J2601 standards for the temperature, pressure, and pressure ramp rate.

1.8. Electrolytic Hydrogen Production

The Hydrogen Economy concept is where hydrogen serves as the primary energy carrier and is produced using renewable energy sources. Hydrogen and Electricity are believed to be the most dominant energy carriers in the future when the global energy market becomes non-fossil based. [21]

“Green” hydrogen is a well-known clean and sustainable energy as it is generated using only renewables in contrast with traditional fossil-fuel based “grey” or “blue” hydrogen production technologies. Hydrogen production can happen using various methods: water electrolysis, steam methane reforming, methane pyrolysis, and biomass gasification amongst the most common ones. Water electrolysis using renewable electricity is considered the cleanest and most sustainable method of hydrogen production. [22]

Electrolysis technologies that currently dominate the green hydrogen are Alkaline, Proton Exchange Membrane (PEM), Anion Exchange Membrane (AEM) and Solid Oxide Electrolysis Cell (SOEC). Among these PEM electrolyzers are mostly suitable for the integrated operation with intermittent renewable sources due to operational flexibility. And with 40 times increase in solar PV capacity and 6-fold increase in wind energy from 2010 to 2023, PEM electrolyzers can play a crucial role in green hydrogen economy. [23]

For projects planned beyond 2025, PEM projects are estimated to reach an average of 297 MW installed capacity which is higher than the Alkaline projects. This shows strong confidence in cost reductions and operational performance and efficiency improvements for the PEM technology. [24] Green hydrogen is produced by electrolysis using solar or wind energy and does not release any greenhouse gases. Its potential and ability to decarbonize sectors that are heavily dependent on fossil fuels makes it very significant for the net-zero global economy. [25]

In our work hydrogen is produced via PEM electrolysis supplied by a combination of on-site solar PV and grid electricity. The carbon intensity of the produced hydrogen therefore depends on the time-varying grid mix. Only the PV supplied fraction can be classified as ‘green hydrogen’ as its being produced only using renewable energy source. While the grid-supplied fraction corresponds to grid-mix hydrogen with an associated CO₂ intensity (kg CO₂/kg H₂).

1.9. Optimization for Hydrogen Stations

The mathematical optimization for the hydrogen systems and stations have been developed by many researchers in the past reflecting the importance of the methods to improve and design an optimized system. The study by Yi Pang, et. al. [26] addresses this by proposing an off-grid integrated energy system combining wind and PV generation, batteries, electrolyzers, hydrogen storage, heat storage tanks, and absorption chillers and formulating MIQCP optimization to minimize total life cycle cost while jointly determining optimal equipment sizing and hourly scheduling. The results show the proposed configuration can satisfy hydrogen demand alongside building loads and can outperform reduced-component alternatives, with sensitivity analysis highlighting PV economics as a dominant life cycle cost driver and PV often emerging as the main contributor due to correlation between solar availability and hourly hydrogen demand.

A recent study [27] developed a mixed-integer linear programming (MILP) framework to optimally design a hydrogen refueling station integrated with an on-grid concentrated solar power system, with the objective of minimizing total life-cycle cost while satisfying operational and capacity constraints. The model simultaneously selects optimal HRS component sizes, solar field area, and grid import/export decisions, and is validated for Dhahran, Saudi Arabia to meet a taxi-fleet demand of about 4202 kg hydrogen per day. Results indicate the system requires a around 71,721 m² solar field producing roughly 50,233 MWh/year and electrolyzer capacity of 9352 kW with excess electricity of 10,515 MWh/year exported to the grid, improving the project economics; the reported LCOH is 7.17 \$/kg, demonstrating technical feasibility but also highlighting that high upfront investment still makes hydrogen less cost-competitive than fossil fuels today. The authors emphasize that grid export can materially support viability in high-irradiance regions and note future extensions such as incorporating stochastic demand/weather, adding other renewables (PV/wind), and improving electrolyzer safety considerations at low loads.

1.10. Challenges

A major challenge in developing an integrated, self-sustaining hydrogen refueling station (HRS) lies in the accurate sizing and coordination of all major subsystems: the electrolyzer, liquefier, cryogenic storage tank, gaseous buffer tanks, high-pressure pump, multi-stage compressors, vaporizers, and dispensing hardware. Unlike conventional fueling infrastructure, the hydrogen production and refueling demand profiles are highly variable, which makes inappropriate sizing a significant risk for both performance and cost. The capacity factor of on-site hydrogen infrastructure remains one of the most critical determinants of the levelized cost of hydrogen (LCOH). Low utilization of electrolyzers and compressors dramatically increases cost per kilogram.

Current research shows that the cost of hydrogen refueling stations (HRSSs) remains one of the main barriers to large-scale fuel-cell vehicle deployment. Detailed component-level studies highlight that electrolyzers, compressors, pumps and high-pressure storage dominate both capital and electricity costs. High station costs are further compounded by the cost and utilization of on-site PEM electrolyzers and the complexity of coordinating them with variable renewables and the grid. Shaner et al. mentioned the high LCOH of \$12.1/kg with PV-coupled electrolyzers system at low capacity factor of around 20% and electrolyzer CAPEX of 900 \$/kW [28]

Transportation alone accounts for 25% of total CO₂ emissions in 2018 from fuel consumption and is projected to grow at 1.7% rate from 1990 to 2022. [29] The decarbonization of heavy-duty vehicles is a major challenge due to limited technology and infrastructure.

The demand for liquid hydrogen is rising with new end-use applications, which are often located far from centralized hydrogen production plant sites. This creates a logistical and optimization problem connected to storing, transporting, loading, and unloading large quantities of liquid or high-pressure gaseous hydrogen, while minimizing boil-off losses, maximizing mass efficiency, and minimizing energy intensity.

A big factor influencing boil-off losses during transportation is sloshing, which happens due to the movement of liquid hydrogen in the vessel. The LNG industry has developed methods to reduce sloshing boil-off losses, such as baffles in the tank and minimum fill levels during transportation. However, such measures are generally not effective in liquid hydrogen due to higher boil-off rate as it required significantly lower temperatures to remain liquid.

Safe operation and handling is another major challenge in the hydrogen supply chain as it directly relates to both maintenance and cost. Hydrogen gas, due to its small molecular size of 0.28 nm and high diffusivity of around 0.410 cm²/s is highly prone to leaking. It is also very likely to ignite due to its wide flammability range (4 to 74 vol% in air) and very low ignition energy (0.017 mJ). Hydrogen flames are hot (~2400 K) but nearly invisible, making it difficult to detect. Also, liquid hydrogen and the boil-off generated due to very low temperatures can produce severe burns and

injuries if in contact with humans. Based on the above studies and facts the major challenges in hydrogen supply chain can be established in cryogenic losses, economics, scale and safety. [30]

1.11. Objectives

Recent operational issues across existing HRS networks, including hydrogen shortages, high operating costs, boil-off losses, and station downtime, have contributed to unmet customer demand and declining FCEV adoption. Centralized production and transportation of hydrogen introduce significant variability, while station-level storage constraints often prevent consistent availability. These challenges are particularly critical for the emerging heavy-duty hydrogen trucking sector, where battery-electric vehicles face practical limitations related to mass, range, charging time, and mineral dependency. Therefore, station architectures capable of producing and dispensing hydrogen locally, while maintaining high thermodynamic and mass efficiency is essential for enabling reliable 700-bar heavy-duty refueling.

The objective of this research is to develop a fully self-sustaining hydrogen refueling station (HRS) framework that integrates on-site renewable hydrogen production, liquefaction, cryogenic storage, and 700-bar dispensing into a unified, optimally controlled system. By co-locating all major processes: electrolysis, liquefaction, liquid hydrogen, storage, gas compression, and vehicle fueling, this work aims to overcome the supply-chain and replenishment challenges that currently limit the reliability and commercial viability of hydrogen refueling stations. The work aims to minimize boil-off losses, improve overall mass efficiency, and reduce electrical energy consumption through optimal scheduling. Also identify the optimal sizing of electrolyzers, liquefiers, pumps, compressors, and storage tanks to reduce capital costs, while increasing electrolyzer capacity factor and ensuring the required daily hydrogen throughput for heavy-duty vehicles for 2 TPD stations. Overall, the thesis establishes a design and control framework for next-generation, on-site hydrogen refueling systems that can deliver reliable, low-cost, and thermodynamically efficient hydrogen for heavy-duty transportation.

Chapter 2. Systems Components and Modelling

In the following sections, we describe the main components and the modelling methodology in the HRS system. Figure 5 shows the process schematic for the HRS system divided into two subsystems and both the systems are modelled separately. The electrical power consumption from subsystem 1 is provided as input to the subsystem 2 for the optimization model.

Each step has a fixed duration of 5 minutes time resolution. All equations use this constant time step to convert mass flow rate (kg/s) and power terms (MW) into discrete time changes of variables. Hydrogen is modelled as a single-component fluid with no impurities or ortho–para conversion dynamics. Thermophysical properties (density, enthalpy, entropy) are obtained from REFPROP wherever needed. Explicit wall heat transfer and natural boil-off are not modelled dynamically and boil-off associated with pump operation is represented indirectly via the pump efficiency. The 350 and 900 bar gaseous hydrogen buffer tanks are assumed isothermal at a fixed temperature of 298 K. There is no mass held up in the piping or in any components; the only storage of hydrogen is in the cryogenic tank and gaseous buffer tanks.

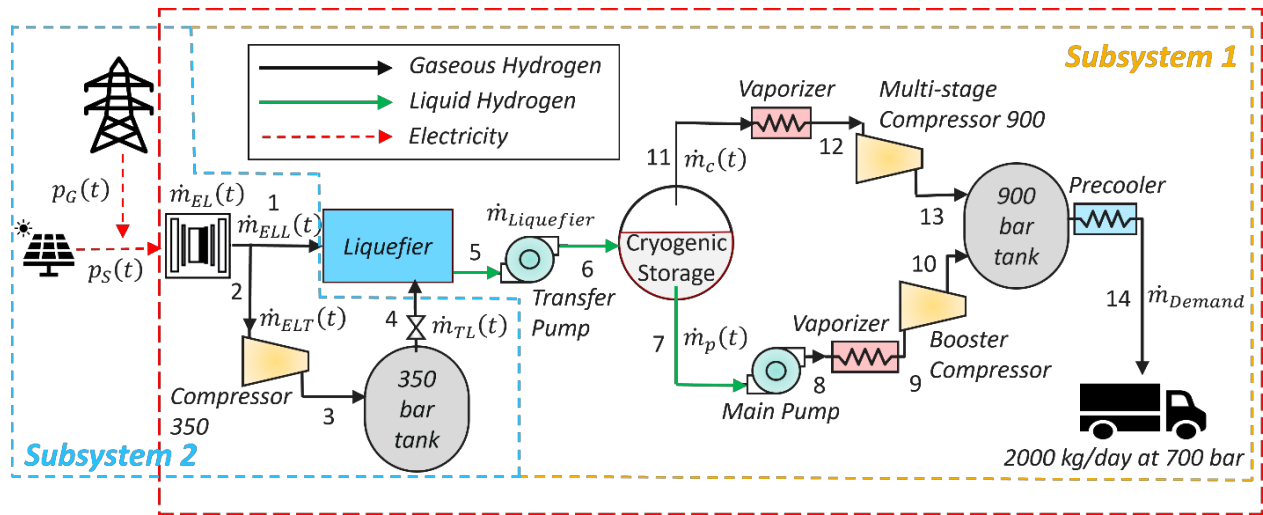


Figure 5. PV-Grid Integrated Liquid Hydrogen Refueling Station for 700 bar heavy-duty vehicle refueling.

2.1. Assumptions

Table 3. List of modelling assumptions for each HRS component.

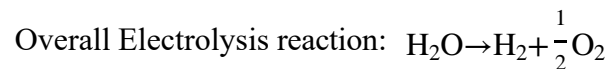
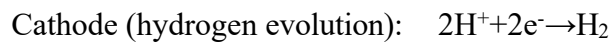
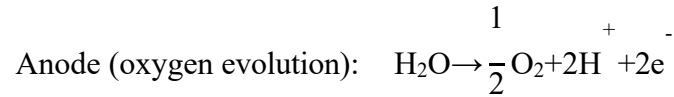
Category	Assumption
General Fluid Model	<ul style="list-style-type: none"> Hydrogen is modeled as a pure substance with no impurities or ortho-para conversion dynamics. Liquid hydrogen near saturation at ≈ 20 K. Thermophysical properties (density, enthalpy, entropy) obtained from REFPROP.

Cryogenic Tank Model	<ul style="list-style-type: none"> • 0-D lumped parameter model and no spatial temperature distribution. • Wall temperature assumed uniform and no thermal mass considered. • No pressure drops or heat loss in pipes; hydrogen in pipes neglected. • No explicit venting or PBU during normal operation (except pump-only case). • Tank pressure modeled as affine function of liquid and vapor mass. • Operating pressure band: 80-100 psi (≈ 5.5-6.9 bar).
Main Cryogenic Pump	<ul style="list-style-type: none"> • Modeled as incompressible hydraulic machine; mechanical efficiency = 65%. • Boil-off losses from pump (95% mass efficiency). • Neglects kinetic and potential energy changes; work from isentropic enthalpy rise and efficiency via REFPROP. • Pump discharge is fully vaporized to 298 K at 550 bar in the pump-line vaporizer before entering the booster.
Compressor	<ul style="list-style-type: none"> • Five-stage intercooled design; per-stage isentropic efficiency 75%. • Equal pressure ratio per stage; intercooler pressure drop = 30 kPa; outlet cooled to 303 K after each state. • Neglects kinetic and potential energy changes; work based on enthalpy rise. • This model is used only for diagnostics to get SEC for MILP. • Electrolyzer compressor is modelled as 3-stage with similar assumptions; Electrolyzer output assumed at 35 bar and 333K. •
Vaporizers	<ul style="list-style-type: none"> • Constant pressure heating devices: pressure drop neglected. • Heats liquid hydrogen from cryogenic temperature to ambient 298 K at 550 bar for pump line. • Heat gaseous hydrogen from cryogenic temperature (~ 25 K) up to 303K at tank pressure for main compressor suction.
Liquefier	<ul style="list-style-type: none"> • Treated as black box with fixed SEC = 11.9 kWh/kg. • Constant inlet and outlet hydrogen mass flow with no delay.
Gaseous Buffer Tanks	<ul style="list-style-type: none"> • Both the 350-bar ELX buffer and 900-bar HRS buffer are modeled as 0-D, single-phase, isothermal tanks at 298 K. • Tank pressure is obtained from REFPROP given mass and fixed volume at $T = 298$ K with no temperature evolution. • No explicit modeling of heat transfer with ambient; any compression heating is assumed to be rejected before the gas is stored.
Energy Modeling	<ul style="list-style-type: none"> • All component energy demands are expressed as linear functions of mass flow and SEC.

2.2 PEM Electrolyzer

Our study uses the PEM system model from Mathworks [31] as shown in Figure 6. The model combines electrochemical, thermal-fluid and gas phase transport physics. The PEM electrolyzer converts electrical energy into chemical energy and oxidizes water into hydrogen and oxygen.

The reactions in the PEM electrolyzer are:



The Simulink model is an integrated water electrolyzer stack with balance of plant: water supply, thermal management, gas separation and drying, and hydrogen back-pressure control.

The MEA block connects to the anode, cathode and thermal network. Anode moist air block models oxygen and water vapor removal, Cathode models hydrogen and Thermal block models the liquid water feed, recirculation and heat removal. The MEA block computes the cell voltage from reversible Nernst potential, activation overpotentials, ohmic losses through membrane and GDLs, and concentration losses at high current density.

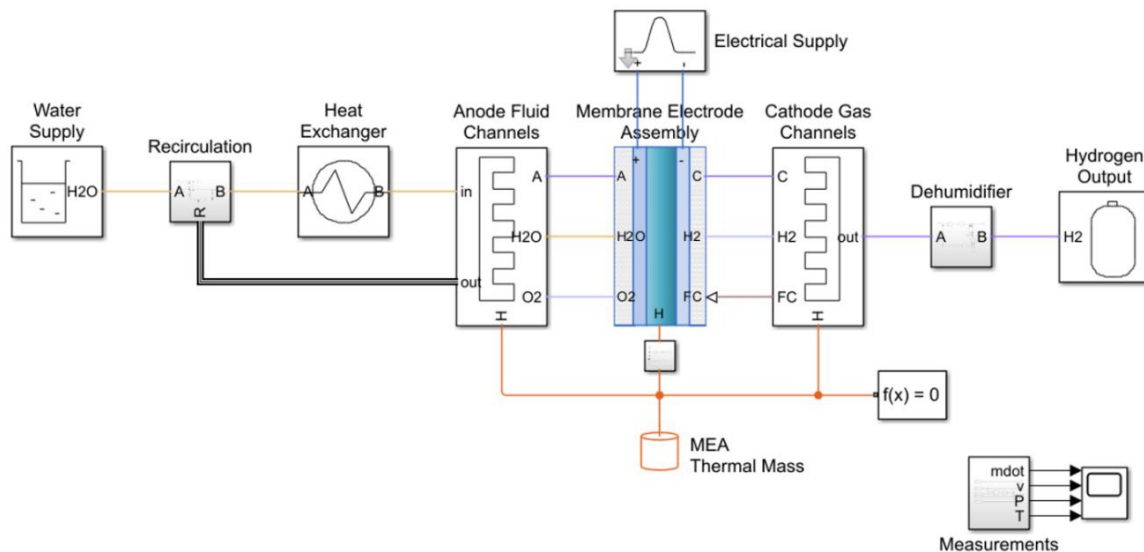


Figure 6. PEM Electrolyzer Balance of Plant Simulink Model. [31]

The water supply subsystem provides DI water to the anode recirculation loop. This block contains a water reservoir for the properties, supply pump to feed water into the recirculation loop, and a

PI controller to adjust the pump flow rate to ensure the system water level is sufficient to supply for consumption and evaporation.

The recirculation loop on anode side ensures that water is recirculated to supply water and remove heat. A circulation pump and PI controller work to maintain the stack temperature at a setpoint temperature of 80°C. If the stack becomes hotter than 80°C, the controller increases the water flow to increase the heat removal and if it cools below setpoint, the water flow is reduced. The separator tank subsystem is used to model the phase separation of oxygen and water in the anode returning stream. Liquid water exits from the bottom port back into the recirculation loop and the oxygen exits from the top to the environment.

In the Anode fluid channels block connects the thermal liquid network to anode moist air network. The water channel inflow/outflow models the anode liquid inlet/outlet to MEA water port and local heat transfer between water and MEA. The cathode gas channel subsystem maintains moist air along the cathode side and hydrogen channel outflow receives hydrogen and water vapor from MEA cathode port and mixes it with dehumidifier. Mass and energy transport between gas channels and MEA are modelled with heat transfer management for the stack.

The dehumidifier subsystem has volume block where the water vapor condenses, and the moisture sink removes condensed water from hydrogen system. The heat exchanger subsystem uses geometric inputs like exchanger length, width, height, tube height and spacing, fin spacing and efficiency etc. These parameters are combined to calculate effective heat transfer coefficient and pressure drops. The electrochemical heat generated in the stack is removed and transported by the water and dissipated to the surroundings.

2.3. Hydrogen Liquefaction

Liquid hydrogen provides advantage of purity, ease of gasification and end use versatility. It also provides high volumetric hydrogen density, i.e., 70.9 kg/m³ which is approximately 80% more than compressed gaseous hydrogen at 70 MPa, i.e., 39.2 kg/m³. However, challenges associated with liquid hydrogen storage include its energy intensity, giving Specific Energy consumption (SEC) of 11.9 to 15 kWh/kg of liquid hydrogen. The SEC of liquefier is defined as the electrical energy required to liquefy a unit mass of hydrogen. Another challenge is the cryogenic boil-off loss associated with transportation, storage and replenishment. NASA's data shows that during its Space shuttle program between 1977 and 2011 only 54.6% was used and the remaining was lost.

There are three major hydrogen liquefaction cycles

1. Brayton refrigeration
2. Linde-Hampson
3. Claude

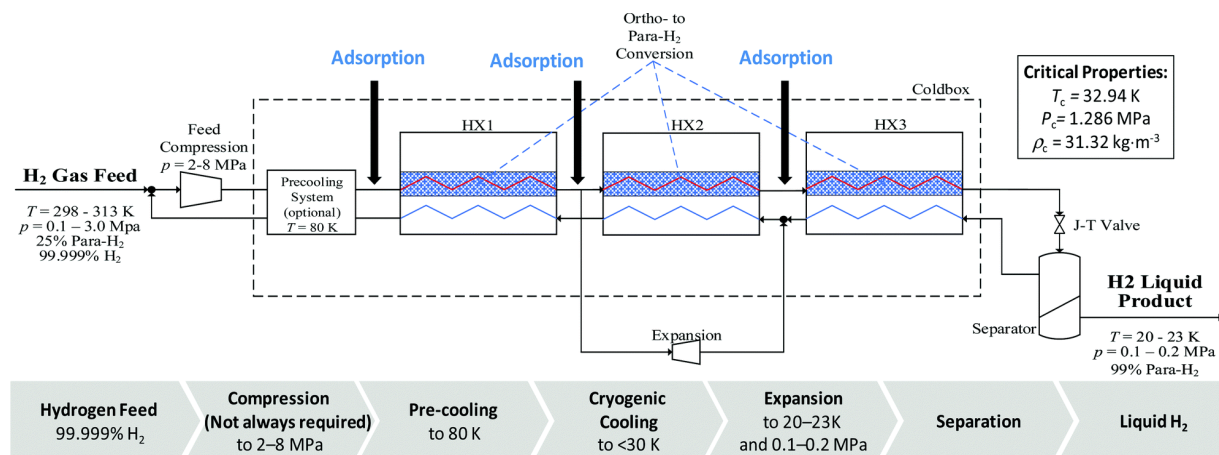


Figure 7. Simplified diagram of simple Claude based hydrogen liquefaction process with critical para-hydrogen properties. [30]

The Claude cycle is generally considered an efficient choice for systems with more than 2 TPD of production capacity. For a simple Claude cycle as shown in Figure 7, the hydrogen liquefaction process starts with pre-compression if the feed is provided at the low pressure. The next stage is optional precooling ($\sim 80\text{K}$) and adsorption to remove impurities that might result in freezing while liquefaction. The hydrogen is then cooled to cryogenic temperatures ($<30\text{K}$) in a closed-loop refrigeration cycle. This stage involves the catalytic conversion of ortho to para hydrogen in a supported iron oxide-based catalyst bed. The last step is usually adiabatic expansion using a joule Thompson valve. Then the final liquid hydrogen with para-hydrogen fraction of more than 98% is transported and stored. This study reported that the Linde-Leuna unit established with LN₂ pre-cooled Claude cycle with 5TPD capacity have a SEC of 11.9 kWh/kg of liquid hydrogen.

The liquefier unit is assumed to be a black box for the SEC calculations and is not modelled in this optimization code. Start-up, shut-down and transient behavior are neglected. The liquefier unit is treated as a continuous base-load unit whose output must be consistent with the downstream refueling demand, while keeping the cryogenic tank within its pressure and inventory constraints. The SEC is assumed to be 11.9 kWh/kg of liquid hydrogen and is used to capture the total electrical energy required for the complete liquefaction cycle. [30]

2.4. 2-phase Cryogenic Storage

The dynamic model of 2-phase cryogenic storage tank is originally based on the work by Osipov et al [24], which is used for rocket propellant loading simulation and was published open-source (NASA Technical report 216394). [25] This code models dynamic process for conduction vs convection in the saturated film region and the liquid/vapor hydrogen, energy balance, condensation and evaporation. The model is a reduced-lumped parameter model for multiphase mass and energy balance and have originally used ideal gas equations.

Liquid hydrogen storage and transfer tanks operate under strongly time-dependent conditions. During filling and transfer, the tank experiences (i) continuous changes in liquid and vapor inventory due to inflow and outflow, (ii) a growing or shrinking ullage volume (iii) pressure variations driven by vapor density and thermodynamic state, and (iv) environmental heat leak through tank wall. These coupled effects occur on time scales of seconds to hours and cannot be captured with a steady-state thermodynamic calculation. A dynamic model is therefore required to capture transient pressure changes, phase change, boil-off and condensation behavior.

The uncertainty in cryogenic tank transients is often the rate of heat exchange between the bulk phases (liquid and vapor) and the interface. Near the liquid-vapor boundary, heat can reach the interface by two competing mechanisms: conduction and natural convection. Conduction happens through a thin thermal boundary layer when the adjacent fluid is relatively stagnant. In this case, heat transfer scales with the thermal gradient across an effective penetration depth, and the interface exchange behaves like an equivalent heat transfer coefficient. Natural convection happens when the temperature stratification becomes unstable. If warmer, lighter fluid lies below cooler, denser fluid (or vice versa depending on the phase) then buoyancy induces motion that increases heat transfer beyond conduction.

To couple the two bulk phases without resolving full multidimensional interfacial structure, the model uses concept of saturated interfacial film. This film is a thin region adjacent to the liquid-vapor boundary that is assumed to remain at thermodynamic equilibrium or saturated corresponding to the prevailing tank vapor pressure. The film is characterized by a single temperature, which is computed from a saturation relation as a function of vapor pressure and is allowed to evolve dynamically using a first-order Osipov-type relaxation toward the instantaneous saturation value. Heat exchange from the bulk liquid to the film and from the bulk vapor to the film is calculated using conduction and natural convection correlations. The resulting net interfacial heat rate determines the phase-change mass flux through the latent heat of vaporization.

Petitpas [34] made some key modifications in the code to make it more accurate and are made available open source. The chief modification was the use of real gas equation (REFPROP) of state replacing the ideal-gas equation. This is important to capture the accurate thermodynamic states in a two-phase region as ideal gas law makes linear assumptions for pressure and temperature. The code was written in MATLAB and used REFPROP thermodynamic database by NIST. Energy conservation equations were added to compute temperature variations in the liquid phase.

Additional assumptions implemented in the modified model are:

- Zero-dimensional and isothermal boundary layers in the saturation film interface at temperature T_s .
- Zero storage term of volume or mass of hydrogen in pipes.
- No pressure drops and heat loss across pipes.
- Isothermal Dewar tank wall.

- Assuming that the tank is being used continuously and the bulk liquid hydrogen temperature is very low and constant.
- Thermal inertia of the tank wall is infinite.
- No ortho-para conversion is considered assuming all hydrogen is in para state due to low temperatures and pressures and relatively short times.

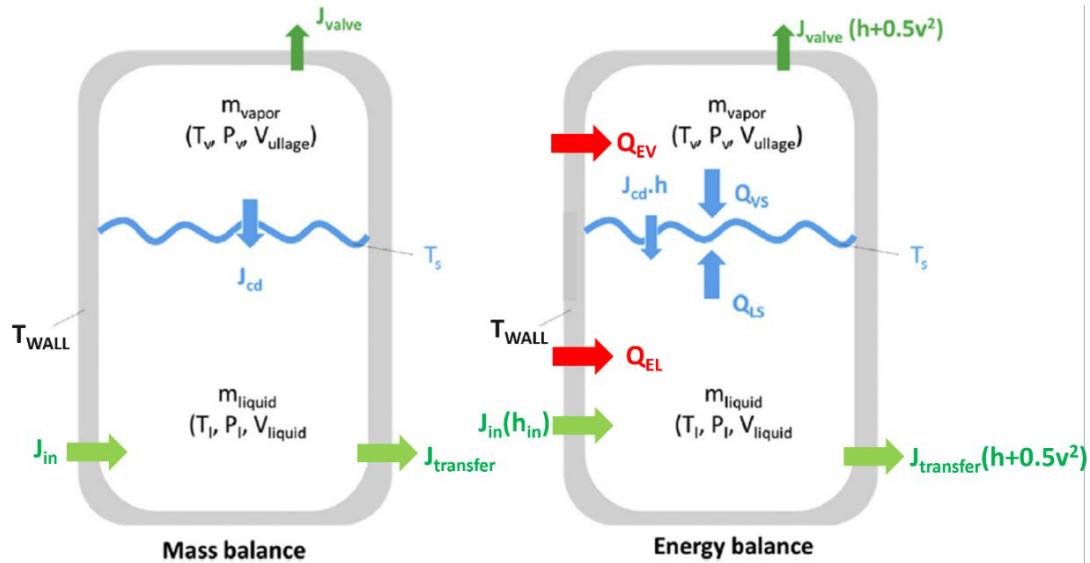


Figure 8. Simple illustration showing the mass and energy conservation for a 2-phase cryogenic hydrogen. Modified from [34]

The main governing equations of the model are reported below and thermodynamic variables illustrated in Figure 8. The subscripts (*v*) and (*l*) denote vapor and liquid properties respectively. The thin film interface is a boundary layer that exists between the bulk saturated liquid hydrogen and the superheated vapor hydrogen. It's where the boil-off occurs, i.e., liquid hydrogen vaporizes due to external heat ingress and heat and mass transfer happen across the phase boundary.

In order to have continuous and concurrent refilling and transfer of liquid hydrogen into the tank, a mass flow rate J_{in} of liquid mass enters cryogenic tank from the liquefaction unit with a known constant temperature (20K) and pressure (110 psi), and a flux $J_{transfer}$ represents the liquid mass discharged at constant flow rate, equal to the pump discharge flow rate. The mass flow rate J_{valve} represents the vapor mass entering/leaving the storage tank either due to the voluntary production of gaseous hydrogen via the vaporizer unit, or via management of the boil-off volume via a vent valve.

The flow J_{cd} represents the condensation with Q_{vs} and Q_{ls} being the heat transfer from the vapor and liquid phase, respectively. The red arrows represent the heat transfer from the environment to the vapor (Q_{EV}) and to the liquid (Q_{EL}) masses, respectively.

$$\frac{d\dot{m}_{EE}}{dt} = -\dot{J}_{tr} + \dot{J}_{cd} + \dot{J}_{in}$$

$$\frac{d\dot{D}_{VV}}{dt} = -\dot{J}_{aa, valve} - \dot{J}_{cd}$$

$$\dot{J}_{cd} = -\frac{\dot{Q}_{EES} + \dot{Q}_{WS}}{q_{qh}} \quad (q_{qh} > 0)$$

$$\frac{d(\dot{m}_{EEU})}{dt} = \dot{Q}_{EEE} - \dot{Q}_{EES} + p_p d\dot{V} - \dot{J}_{tr} h_{EE} + \frac{u_{EE}^2}{2} + \dot{J}_{cd} h_{cd} + \dot{J}_{in} h_{in}$$

$$\frac{d(\dot{m}_{VVU})}{dt} = \dot{Q}_{EEV} - \dot{Q}_{WSS} - p_p d\dot{V} - \dot{J}_{valve} h_{valve} + \frac{u_{valve}^2}{2} - \dot{J}_{cd} h_{cd}$$

2.5. Cryogenic Hydrogen Pumps

Liquid hydrogen stations use cryogenic pumps to pressurize the hydrogen before vaporizing and dispensing to the vehicle tanks. Cryogenic reciprocating liquid hydrogen pumps provide advantages of reduced energy consumption, large pumping mass flow rate, low capital investment and maintenance cost.

Guoyi Qiu et.al. studied reciprocating liquid hydrogen pumps under dynamic pressure, flowrate and temperature conditions for an HRS. They have used a pump with nominal mass flowrate of 50 kg/h with intake and maximum delivery pressure being 0.4 MPa and 87.6 MPa, respectively. The pump's isentropic efficiency and volumetric efficiency are reported to be 97.3% and 90.76%, respectively. One of the findings in Figure 9(a) shows that as the delivery pressure decreases from 15 MPa to 0.8MPa the isentropic efficiency drops rapidly from 98% to 2%, resulting in decrease in energy consumption for compression. It also shows that with a decrease of delivery pressure, the heat transfer in-cylinder decreases due to reduced temperature difference, and this results in lower pump boil-off losses. [35]

Guoyi Qiu et al compared some major reciprocating liquid hydrogen pumps available in the market as shown in Figure 9(b) [36]. The exponential relation shows the increase of specific work consumption with increase in delivery pressure. The ideal work consumption deviates significantly from actual work consumption as per the curve, especially for high delivery pressures. Based on the plot, Nikkiso ACD pump provides the capability of delivering very high flowrate with less energy consumption compared to other mid-range delivery pressure pump models. For the ultra-high delivery pressures above 50 MPa the liquid hydrogen pump efficiency decreases due to challenges posed by the cryogenic properties and pump design and seal. In addition to low efficiencies, the 90 MPa pump also asks for significant investment and maintenance cost compared to the 45 MPa pump.

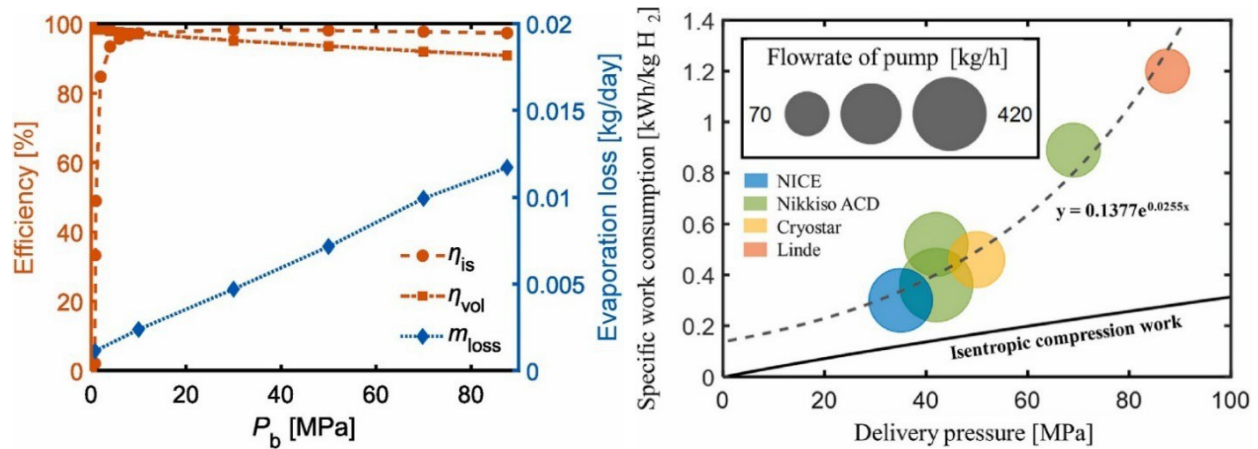


Figure 9. (a) Isentropic efficiency and evaporation loss [35] (b) Specific work consumption for different cryogenic pumps and mass flowrates under different delivery pressures.[36]

Cryostar is a leading hydrogen pump manufacturer and offers various models for various industries. Based on their industrial experience they found out that compression is the major operating cost for the hydrogen station and can account for up to 25% of the cost of dispensing. They also noticed that 90 MPa LH2 pumps are not reliable and cost-effective, and compressors are usually oversized due to inlet pressure limitations and are underutilized during off-peak hours.

Cryostar suggests that two stage compression is the best approach to reach 90 MPa. The first stage uses a mid-size pump of around 50 MPa with a heat exchanger to provide inlet pressure to booster compressor that pressurizes the hydrogen gas to ultra high-pressure range offering constant compression ratio of 2:1. Based on their industrial operation data it shows that this hybrid approach can reduce compression cost by 50-75%. As the hydrogen sector continues to grow, onsite liquid hydrogen storage will ease logistical challenges. Cryostar's MRP 40/55-K LH2 Pump offers max discharge pressure of 500 bar and max flow rate of 190 kg/h = 0.0527 kg/s with a low specific energy consumption of 0.4 kWh/kg H₂. The LH2 pump efficiency for Cryostar is 35.8% as mentioned by *Guoyi Qiu et al.*

Another major manufacturer of cryogenic pumps is NIKKISO as mentioned in plot figure 9(b) mentioned above. NIKKISO's MP-100 with a max discharge pressure of 550 bar with LH2 mass flow rate range of 40 to 1000 kg/hour with SEC of around 0.5 kWh/kg H₂. [37]

For a positive-displacement pump, mass flow is assumed to be set by speed and volumetric filling, and suction pressure only matters as it protects filling (NPSH). NPSHR is the minimum amount of pressure energy the pump needs at its inlet to prevent the liquid from vaporizing and forming bubbles (cavitation). When selecting or designing a pump system, you must ensure that the Net Positive Suction Head Available (NPSHA) in your system is always greater than the Net Positive Suction Head Required (NPSHR) by the pump to ensure proper and long-lasting operation. Considering adequate NPSH and proper discharge side pressure control, the mass flow rate of pump is controlled via VFD while holding constant discharge pressure.

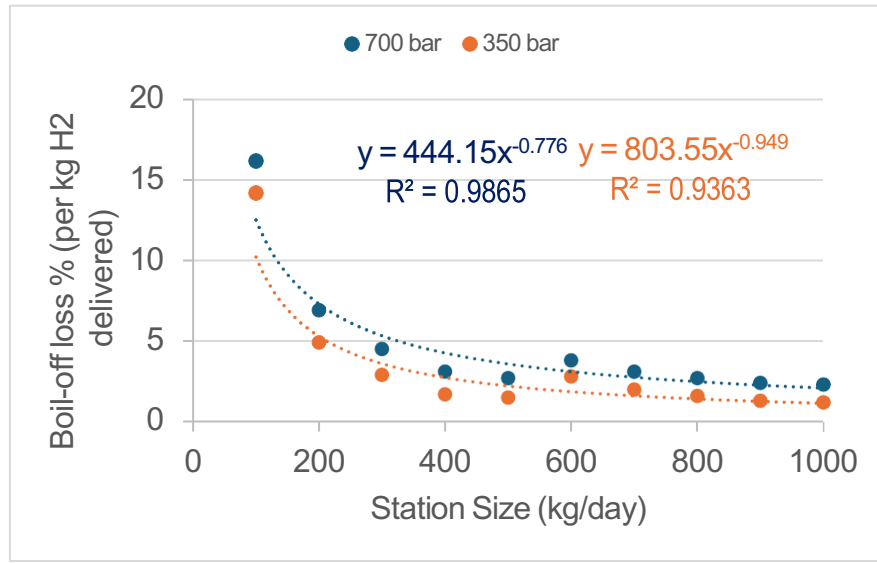


Figure 10. Cryogenic pump boil-off and station size curve fitting for 350 and 700 bar dispensing. Produced using experimental data from [38]

Figure 10 is based on experimental data by G. Petitpas [38] showing the relation between the specific boil-off loss per unit of hydrogen dispensed as a function of the liquid station size, which is the total amount of liquid hydrogen dispensed for a LH2 pump with a nominal flow rate of 100 kg/hr. It is observed that boil off losses are higher for stations that dispense less than 400 kg/day, due to low utilization of the pump. As utilization increases, the boil-off losses are reduced drastically, and it accounts for less than 2% for station dispensing around 2000 kg/day. Most boil-off generation in cryogenic liquid hydrogen pumps occurs during pump idling and pump pre-cooling or warming up as shown in figure 11, based on Petitpas experimental data. This shows that the best strategy to avoid boil-off losses from the cryogenic pump is to avoid transient operation with on/off events. The ideal way is to minimize pump idling and pre-cooling and keep pump operating with variable mass flow rate rather than switching on/off frequently.

In this HRS system model, the cryogenic pump withdraws liquid hydrogen from the 2-phase cryogenic storage tank and raises the pressure from the Dewar tank pressure to the downstream setpoint pressure of 550 bar. The optimizer calculates the required mass flow rate through the pump at each time step $mm_{pp}(dd)$ kg/s. The pump is modelled as an incompressible hydraulic machine with a mechanical efficiency $\eta_{\text{pump, mech}}$ of 65%.

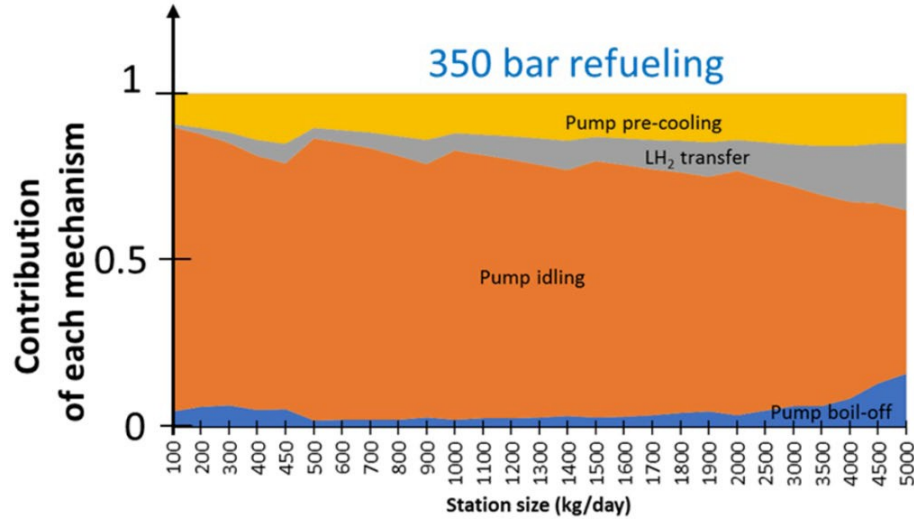


Figure 11. Boil-off contribution from cryogenic pump mechanisms for 350 bar refueling. [38]

At each time step, the suction pressure is obtained from the LH₂ tank liquid/vapor flash equilibrium and the discharge pressure is fixed at 550 bar. The real fluid thermodynamic properties (i.e., enthalpy, entropy, density) are obtained using REFPROP for hydrogen. Changes in kinetic and potential energy across the pump are neglected for the ideal mechanical work calculation. After calculating the inlet enthalpy and entropy of liquid hydrogen, we get the isentropic (ideal) enthalpy for discharge pressure and isentropic enthalpy rise is calculated. The actual specific work for pump is then calculated using the isentropic enthalpy rise and pump efficiency. The details and equations are discussed in the energy modelling section 2.7.

2.6. Compressors

Compressors are the biggest contributor to the levelized costs in an HRS, as shown in figure 12 (a) for gaseous hydrogen stations. Figure 12(b) shows the impact of station size and dispensing method (pumping and compression) on the HRS levelized cost. As shown, compressors and pumps are the biggest contributors to levelized cost. For low station size, it is more cost effective to have gaseous based system with compressor compared to LH₂ based pumping stations. The liquid HRS with pump is a better solution for high throughput station sizes of more than 1200 kg/day.[16]

A two-stage diaphragm compressor can be configured so that the two stages operate independently, allowing each compressor stage to operate over a wide range of mass flow and suction pressure. Diaphragm Compressor isentropic efficiency is reported as 80% and SEC range of 2-4 kWh/kg [39]. Specific electrical energy consumption per kg of hydrogen is reported at 4 kWh/kg within a delivery pressure range from 5 to 900 bar, with potential to reach 3 kWh/kg in 2030. [40]

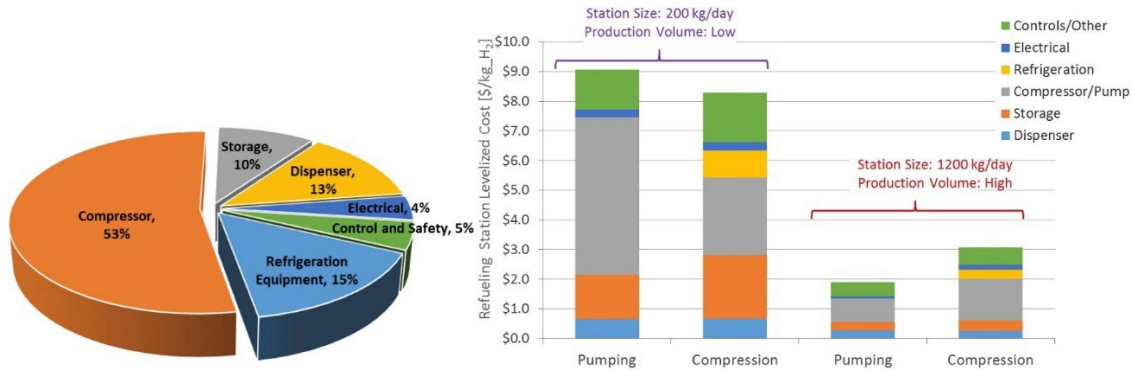


Figure 12. (a) HRS component cost contribution. (b) LCOH comparison for pump and compressor based stations for low and high station demand. [16]

Bauer et al. used five-stage compressor with a constant throughput using an intermediate cooling. The stage wise compression ratio is dependent on the overall minimum input and maximum output pressure. [41] In this optimization model the compressor is modelled as multi-stage intercooled compressor with real gas properties using REFPROP database. At each time step, the suction pressure is taken from the cryogenic tank pressure, and the discharge pressure is taken from the 900-bar buffer tank calculated from REFPROP using mass and volume.

For the compressor line vaporizer, which is placed upstream of the compressor, the inlet temperature from the cryogenic tank is assumed to be 25 K and suction pressure same as the tank pressure. The vaporizer heats up the hydrogen to 303 K before supplying it to the compressor. The pressure drop is neglected across the vaporizer. The enthalpy difference over this constant-pressure heating is used to compute the vaporizer energy consumption.

The 5-stage intercooled compression is assumed to operate with equal stage pressure ratio of 2.6, constant isentropic efficiency (75%), fixed intercooling temperature and pressure drop across each intercooler. The intercoolers are assumed to be cooled by a coolant fluid at 298K and after each intercooler the hydrogen gas is assumed to be cooled 5 K above the coolant, i.e., 303K. The intercooler pressure drop is considered constant of 30 kPa for each stage. The kinetic and potential energy changes are neglected, and the real compressor work is considered equal to the enthalpy rise.

For the compression stage 1 we have pressure and temperature, and the corresponding enthalpy and entropy are obtained using REFPROP. For stages $k > 1$ the hydrogen gas is assumed to be back at a cooler temperature using intercooler with slight pressure loss. Then enthalpy and entropy are again obtained using REFPROP using temperature and pressure from the previous stage.

For each stage, using same entropy and higher pressure we calculate isentropic enthalpy and actual outlet enthalpy using isentropic efficiency. Using the enthalpy difference, we calculate the specific work done per stage compression for per unit mass of gas and the sum of all stages gives us the total specific compressor work as explained in the energy modelling section 2.7.

The booster compressor after main cryogenic pump is assumed to be single-stage isentropic compressor with fixed isentropic efficiency of 75%. The suction pressure is assumed to be constant and equal to the pump discharge pressure and suction temperature is the outlet temperature of the pump-line vaporizer 298K. The booster compressor discharge pressure equals the 900-bar buffer tank pressure.

2.7. Energy modelling

This section describes the power and energy consumption calculation for the HRS components. These are calculated using the thermodynamic relations and REFPROP derived enthalpies and then reduced to linear Specific Energy Consumption (SEC) forms to use inside the MILP.

For any component with hydrogen flow rate and specific work or heat, the instantaneous power is

$$\begin{aligned}
 pp(dd) &= \dot{m}(dd) ww \quad [\text{W}] \\
 EE_{\Delta t} &= PP(dd) \Delta t \quad [\text{J}] \\
 EE_{\Delta t, \text{kWh}} &= \frac{PP(dd) \Delta t}{3600 \times 1000} \\
 MM &= \frac{\dot{m}(dd) \Delta t}{\eta} \\
 \text{SEC} &= \frac{EE_{\Delta t, \text{kWh}}}{MM} \quad [\text{kWh/kg}] \\
 pp(dd) &= 3.6 \text{ SEC } \dot{m}(dd) \quad [\text{MW}]
 \end{aligned}$$

For a cryogenic pump and compressor, the ideal isentropic specific work is computed using the enthalpy rise between inlet and outlet at constant entropy.

$$\begin{aligned}
 h_1 &= h(TT_{\text{in}}, PP_{\text{in}}) \\
 ss_1 &= s(TT_{\text{in}}, PP_{\text{in}}) \\
 h_{2_{ss}} &= h(PP_{\text{out}}, ss_1) \\
 ww_{\text{is}} &= h_{2_{ss}} - h_1 \quad [\text{J/kg}] \\
 ww &= \frac{ww_{\text{is}}}{\eta}
 \end{aligned}$$

The main gaseous hydrogen (GH₂) compressor is one of the most energy-intensive units in the refueling station. It raises hydrogen from the low suction pressure of the vapor from the cryogenic tank headspace (typically 5.5-6.9 bar) to the storage buffer pressure (up to 900 bar). To model this process accurately, the compressor is represented as a multistage isentropic compressor with

intercooling, where each stage compresses hydrogen to an intermediate pressure and then rejects heat to an intercooler before the next stage.

$$\text{Overall compression ratio, } PR_{\text{tot}} = \frac{PP_{\text{dis}}}{PP_{\text{suc}}}$$

To account for the pressure losses across the intercoolers the effective discharge pressure is calculated by increasing that loss and assuming equal pressure ratio per stage, the per stage pressure ratio is calculated. This ensures that each stage performs similar work and is consistent with industrial compressor designs.

$$PP_{\text{dis,eff}} = PP_{\text{dis}} + \Delta PP_{\text{cool}} - 1 \Delta PP_{\text{cool}},$$

$$PR_{\text{stg}} = \left(\frac{PP_{\text{dis,eff}}}{PP_{\text{suc}}} \right)^{1/N_{\text{stg}}}$$

For each stage, the inlet thermodynamic state is defined by,

$$h_{\text{in}} = h(TT_{\text{in}}, PP_{\text{in}}),$$

$$s_{\text{in}} = s(TT_{\text{in}}, PP_{\text{in}})$$

The stage outlet pressure, $PP_{\text{out}} = PP_{\text{in}} PR_{\text{stg}}$

Isentropic outlet enthalpy, $h_{2,ss} = h(PP_{\text{out}}, s_{\text{in}})$

Isentropic specific work, $ww_{\text{is,kk}} = h_{2,ss} - h_{\text{in}}$

Actual outlet enthalpy applying stage isentropic efficiency, $h_{2,\text{act}} = h_{\text{in}} + \frac{ww_{\text{is,kk}}}{\eta_{\text{is,stg}}}$

Actual stage work, $ww_{\text{kk}} = h_{2,\text{act}} - h_{\text{in}}$

After each stage the hydrogen is cooled back to the intercooler temperature and pressure is reduced assuming pressure drop across intercooler, this resets the inlet state for the next stage. The work and energy consumption of the intercoolers are not considered in the model.

Total Compressor work, $ww_{\text{comp, total}} = \sum_{kk=1}^{N_{\text{stg}}} ww_{\text{kk}}$ and the same methodology is used for power and total energy calculation as described for the pump above.

Vaporizers add sensible heat to hydrogen raising it from cryogenic or intermediate conditions to near ambient temperature. For a vaporizer with known inlet temperature and pressure and outlet temperature assuming no pressure drop the thermodynamic calculations are done.

$$h_{\text{in}} = h(TT_{\text{in}}, PP),$$

$$h_{\text{out}} = h(TT_{\text{out}}, PP)$$

$$\Delta h_{\text{vap}} = h_{\text{out}} - h_{\text{in}}$$

$$PP_{\text{vap}}(dd) = \dot{m}(dd) \Delta h_{\text{vap}},$$

$$EE_{\text{vap,total}} = \frac{PP_{\text{vap}}(dd) \Delta dd}{3600 \times 1000}$$

//

$$\text{SEC}_{\text{vap}} = \frac{EE_{\text{vap,total}}}{MM_{\text{heated}}}$$

The liquefier unit is assumed to take constant mass flow inlet and dispensing at a fixed rate as calculated by the optimizer. The liquefier converts the gaseous hydrogen to liquid at cryogenic temperatures. Rather than modelling the full refrigeration thermodynamics cycle as explained in section 2.3, a single SEC (kWh/kg) value is used to calculate the power and total energy consumption of the liquefier.

Chapter 3. Optimization Model

This chapter presents the optimization framework developed for an integrated hydrogen refueling station that combines production, liquefaction, cryogenic storage, compression, and vehicle dispensing within a single site shown in process schematic figure 5. The objective is to capture the tightly coupled mass, energy, and pressure dynamics across gaseous and liquid hydrogen subsystems, while enabling optimal operational decisions under realistic constraints.

A physics-informed, control-oriented modeling approach is adopted to represent each major component including the electrolyzer interface, liquefier, cryogenic storage tank, pumps, compressors, and buffer tanks using simplified thermodynamic relationships. These component models are embedded within a mixed-integer optimization framework to determine optimal equipment dispatch, sizing, and operating strategies that minimize energy consumption, boil-off losses, and capital investment, while ensuring reliable hydrogen delivery.

3.1. MILP and Solver

The optimization problem in this work is formulated as Mixed-Integer Linear Programs (MILPs). In a MILP, some decision variables are continuous (e.g., flow rates, power consumption, capacities), while others are discrete, typically binary ON/OFF or integer counts (e.g., start/stop decisions, unit commitment). A generic MILP equation can be written as:

$$\begin{aligned} \min_{xx, yy} \quad & ccxx + dddd \\ & AAxx + BBdd \leq bb \\ & xx_{D DLL DD} \leq xx \leq xx_{D DD D mm} \\ & dd \in \{0,1\} \end{aligned}$$

Where xx denotes vector of continuous decision variables and dd denotes the vector of binary variables. cc and dd are the cost coefficient vectors, and AA , BB , bb encode the linear constraints. This formulation is sufficiently general to represent capacity planning, scheduling, unit commitment, network flow, and many other engineering decision problems, provided that all constraints and the objective function can be written as linear expressions in the decision variables.

MILPs require specialized solvers and in this work, all MILPs are solved using the Gurobi Optimizer, a state-of-the-art commercial solver for linear, integer, and quadratic programming. All model formulation, the decision variables, constraints, and objective functions are constructed programmatically in MATLAB. The YALMIP toolbox is used as a modeling layer between MATLAB and Gurobi. Continuous variables are declared using `sdpvar` to define a matrix or scalar,

binary variables using `binvar` which can be 0 or 1, and constraints are assembled as sets of linear equalities and inequalities. YALMIP then automatically converts this high-level description into the standard MILP form required by Gurobi and calls the solver via the `optimize` command.

After the solver returns, MATLAB is used to extract the optimal decision variables and to perform further analysis: reconstructing time series, computing derived performance indicators, and generating plots for visualization. This combination of MILP modeling in MATLAB/YALMIP and solution by Gurobi provides a flexible and efficient computational environment for tackling large-scale mixed-integer optimization problems that arise in engineering systems design and operation.

3.2. Methodology

The optimization model is formulated in discrete time, where all mass flows, power, tank states and binary on/off decisions are defined at the fixed time interval. This approach allows mixed-integer linear programming (MILP) to solve constraints, storage dynamics and scheduling together.

In subsystem 1, the design variables (equipment sizes) and the operational variables (dispatch, inventories, boil-off, on/off schedules, power) are optimized simultaneously in a single mixed-integer linear programming (MILP) problem, rather than by running a size first, then dispatch loop. Tank capacities and nameplate ratings appear as decision variables that finds the feasible operation: storage inventory is constrained to remain within a range determined by tank size; pump and compressor flow or power are bounded by their selected capacities; and the allowed pressure window and mass balance equations must hold at each time step. Because these couplings are expressed inside the optimization model, the solver can choose sizes and dispatch together so that the total cost (CAPEX plus operating penalties and energy cost) is minimized while all physics-inspired constraints are respected. This formulation eliminates the need for many iterations because the feedback from sizing to dispatch is handled internally by the solver. It is a co-optimization problem where sizing and dispatch are not sequential decisions; they are jointly determined so that the final design is exactly the smallest set of capacities that still allows an economically optimal 24-hour operating schedule.

This work formulates the subsystem 2, solar-grid-electrolyzer-buffer system as a mixed-integer linear optimization problem solved over a 24-hour horizon with 5-minute time steps. A one-megawatt electrolyzer reference hydrogen-production profile is first loaded from the interpolated electrolyzer mass flow rate with solar power variation data and used to define a linear conversion between electrolyzer electrical input and hydrogen production at each time step. The available solar power is then calculated from the PV nameplate rating of 3 MW multiplied by a time-varying capacity-factor profile that represents the daily solar shape and includes derating and random cloud or fog disturbances. At every time step the model enforces three key requirements: the electrical power balance (PV plus grid must supply the electrolyzer, compressor, and fixed station load), the

hydrogen balance (the liquefier inlet demand must be met by a combination of electrolyzer output and tank discharge), and the tank inventory limits (tank mass must remain within bounds consistent with the allowable pressure range). The solution is obtained in stages: stage 1 minimizes the electrolyzer nameplate capacity to find the smallest electrolyzer that can satisfy all constraints across the day; stage 2 then fixes this minimum electrolyzer size and minimizes total cost while allowing the buffer tank size and operating schedule to adjust.

3.3. Decision Variables

3.3.1 Binary Decision Variables

Table 4. List of binary decision variables for MILP optimization.

Description	XXXXXXXXXXXXXXXXX $\in \{00, 11\}$
Main Cryogenic pump On/Off	$xx_{pp}(dd)$
Main Compressor On/Off	$xx_{cc}(dd)$
Main Pump start-up flags	$oonn_{pp}(dd)$
Main Pump shut-down flags	$oooo_{pp}(dd)$
Main Compressor start-up flags	$oonn_{pp}(dd)$
Main Compressor shut-down flags	$oooo_{pp}(dd)$
Electrolyzer to 350 bar buffer tank flow on/off	$zz_{cc}(dd)$

3.3.2. Continuous Decision Variables

The time-dependent continuous decision variables in table 5, $dd = 1, \dots, TT$

Table 5. List of continuous decision variables for MILP optimization.

Description	XXXXXXXXXXXXXXXXX
Pump mass flows [kg/s]	$m\dot{m}_{pp}(dd)$
Compressor mass flow [kg/s]	$m\dot{m}_{cc}(dd)$
350 bar gaseous hydrogen buffer tank mass [kg]	$MM_{350}(dd)$
900 bar gaseous hydrogen buffer tank mass [kg]	$MM_{900}(dd)$
2-phase cryogenic storage liquid mass [kg]	$MM_{liq}(dd)$
2-phase cryogenic storage vapor mass [kg]	$MM_{vap}(dd)$
2-phase cryogenic storage tank pressure [psi]	$PP_{tank}(dd)$
Electrolyzer power input [MW]	$ee(dd)$
Solar PV power used [MW]	$pp_{SS}(dd)$
Grid Power used [MW]	$pp_{GG}(dd)$
Electrolyzer hydrogen production rate [kg/s]	$m\dot{m}_{EEEE}(dd)$
Electrolyzer mass flow to Liquefier [kg/s]	$m\dot{m}_{EEEEEE}(dd)$
Electrolyzer mass flow to 350 bar buffer storage tank [kg/s]	$m\dot{m}_{EEEEEE}(dd)$
Mass flow from 350 bar buffer tank to Liquefier [kg/s]	$m\dot{m}_{EEEE}(dd)$

The binary decision variables are mentioned below in table 4: $dd = 1, \dots, TT$. These binary decision variables are introduced to represent the discrete (on/off) operation of the main cryogenic pump and main compressor, which cannot be captured realistically using only continuous flow variables. The start-up and shut-down flag variables are included to explicitly capture transitions between operating states from one time step to the next. This enables the model to quantify and penalize frequent cycling, which is undesirable in practice due to increased wear, reliability concerns, and potential efficiency losses during transients. These transition flags also support the implementation of operational logic such as minimum up-time and minimum down-time constraints, ensuring that once a unit starts it must remain on for a specified duration (and similarly remain off after shut-down).

3.3.3. Continuous Design Variables

Table 6. List of continuous design decision variables for MILP optimization.

Description	VVVVVVVVVVVVVVVVVVVV
2-phase cryogenic storage mass [kg]	MM_{tank}
350 bar Buffer storage tank sizes [m ³]	VV_{350}
900 bar Buffer storage tank sizes [m ³]	VV_{900}
Initial Liquid hydrogen inventory in cryogenic storage [kg]	$MM_{\text{liq},0}$
Liquefier hydrogen mass flow production rate [kg/s]	$m\dot{m}_{EELLLLLLLLLLLLLLLLL}$
Electrolyzer capacity [MW]	EE

3.4. Constraints

Two-phase cryogenic tank mass balance accounts for the combined liquid and vapor inventory changes due to liquefier inflow and hydrogen dispensing through the pump and compressor. Venting is avoided because it is undesirable in normal operation; instead, the optimization is designed to keep the tank pressure within the target operating range so that routine day-to-day operation can be achieved with minimum vent losses. The mass balance constraints from the thermodynamic model and multi-linear regression are:

$$MM_{\text{liq}}(dd) + MM_{\text{vap}}(dd) = MM_{\text{liq}}(dd - 1) + MM_{\text{vap}}(dd - 1) + m\dot{m}_{EELLLLLLLLLLLLLLLLL} \Delta dd - \eta_{ppLLDDpp} m\dot{m}_{pp}(dd) \Delta dd - m\dot{m}_{cc}(dd) \Delta dd$$

$$MM_{\text{liq}}(dd) = MM_{\text{liq}}(dd - 1) + m\dot{m}_{EELLLLLLLLLLLLLLLLL} \Delta dd - \eta_{\text{pump}} m\dot{m}_{pp}(dd) \Delta dd - m\dot{m}_{\text{boil}}(dd) \Delta dd$$

$$MM_{\text{vap}}(dd) = cc_{v1} MM_{\text{liq}}(dd) + bb_{v1} \text{ where } cc_{v1} = -0.049258 \text{ and } bb_{v1} = 64.606164$$

The cryogenic tank pressure is approximated as a linear function of liquid and vapor mass as both impact the tank pressure. Vapor compression and ullage volume change as the mass of liquid impacts the tank pressure, as discussed in section 2.3. The cryogenic tank is made to operate between 80 and 100 psi (around 5.5 to 6.9 bar) so any schedule of pump, compressor and liquefier

operating condition that would drive the pressure outside this range is automatically rejected as infeasible. MM_{tank} is a single scalar decision variable (same for all timesteps) and it is used to represent the nameplate mass capacity of the cryogenic tank in kg. The MILP optimization algorithm constrains the sum of liquid and vapor mass at each timestep to be less than or equal to this nameplate capacity. The tank capacity itself is bound between a minimum of 300 kg and a maximum of 1000 kg (50% of the daily demand) value based on design limits to provide some buffer against liquefier outages. To avoid unrealistically empty or completely flooded operating points, the liquid inventory in the cryogenic tank is restricted to a fraction of the nameplate capacity. The lower bound of 50% ensures that the tank is not operated at very low liquid levels. The upper bound represents a practical maximum fill level (85% of nameplate), leaving space for vapor/ullage. Finally, to represent steady daily operating pattern, the liquid inventory is enforced to be cyclic over the 24-hour horizon, i.e. the liquid mass at the end of the horizon returns to its initial value. This periodicity constraint means the optimizer must choose a tank size and operating schedule such that the system can repeat the same 24-hour pattern indefinitely without gradually emptying or overfilling the tank.

$$PP_{\text{tank}}(dd) = pp_{cc0} + pp_{ccMM_{vv}} MM_{\text{vap}}(dd) + pp_{ccMM_{ll}} MM_{\text{liq}}(dd)$$

$$\text{where } pp_{cc0} = -39.518011, pp_{ccMM_{vv}} = 1.547402, pp_{ccMM_{ll}} = 0.118230$$

$$80 \leq PP_{\text{tank}}(dd) \leq 100$$

$$MM_{\text{liq}}(dd) + MM_{\text{vap}}(dd) \leq MM_{\text{tank}}$$

$$0.50 MM_{\text{tank}} \leq MM_{\text{liq}}(dd) \leq 0.85 MM_{\text{tank}}$$

Cryogenic tank nameplate capacity: $300 \leq MM_{\text{tank}} \leq 1200$ [kg]

For a 24-hour horizon, $T = 288$ steps of 5 minutes, the optimization is modelled such that the liquid mass at the end of the day returns to its initial value,

$$MM_{\text{liq}}(TT) = MM_{\text{liq},0}$$

900 bar gaseous hydrogen buffer volume tank: $10 \leq VV_{900} \leq 30$ [m³]

900 bar gaseous hydrogen buffer mass: $MM_{900, \text{min}} \leq MM_{900}(dd) \leq MM_{900, \text{max}}$ where VV_{900} is the given tank volume and the usable density is calculated using REFPROP at 298K for $PP_{\text{min}} = 820$ bar and $PP_{\text{max}} = 900$ bar.

Initial gaseous buffer mass: $MM_{900}(1) = MM_{900, \text{min}} + 0.30 \diamond MM_{900, \text{max}} - MM_{900, \text{min}} \diamond$

Gaseous hydrogen buffer mass balance for each time step $t = 2, \dots, T$

$$MM_{900}(dd) = MM_{900}(dd - 1) - \dot{m}_{DLLLLDDDDDDDD}(dd) + \eta_{pp} \dot{m}_{pp}(dd) \Delta dd + \eta_{cc} \dot{m}_{cc}(dd) \Delta dd$$

Where \dot{m}_{demand} is required dispensing flow rate to vehicle tank, $\eta_{pp} = 0.95$ is pump mass efficiency, $\eta_{cc} = 1$ is compressor mass efficiency. This means that cryogenic pump generates 5% boil-off and only dispenses 95% of total mass flow whereas compressor dispenses without any mass loss. This is due to cryogenic pump operation mechanism and utilization as explained in section 2.5.

Physically, most large pumps and compressors cannot operate stably at arbitrarily small flow rates; below some fraction of their design capacity they may suffer from poor efficiency, overheating and unstable operation. The factor 0.05 is provided as a minimum turndown ratio and allows flow only if it is ON and must operate between 5-100% of its nameplate.

Pump nameplate capacities: $0.02 \leq ccccp_{pp} \leq 0.09$ [kg/s]

Compressor nameplate capacities: $0.01 \leq ccccp_{cc} \leq 0.025$ [kg/s]

$$0.05 ccccp_{pp} x_{pp}(dd) \leq \dot{m}_{pp}(dd) \leq ccccp_{pp} x_{pp}(dd), \quad \forall dd$$

$$0.05 ccccp_{cc} x_{cc}(dd) \leq \dot{m}_{cc}(dd) \leq ccccp_{cc} x_{cc}(dd), \quad \forall dd$$

HRS rotating equipment like pumps and compressors cannot instantly transition from a low mass flow rate to a high mass flow rate. Their mechanical and thermal design have maximum allowable rate of change of flow. To model this realistically, the MILP assumes a maximum ramp rate between consecutive time steps.

Pump Ramp up limit: $\dot{m}_{pp}(dd) - \dot{m}_{pp}(dd - 1) \leq rr_{pp} ccccp_{pp} \Delta dd / 60$

Pump ramp down limit: $\dot{m}_{pp}(dd - 1) - \dot{m}_{pp}(dd) \leq rr_{pp} ccccp_{pp} \Delta dd / 60$

Compressor Ramp-up limit: $\dot{m}_{cc}(dd) - \dot{m}_{cc}(dd - 1) \leq rr_{cc} ccccp_{cc} \Delta dd / 60$

Compressor ramp-down limit: $\dot{m}_{cc}(dd - 1) - \dot{m}_{cc}(dd) \leq rr_{cc} ccccp_{cc} \Delta dd / 60$

Allowable Ramp fraction per minute: $rr_{pp} = rr_{cc} = 0.05$, which means 5% of capacity per minute or up to 25% of its nameplate capacity per time step of 5 minutes.

In addition, this equipment cannot be cycled ON/OFF rapidly and each unit requires some minimum up-time and down-time to work efficiently. This is to avoid thermal and mechanical damage due to excessive wear and failure. These rules are implemented using ON/OFF state and start-up/shut-down flags.

Minimum down time constraint for the main Pump and compressor is:

Pump: $x_{pp}(dd + 1 + ii) \leq 1 - ooooo_{pp}(dd)$, $ii = 0, \dots, N_{pp}^{DDccwueDD} - 1$

Compressor: $x_{cc}(dd + 1 + ii) \leq 1 - ooooo_{cc}(dd)$, $ii = 0, \dots, N_{cc}^{DDccwueDD} - 1$

When a unit shuts down at time t , $o_{pp}(dd) \text{ or } o_{cc}(dd) = 1$ and it must stay OFF for the next $NN_{pp}^{D_{ccw}DD}$ or $NN_{cc}^{D_{ccw}DD}$ time steps. The typical values used in the MILP are $NN_{pp}^{D_{ccw}DD} = 36 \text{ ssdeeppss}(3 \text{ hoourrss})$ and $NN_{cc}^{D_{ccw}DD} = 24 \text{ ssdeeppss}(2 \text{ hoourrss})$.

Similarly for the minimum up-time constraint, once the unit starts at time t , $o_{pp}(dd) \text{ or } o_{cc}(dd) = 1$, it must remain ON for at least $NN_{pp}^{L_{pp}}$ or $NN_{cc}^{L_{pp}}$ time steps.

Pump: $x_{pp}(dd + ii) \geq o_{pp}(dd)$, $ii = 0, \dots, NN_{pp}^{L_{pp}} - 1$

Compressor: $x_{cc}(dd + ii) \geq o_{cc}(dd)$, $ii = 0, \dots, NN_{cc}^{L_{pp}} - 1$

When a unit starts at time t , the typical values are $NN_{pp}^{L_{pp}} = 36 \text{ ssdeeppss}(3 \text{ hoourrss})$ and $NN_{cc}^{L_{pp}} = 24 \text{ ssdeeppss}(2 \text{ hoourrss})$.

The equation below shows how much Solar PV power is available at each time step,

$$pp_{SS}^{av}(dd) = SS_{DDDDmm} CCCCP_{PV}(dd)$$

Where $pp_{SS}^{av}(dd)$ is PPV $pp_{o_{weerr}}$ $ccv_{cciaacbbaae}$ $ccdd$ dd_{iimmee} dd , SS_{DDDDmm} is PV nameplate capacity and $CCCP_{PV}$ is PPV $ccccppccciidd$ $o_{cccccdoorr}$ $(0 - 1)$, $v_{ccrrdiinnuv}$ o_{vveerr} dd_{iimmee} .

The PV array has a nominal size of 3MW, however due to clouds transients, irradiance and day/night cycles, the PV is not always at full production. The variable $CCCP_{PV}$ is used in the modelling to account for solar power fluctuations and it gives the actual PV power available at each timestep. The MILP constraint given below allows the optimizer decide how much PV power to use but it cannot exceed what is physically available.

$$0 \leq pp_{SS}(dd) \leq pp_{SS}^{av}(dd), \quad \forall dd$$

In the integrated PV-electrolyzer-grid model, the optimizer system can draw up to the firm grid limit under normal conditions but is required to operate without any grid import during an outage period. Grid import $pp_{GG}(dd)$ is bounded by the grid capacity $pp_{GG}(dd)$ set to 15MW under normal operation and forced to zero during specified outage interval. This allows optimizer to strategically balance PV use, grid import and electrolyzer operation.

$$0 \leq pp_{GG}(dd) \leq pp_{GG}(dd), \quad \forall dd$$

The HRS require electrical power to operate multiple subsystems responsible for liquefaction, pumping, compression, and vaporization. The optimizer must account for each components power demand at every time step. The total HRS electrical load is modeled as the sum of all major energy consuming processes:

$$pp_{HRS}(dd) = pp_{pump}(dd) + pp_{boost}(dd) + pp_{comp}(dd) + pp_{ppLLDDpp,tlL}(dd) + pp_{ELLLLLLLLLLLLLLLL}(dd) + pp_{vap}(dd) + pp_{vapC}(dd)$$

Where power of each component is calculated by calculating the SEC (kWh/kg) and multiplying it with mass flow rate (kg/s).

At every time step, the total system electrical input to the electrolyzer, 350 bar compressor and HRS components load must be supplied by PV and grid.

$$ee(dd) + pp_{\text{comp}}(dd) + pp_{\text{HRS}}(dd) = pp_{\text{SS}}(dd) + pp_{\text{GG}}(dd), \quad \forall dd$$

The electrolyzer converts the electrical power into hydrogen and its electrical input $ee(dd)$ is restricted by the installed nameplate capacity E . This constraint ensures the optimizer can not exceed the physical maximum rating of the electrolyzer stack. When renewable power is abundant and grid is stable, it can run at full load while during outage, it may drop to zero.

$$0 \leq ee(dd) \leq EE, \quad \forall dd$$

Hydrogen production is modeled using the 1MW reference electrolyzer performance curve with hourly variable solar power input as mentioned in section 4.2. The hydrogen mass flow is assumed proportional to the electrical power input and kk_{ELX} is the hydrogen production coefficient (kg/s per MW) obtained from the dataset from the electrolyzer model. This creates linear power to hydrogen mapping, which simplifies the MILP structure while remaining consistent with real PEM electrolyzer performance.

$$m\dot{m}_{\text{EEEE}}(dd) = kk_{\text{ELX}} ee(dd), \quad \forall dd$$

The hydrogen produced by the electrolyzer must be divided between two possible downstream units, the liquefier unit and the 350 bar buffer tank. This enforces mass conservation, so every kilogram of hydrogen produced must go either to liquefaction or to the 350 bar buffer tank.

$$m\dot{m}_{\text{EEEEEE}}(dd) + m\dot{m}_{\text{EEEEEE}}(dd) = m\dot{m}_{\text{EEEE}}(dd), \quad \forall dd$$

$$m\dot{m}_{\text{EEEEEE}}(dd) \geq 0, \quad m\dot{m}_{\text{EEEEEE}}(dd) \geq 0, \quad \forall dd$$

The MILP operational strategy is modelled to supply the liquefier continuously at a fixed mass flow rate as calculated by the optimization, either from the electrolyzer output or from the 350-bar buffer tank.

The 350-bar buffer tank plays a crucial role in smoothing the mismatch between electrolyzer hydrogen production and liquefier demand. The tank absorbs surplus gaseous hydrogen when renewable power generation is high and supplies hydrogen to the liquefier during grid-outage or low power supply periods. To model a repeating daily operating cycle, the buffer tank must end the horizon with the same mass it started with.

$$MM_{350}(dd + 1) = MM_{350}(dd) + \Delta dd \diamond m\dot{m}_{\text{EEEEEE}}(dd) - m\dot{m}_{\text{EEEE}}(dd) \diamond$$

$$MM_{350}(1) = MM_{350}(TT) + \Delta dd \diamond m\dot{m}_{\text{EEEEEE}}(TT) - m\dot{m}_{\text{EEEE}}(TT) \diamond$$

The 350-bar buffer tank volume is a decision variable. For a given volume, REFPROP provides the hydrogen density range at storage temperature of 298 K and allowable pressure window of 320-350 bar.

$$\rho_{DdLLDD}^{350} V_{350} \leq MM_{350}(dd) \leq \rho_{DDDDmm}^{350} V_{350}$$

$$0 \leq V_{350} \leq 50 \quad \text{m}^3$$

3.5. Capacity factor

The capacity factor is defined as the ratio between the actual energy used (or hydrogen produced) over a year and the theoretical maximum if the unit operated at its nameplate rating for all hours. For the electrolyzer, this is the ratio of the time-varying electrical input (integrated over the horizon) to the product of nameplate power and total time. The same definition applies to the liquefier and the hydrogen pumps/compressors, using their respective power draws and rated capacities. In other words, a capacity factor close to 1 or 100% means the equipment is fully utilized, while a low value indicates that expensive assets sit idle for a large fraction of the time. In this model, the capacity factor is not a part of MILP and is calculated afterwards using the optimization results. The key focus was to create an operational strategy to increase the capacity factor of electrolyzer and liquefier. The electrolyzer capacity factor is calculated using the relation:

$$CF_{EEEEEE} = \frac{\sum_{t=1}^T e(t)\Delta t}{EE \times 24h}$$

3.6. Capital and Operating Cost (CAPEX & OPEX) Modeling

The techno-economic optimization of the hydrogen refueling station must jointly consider the capital expenditure (CAPEX) of major equipment and the operating expenditure (OPEX) driven primarily by electrical energy consumption. All cost models follow standard cost correlations, multi-year cost escalation and MILP compatible linear or piecewise-linear structures. The general expression used to calculate the electrical energy cost is given below where cc_{elec} is electricity price (\$/kWh) and EE_{total} is total electrical consumption (kWh/day)

$$OPEX_{elec} = cc_{elec} EE_{total}$$

All capital costs follow HDSAM correlations[42], estimated CEPCI escalation or linearized approximations. Due to unavailability of actual CEPCI values, we used estimations which gives reasonable capital cost values for the target year.

The escalation to target year 2024 with CEPCI indices for all the components is:

$$CAPEX_{2024} = C_{2024} = C_{2013} \frac{CEPCI_{2024}}{CEPCI_{2013}}$$

For 900 bar gaseous buffer tank, $CC_{900,2013} = \$1800 / \text{kg}$

The main compressor, $CC_{\text{comp},2007} = 2404.1pp_{\text{comp}}(kkkk) + 166409$

$$CC_{\text{comp},\text{inst},2007} = 1.3 CC_{\text{comp},2007}$$

Liquid hydrogen (LH₂) pumps constitute a major portion of the hydrogen refueling station capital cost, especially for high-pressure dispensing. Pump costs used in this work are derived from the U.S. DOE HDSAM (Hydrogen Delivery Scenario Analysis Model) database, which provides empirical cost correlations for station pumps in hydrogen stations.

HDSAM station pump uninstalled cost for 700 bar dispensing, 2010 dollars = \$700,000 and a low pressure terminal pump used in liquefier upstream has uninstalled cost of \$135,000, 2014 dollars. The installation factor for both the pumps is mentioned to be 1.3.

Hydrogen liquefaction is the most capital-intensive component of this HRS and commercial scale liquefiers exhibit strong economies of scale and use multistage cryogenic refrigeration cycles. A simplified linear cost capacity correlation is used in MILP.

$$\text{Liquefier CAPEX, } CC_{\text{liq},2014} = 5.6 \times 10^6 (\text{TPD})^{0.8}$$

The above is a non-linear as $b < 1$ to reflect economies of scale. For MILP, we need to linearize to make it compatible, the liquefier cost is expressed as a linear function of the liquefier mass-flow variable where $m\dot{m}_{\text{liq}}$ (kg/s) is liquefier's design mass-flow rate and cc_{liq} is a constant derived from HDSAM.

This conversion yields a constant cost per unit liquefaction flow and using HDSAM liquefier cost CC_0 for a known reference size $m\dot{m}_0$.

$$cc_{\text{liq}} = \frac{CC_0}{m\dot{m}_0} [\$/(kkvv/ss)]$$

This constant is then directly used in the MILP objective function. The liquefier CAPEX in our MILP becomes:

$$CC_{\text{liq},2014} = cc_{\text{liq}} m\dot{m}_{\text{liq}}$$

The CAPEX calculation for Solar PV [43] and PEM electrolyzer system [44] is given below where SS_{DDDDmm} [MW] is PV nameplate capacity and EE [MW] is the optimized electrolyzer size.

$$\text{CAPEX}_{\text{PV}} = 1500/kkkk(SS_{DDDDmm} \times 1000)$$

$$CC_{\text{APEX}_{\text{ELX}}} = 1050/kkkk(EE \times 1000)$$

For 350 bar buffer tank as per HDSAM 2013 dollars,

$$CC_{350,2013} = 1560/kkvv \times MM_{350}$$

For the main cryogenic pump, the HDSAM database has only two reference cost points,

$$CC_{pump}^{2010} = \$ 425000 \text{ (350 bar)}$$

$$CC_{pump}^{2010} = \$ 700000 \text{ (700 bar)}$$

Since the pump discharge pressure is assumed to be around 550 bar in our case, we require a continuous function that estimates pump cost. Therefore, we use power-law scaling rule as mentioned below where KK_{pump} is scaling constant and nn_{pump} is scaling exponent. This method is more appropriate as pump cost does scale linearly with pressure, and it is widely used method.

$$m_{pump} = \frac{\ln (CC_2^{2010}/CC_1^{2010})}{\ln (700/350)}$$

$$KK_{pump} = \frac{CC_{pump}^{2010}}{350^{nn_{pump}}}$$

$$CC_{pump,2010} = KK_{pump} pp_{pump}^{nn_{pump}}$$

The same correlation was used for the transfer pump between liquefier and cryogenic tank.

Booster compressor CAPEX- Pump line

$$CC_{boost,2013} = 6000/kkkk \cdot pp_{boost}$$

Non-linear HDSAM correlation for cryogenic tank cost, $CC_{tank,2013} = 991.89 MM_{tank}^{0.6929}$

First, we choose a fixed reference capacity, MM_{ref} from first iteration and then evaluate the non-linear HDSAM formula only at this fixed size. Then we applied for the installation fraction an cost escalation and convert to \$/kg based on that reference size. Lastly, we use a linear model for any tank size in MILP, where the MM_{tank} is a decision variable and the coefficient $cc_{tank}^{$/kg}$ is constant.

$$CC_{tank,2013}(MM_{ref}) = 991.89 MM_{ref}^{0.6929}$$

$$cc_{tank}^{$/kg} = \frac{CC_{inst}^{2024}(MM_{ref})}{MM_{ref}}$$

$$CC_{tank,2013}(MM_{tank}) = cc_{tank}^{$/kg} MM_{tank}$$

The Vaporizer CAPEX for pump and compressor line as per HDSAM 2013 dollar with 1.3 installation factor. We use mm_{pp} for pump-line vaporizer and mm_{cc} for compressor-line vaporizer.

$$CC_{vap,2013} = cc_{vap} mm_{pp} + bb_{vap}, \text{ where } cc_{vap} = 1000 (kkvv/h), bb_{vap} = 15000$$

3.7. Objective Function

The overall goal of the integrated hydrogen production, storage and refueling station is to determine the optimal sizing and operation of the electrolyzer, liquefier, cryogenic tank, pump, compressor and buffer storage tanks, while minimizing the technical parameters like boil-off, energy consumption, pump and compressor on/off transitions and economic metrics of capital and operating costs. The optimization problem is solved in two interacting subsystems with each subsystem having its own objective function. The energy requirements of Subsystem 1 are added to the Subsystem 2 for the whole system analysis.

1. **Subsystem 1:** Hydrogen Refueling Station Dispensing Components
2. **Subsystem 2:** Electrolyzer + Grid + PV

For Subsystem 1, $J_{\text{HRS}}^{\text{cost}}$ is the sum of installed CAPEX for all the dispensing components and $J_{\text{HRS}}^{\text{tech}}$ is sum of cryogenic pump boil-off, on/off transitions for pump/compressor penalty cost, and total electrical energy consumption. $E_{\text{HRS}}^{\text{lin}}$ represents the sum of all electrical components from Subsystem 1, where ii (pump, booster compressor, vaporizer, liquefier, etc.), and this is linearized by using SEC values (kWh/kg) for the MILP optimization. For the pump-only case, as discussed in section 4.6.3, the CC_{vent} penalty is added to $J_{\text{HRS}}^{\text{tech}}$ to minimize the vent losses from the cryogenic tank.

$$J_{\text{Subsystem 1}} = J_{\text{HRS}}^{\text{cost}} + J_{\text{HRS}}^{\text{tech}}$$

$$J_{\text{HRS}}^{\text{cost}} = CC_{\text{LH2 tank}} + CC_{\text{EELLLLLLLLLLLLLLLLL}} + CC_{\text{pump}} + CC_{\text{comp}} + CC_{900} + CC_{\text{vapP}} + CC_{\text{vapC}}$$

$$J_{\text{HRS}}^{\text{tech}} = CC_{\text{boil}} + CC_{\text{transition}} + EE^{\text{lin}}$$

$$CC_{\text{boil}} = \sum_{tt=1}^{EE} (1 - \eta_{\text{pump}}) m_{pp}(dd) \Delta dd$$

$$CC_{\text{transition}} = cc_{\text{pump,trans}} (NN_{\text{on,pp}} + NN_{\text{off,pp}}) + cc_{\text{comp,trans}} (NN_{\text{on,cc}} + NN_{\text{off,cc}})$$

$$E_{\text{HRS}}^{\text{lin}} = \sum_{LL} SSEECC_{LL} \sum_{tt=1}^{EE} m_{LL}(dd) \Delta dd$$

For Subsystem 2, the CC_{PV} is CAPEX for the solar PV plant, CC_{ELX} is the capital cost for PEM electrolyzer as per optimized nameplate capacity, and CC_{grid} is the ToD grid cost of buying electricity. The CC_{350} and $CC_{\text{comp},350}$ are the capital cost terms for the 350-bar buffer tank and the compressor feeding compressed hydrogen to this tank from the electrolyzer respectively.

$$J_{\text{SSLLSSssyyssstLLDD 2}} = CC_{\text{PV}} + CC_{\text{ELX}} + CC_{\text{grid}} + CC_{350} + CC_{\text{comp},350}$$

Chapter 4. Results and Discussion

4.1. Vehicle Arrival and Variable Station Demand

To evaluate station operation under realistic usage, a synthetic 24-hour demand profile was generated starting from detailed single-tank refueling data. Instead of assuming a simple constant or piecewise-constant demand, the model explicitly reconstructs the mass-flow history of each vehicle refueling event and superimposes multiple events over the day according to a stochastic arrival process. The total mass delivered to a single tank is computed as the time integral of the mass flow data from the H2Fills simulation data.

In this work a vehicle is defined as a set of 10 identical onboard tanks refueled together with the same single-tank profile. Then the station load (kg/day) is then translated into an integer number to complete vehicle fills per day.

Vehicle arrival times are generated as a stochastic point process over the 24-hour horizon. The day is divided into a daytime window with higher traffic (06:00-22:00) and two low-traffic night windows (00:00-06:00 and 22:00-24:00). The model specified the fraction of daily vehicles assigned to the daytime period i.e., 80% of the refueling between 06:00 and 22:00.

A single-dispenser constraint is imposed with 5-minutes of linger time between vehicle refueling representing hose disconnection, payment and pull away time. The cumulative sum of $mm_{\text{demand}}(dd)$ yields the cumulative daily demand curve (red line) which approaches the target station demand of 2TPD by the end of the horizon.

The hourly histogram of completed refueling vehicle counts and cumulative hydrogen mass dispensed are shown in figure 13 and is generated using stochastic model.

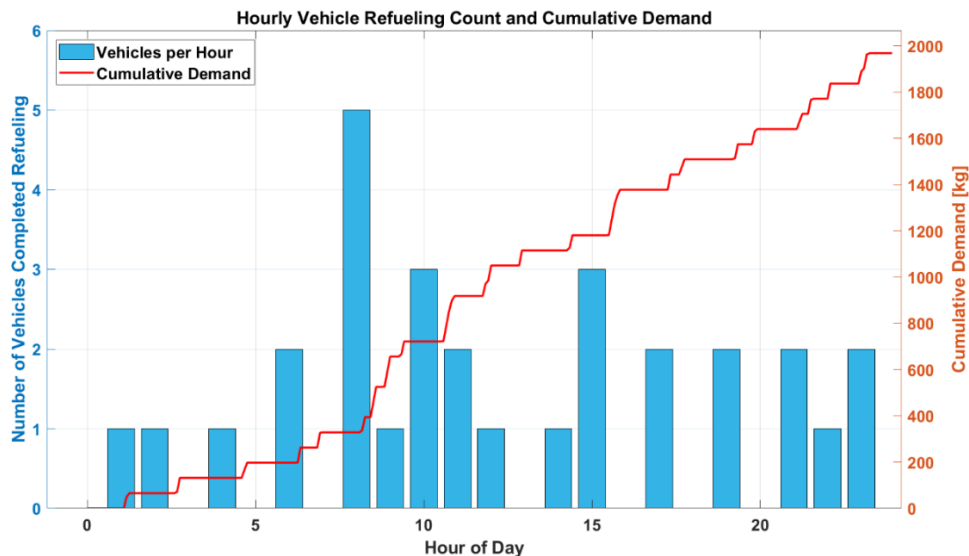


Figure 13. Hourly vehicle refueling count and cumulative hydrogen station demand

4.2. PEM Electrolyzer Hydrogen Production

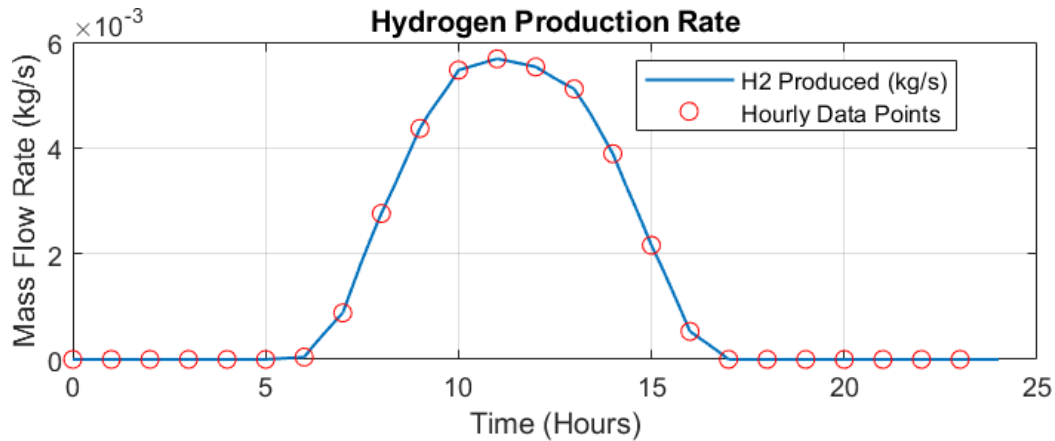


Figure 14. Gaseous hydrogen production rate from 1MW PEM electrolyzer following the hourly solar power variable input.

Figure 14 shows the hydrogen production mass flow rate for a 1MW PEM electrolyzer with solar energy input. The solar energy provides 1MW at noon and the PEM electrolyzer runs full capacity producing around 0.005 kg/s peak hydrogen mass flow at 35 bar. This gives if the 1 MW PEM is run on full capacity for 24 hours then it will produce 432 kg of hydrogen. This data is well aligned with data from Plug Power 1 MW PEM electrolyzer generating max hydrogen of 425 kg/day.[45]

The optimization uses the interpolated mass flow rate data as a reference shape and scaling basis for electrolyzer hydrogen production over the 24-hour horizon. After loading the data, the code extracts single production yield from the profile by taking the maximum hydrogen flow rate observed in 1 MW dataset. This maximum value is treated as the nominal conversion from electrical power to hydrogen production (i.e., how many kilograms per second per MW the electrolyzer can produce). The profile is also normalized by this maximum to form a capacity-factor-like curve between 0 and 1. In this particular implementation, that normalized curve is used mainly to build a realistic time-varying renewable availability signal (it is multiplied by the winter derate factor and additional cloud/fog disturbances), which produces the time series of available PV power over the day.

Within the MILP itself, the optimizer decides the electrolyzer electrical input power at each timestep based on (i) PV available, (ii) grid limits and time-of-day electricity price, and (iii) the need to meet the fixed liquefier inlet flow while respecting GH₂ tank inventory limits. The corresponding hydrogen production rate is then computed by linearly scaling the chosen electrolyzer power using the nominal yield derived from the 1 MW dataset.

4.3. H2Fills Vehicle Tank Refueling Simulation

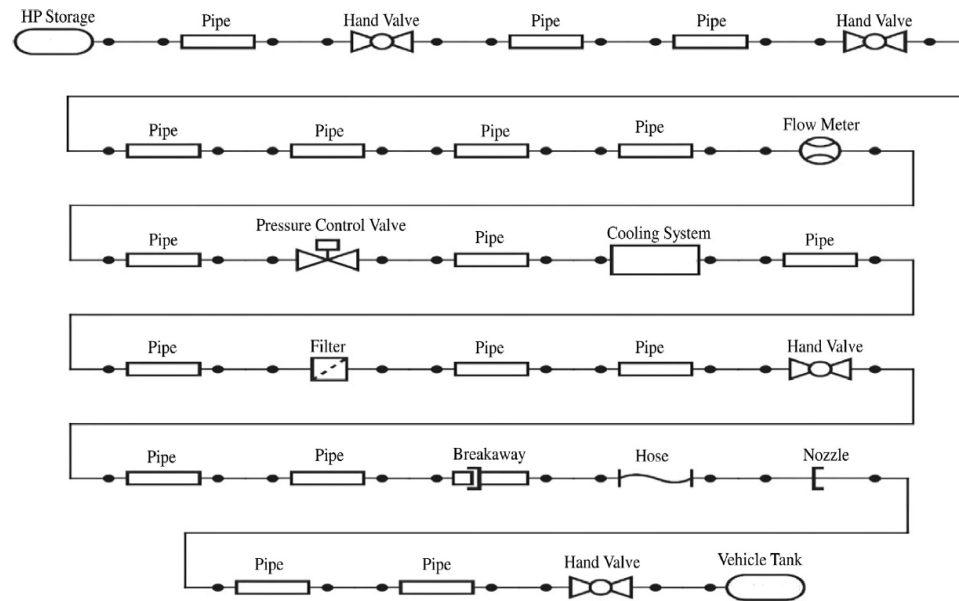


Figure 15. NREL single tank HRS detailed model schematic from H2Fills simulation.

H2Fills [46] is a Hydrogen Filling Simulation software that uses thermodynamic model to understand the transient change in hydrogen temperature, mass flow and pressure when filling a FCEV. The key input parameters for the simulation are shown in Table 7. For other details and modelling specifications the standard NREL's configuration was used with no other changes. [47]

Table 7. H2Fills modelling input parameters for HRS.

Parameters	Value
HP Bank Pressure	85 MPa
Ambient Temperature	25°C
Pressure Ramp Rate	18.5 MPa/min
Fuel Delivery Temp	-40°C
Terminating Pressure	81 MPa

Table 8. H2Fills modelling input parameters for vehicle tank.

Parameters	Value
Vehicle Tank type	Type IV
Single Vehicle Tank Size	7 kg
Vehicle Tank Initial Pressure	2 MPa
Soak Temperature	23°C
Length	1 m
Diameter	0.513 m

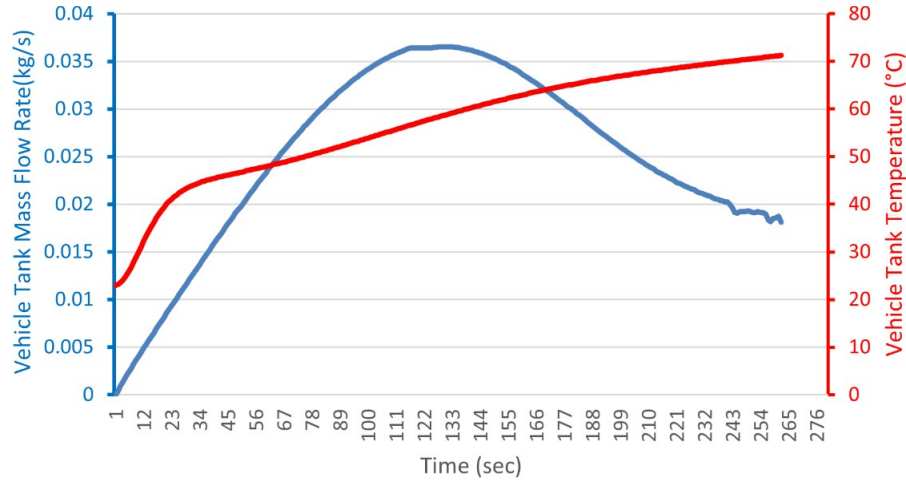


Figure 16. Hydrogen Mass flow rate and Temperature for Vehicle Tank Refilling from H2Fills.

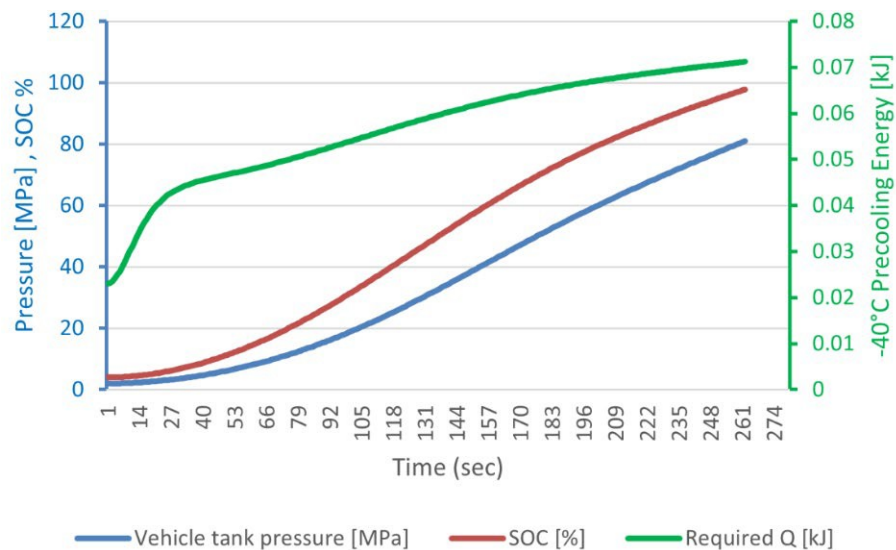


Figure 17. Hydrogen Vehicle Tank Pressure, State of Charge and Precooling Energy requirement for Refilling from H2Fills.

As shown in Figure 3 that Hyundai Xcient Truck has a total capacity of 68.6kg with total of 10 tanks. So, we chose the vehicle tank of 7kg in the H2Fills simulation and scaled the mass flow rate data 10-fold assuming all the tanks have the same initial conditions, and they are refilled in parallel at the same time until the termination conditions are reached.

Figure 16 and 17 shows that initially the mass flow rate ramps quickly towards around 0.035 kg/s due to large pressure difference between the High-Pressure storage bank and vehicle tank. It also shows rapid hydrogen temperature rise as cold hydrogen at -40°C enters a warm tank and increases

with a steady rate after some time. Figure 17 shows state of charge increase with increase of hydrogen mass in the tank. The SOC is ratio of hydrogen density at final pressure and temperature to the hydrogen density at 70MPa and 15°C. [13]

$$\text{SOC} = \frac{\rho_{\text{HH}_2}(T_{\text{final}}, p_{\text{final}})}{\rho_{\text{HH}_2}(15^\circ\text{C}, 700\text{bar})}$$

At around 35% SOC, the tank pressure has increased significantly and due to shrinkage of pressure difference the mass flow rate starts to reduce. This shows that mass flow rate decreases after certain pressure is due to decrease of compressibility of hydrogen and reduced free volume and temperature keeps rising due to compression heating.

4.4. Cryogenic Tank Modelling Results

Table 9. The key inputs for the 2-phase cryogenic storage tank model.

Parameters	Value
Total volume	12 m ³
Radius	1 m
Liquid Hydrogen inlet flow rate	0.025 kg/s
Liquid Hydrogen inlet pressure	110 psi
Liquid Hydrogen outlet flow rate	0.05 kg/s
Initial Tank pressure	80 psi
Initial Liquid Temperature	20 K
Initial Total mass (Liquid and vapor)	300 kg
Environmental Heat Leak to Liquid	50W
Environmental Heat Leak to Vapor	40W

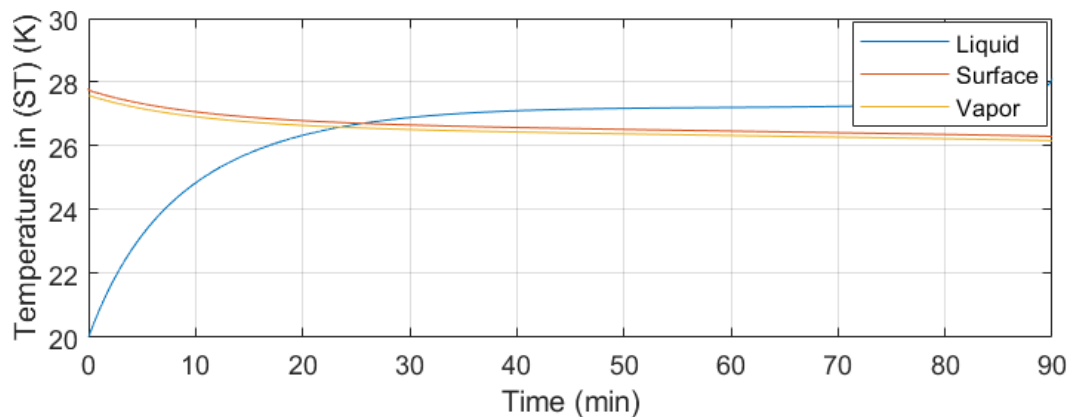


Figure 18. Temperature transition of liquid, vapor and interface film in the cryogenic tank.

The temperature plot figure 18 shows the changes in temperature of liquid, vapor and interface film. Initially, liquid hydrogen is at about 20 K, while the vapor and film temperatures are at 27 K.

As the heat flows from the warmer vapor and wall region into the cold liquid, the liquid temperature rises quickly and the vapor/film temperature decreases. As shown in the energy balance equation, the heat leak is constant but when the liquid mass keeps on decreasing as the inlet flow rate is kept at 0.025 kg/s to model replenishment from liquefier while the outlet flow rate is 0.05 kg/s reflecting near mean pump flow rate, the liquid specific internal energy and temperature rises. Film temperature is tied to vapor pressure via Osipov-type relaxation, as pressure drops the surface temperature also drops. Vapor temperature is computed from specific internal energy and density of vapor and vapor energy balance has condensation enthalpy term resulting in mild vapor temperature drop. The vapor temperature drop also happens due to ullage volume increase and vapor density drop coupled with PdV expansion work. After roughly 30-40 mins all three temperatures approach one another and reach steady value of around 26-27K showing the tank reach towards a near-equilibrium state.

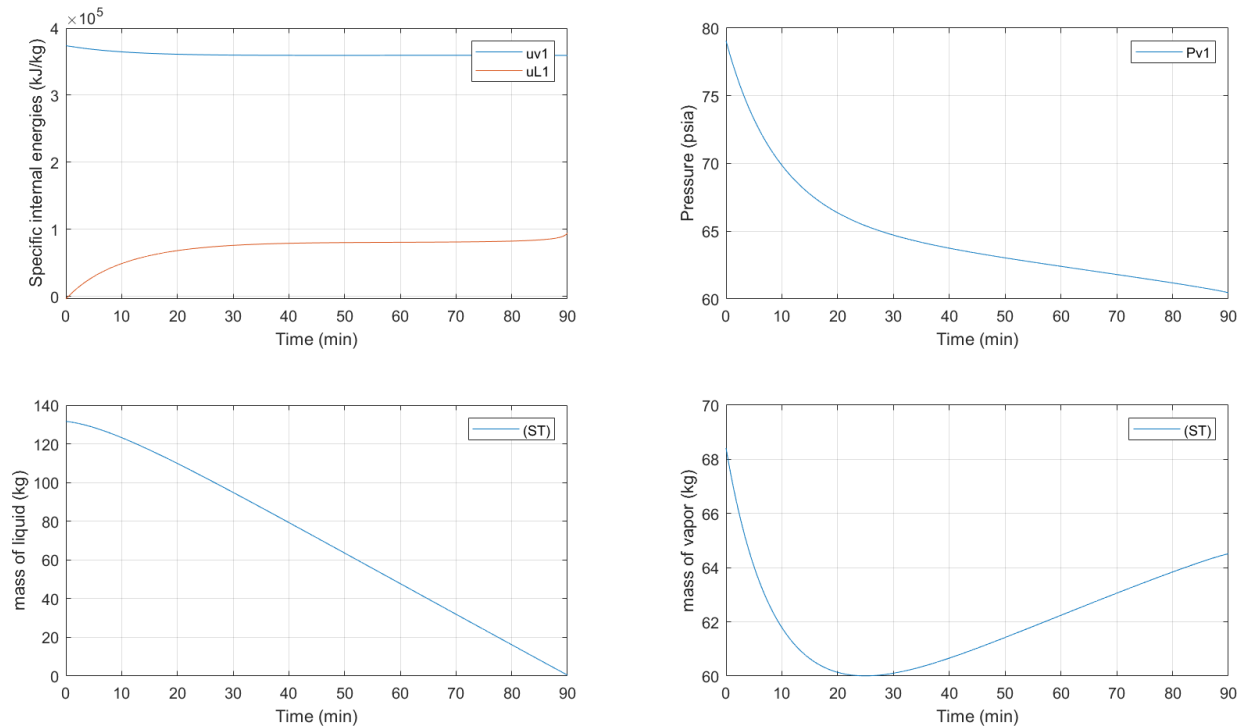


Figure 19. (a) Vapor and liquid specific internal energy (b) Tank Pressure (c) Liquid Hydrogen mass (d) Vapor mass from the cryogenic tank simulation.

Figure 19 (a-d) shows the rise in liquid internal energy as it heats up and the vapor's internal energy drop as it cools and partially condenses. Due to higher outlet flow rate, the mass of liquid hydrogen continues to drop. The vapor mass first drops rapidly showing strong condensation when the liquid temperature is much colder than the vapor with vapor energy losing due to condensation enthalpy and reaches minimum. Then vapor mass slowly increases as the tank warms up and some evaporation happens to keep vapor and liquid near equilibrium, while the liquid mass continues to be removed. The tank pressure drops because the liquid mass decreases due to the continuous

liquid dispensing and the ullage volume increases causing the vapor density and specific internal energy decrease.

To integrate the data from the 2-phase storage tank thermodynamic model with the MILP optimization framework, the non-linear dynamics are approximated using a set of algebraic relations between liquid mass, vapor mass, and tank pressure. The transient start-up data are excluded to eliminate non-equilibrium effects, and only steady-state linear operating points are used for regression. A simple linear relation is first derived between the liquid and vapor mass, followed by a multiple linear regression to derive an affine pressure map as function of both vapor and liquid mass. This approach preserves the essential coupling between tank inventory and pressure, while ensuring compatibility with the linear structure required by MILP. In the MILP framework, full two-phase thermodynamic tank model (state-dependent properties, saturation constraints, and iterative property calls) is computationally expensive and difficult to couple directly within a mixed-integer optimizer. To enable tractable optimization while still capturing the dominant coupling between tank inventory and pressure, an affine pressure mapping is introduced as a surrogate model.

In this optimization model the HRS includes a two-phase liquid hydrogen (LH₂) storage tank that acts as the central buffer between the upstream liquefier and the downstream dispensing equipment (cryogenic pump and compressor). The tank mass balance considers the liquid mass, vapor mass and tank pressure as time-dependent variables. The optimizer finds the optimal solution to meet these constraints while also determines the optimal tank nameplate capacity in kilograms of hydrogen adding liquid and vapor mass.

No explicit pressure-build-up unit (PBU) or vent off valve is modelled in this case; the tank pressure evolution is entirely driven by changes in the total mass and the linear mass-pressure mapping under the constraints given to the optimizer.

In the proposed model, the vapor phase hydrogen is extracted from the 2-phase cryogenic storage tank and compressed to the required pressure for the high pressure gaseous buffer tank used in dispensing. The optimizer determines the compressor mass flow rate at each time step, which is a decision variable $mm_{cc}(dd)$ (kg/s).

In the 2-phase storage tank, the hydrogen is stored near its saturation temperature of approximately 20 K. Before entering the multi-stage compressor, hydrogen vapor is withdrawn from the tank and then heated to near-ambient temperature at roughly constant pressure. Thermodynamic properties such as enthalpy and entropy for these states are obtained from REFPROP at the specified pressure and temperature.

4.5. Linear fits for the cryogenic tank

Figure 20 illustrates a multiple linear regression of tank pressure as a function of liquid mass and vapor mass. The blue markers are the operating data points from the thermodynamic simulation and data cleaning by removing initial transients until 40 minutes, and the translucent colored surface is the fitted regression plane. The close clustering of points around the plane indicates that, over the analyzed range, pressure varies approximately affinely with both state variables. The positive slope along the liquid-mass axis (and the slope with respect to vapor mass) quantifies each variable's contribution to pressure rise, and the small scatter about the plane suggests the linear map is adequate for embedding in the MILP constraints to enforce the 80-100 psi window.

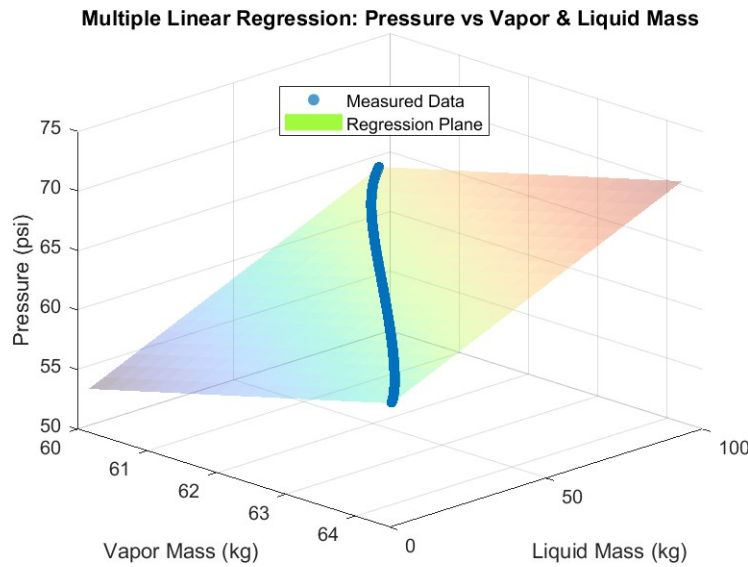


Figure 20. Multiple linear regression: cryogenic tank pressure, vapor mass and liquid mass.

$$MM_{\text{vap}}(dd) = cc_{\text{vl}} MM_{\text{liq}}(dd) + bb_{\text{vl}} \text{ [kg]}$$

$$cc_{\text{vl}} = -0.049258 \text{ and } bb_{\text{vl}} = 64.606164$$

$$PP_{\text{tank}}(dd) = pp_{\text{cc0}} + pp_{\text{ccMM}_{\text{vv}}} MM_{\text{vap}}(dd) + pp_{\text{ccMM}_{\text{ll}}} MM_{\text{liq}}(dd) \text{ [psi]}$$

$$\text{where } pp_{\text{cc0}} = -39.518011, pp_{\text{ccMM}_{\text{vv}}} = 1.547402, pp_{\text{ccMM}_{\text{ll}}} = 0.118230$$

4.6. Subsystem 1 Optimization – Dispensing

The optimization results of Subsystem 1 are discussed in this section. Two cases are discussed: i) case 1 considers the pump and the compressor both operating to replenish the 900-bar buffer tank from the cryogenic tank; ii) case 2 uses only the pump and a vent valve to maintain the cryogenic

tank pressure. For both cases the total mass dispensed to the vehicles remain same as 1968.62 kg. **4.6.1. With main pump and main compressor**

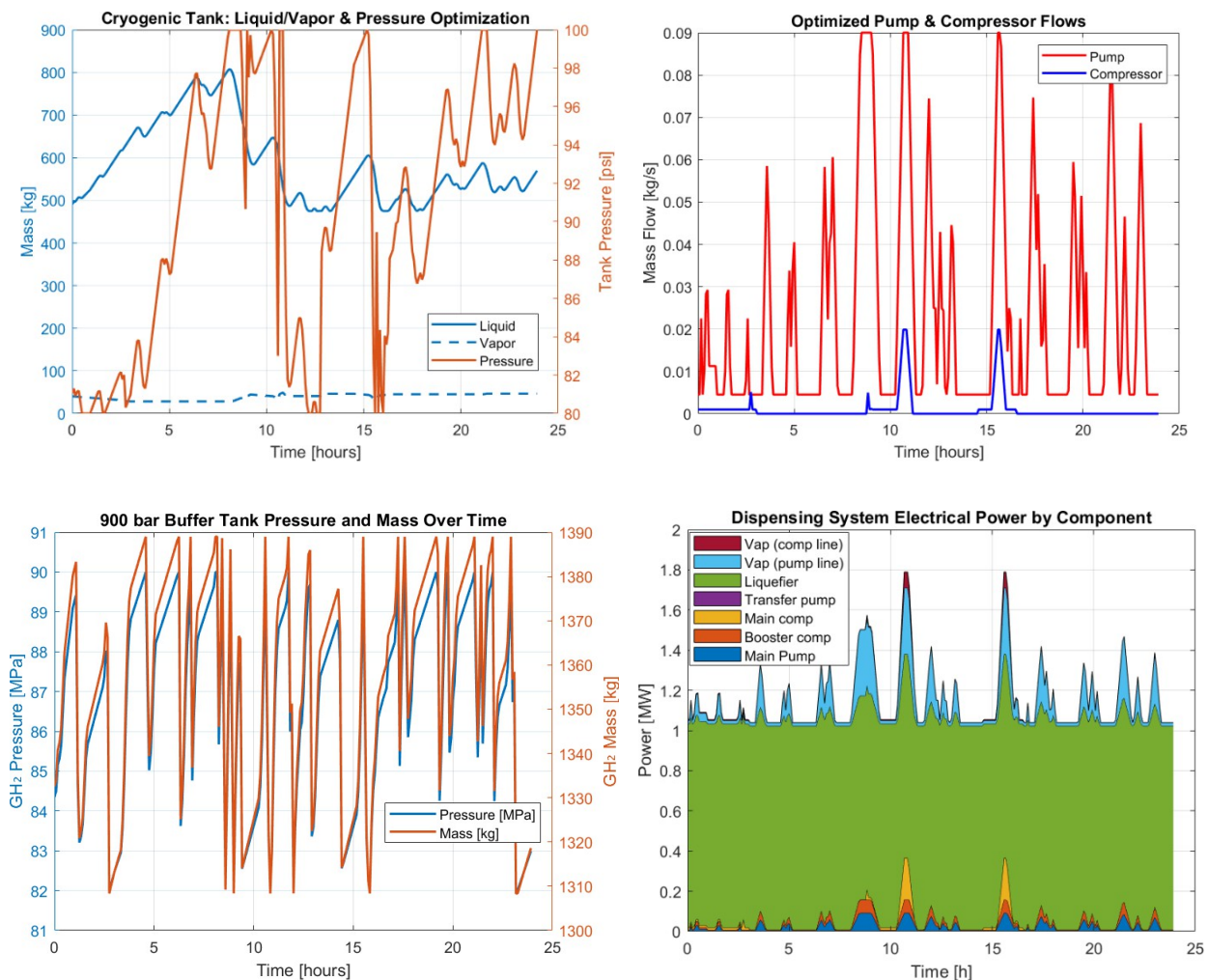


Figure 21. Case 1: (a) Liquid and vapor mass impact on cryogenic tank pressure. (b) Optimized Main pump and compressor flow rates. (c) 900 bar buffer tank mass and pressure dynamics. (d) Stacked plot showing electrical power demand for each dispensing component.

Figure 21(a) shows the behavior of the two-phase cryogenic storage tank that feeds the pump and compressor lines. The solid blue curve is the liquid mass, the dashed blue curve is the corresponding vapor mass from the linear correlation, and the orange curve is the tank pressure obtained from the affine map using vapor and liquid mass. At the start of the time horizon, the tank contains roughly 0.5 tons of liquid hydrogen with a small vapor inventory, and the pressure is close to the lower bound of the control range. During the early hours, when vehicle demand is low, the fixed liquefier inflow exceeds the withdrawal through the pump and compressor, so the liquid inventory rises steadily and approaches a maximum of about 0.8 tons. Over the same interval the vapor mass decreases slightly, because a portion of the initial vapor is drawn into the compressor, and the tank pressure increases from about 80 psi to almost 100 psi as the total tank mass increases.

As the day progresses and refueling demand increases, the pump and compressor start to withdraw more hydrogen than the liquefier supplies. Between approximately 8-12 h a period of intense refueling demand causes the liquid mass to drop by nearly 300 kg, after which the liquefier gradually rebuilds the inventory whenever the demand temporarily goes down. Despite these swings in liquid mass, the pressure remains tightly bounded within 80-100 psi, demonstrating that the combined effect of the liquid-vapor mass balances and the linear pressure map in the optimization model is sufficient to keep the tank within its allowable operating window. At the end of the time horizon, the masses are close to the initial values representing a daily cyclic operation.

Figure 21(b) illustrates the optimized dispatch strategy of the main cryogenic pump and compressor. The red curve represents the liquid hydrogen mass flow rate through the cryogenic pump, while the blue curve shows the gaseous hydrogen mass flow rate through the compressor. The pump is clearly the more active unit, operating in multiple intervals throughout the day at peak flow rates within the optimization constraints. When the 900-bar buffer tank is depleted faster than it can to be replenished, the optimizer increases the pump flow to withdraw additional liquid from the cryogenic tank, which is then vaporized and boosted into the buffer tank. Conversely, the compressor operates less frequently, and at lower flow rates, primarily to remove vapor from the cryogenic tank headspace and to adjust the pressure between refueling events. During the early low-demand hours, the compressor switches cycles intermittently to keep the cryogenic tank pressure within the 80-100 psi band, while the liquefier gradually builds liquid inventory. Around the morning and afternoon demand peaks, the compressor operates along with the pump, helping to supply additional mass to the buffer tank. Outside these peak windows, the compressor is mostly off, reflecting the fact that once the buffer is recharged and the tank pressure is within limits, additional compression work does not provide any benefit under the optimization objective.

The impact of refueling and replenishing of the 900-bar buffer tank is shown in Figure 21(c). The orange curve gives the buffer hydrogen mass and the blue curve the corresponding pressure obtained from REFPROP for the optimized buffer volume. The repeated saw-tooth pattern reflects alternating sequences of vehicle refueling and buffer recharge. Each drop in mass and pressure corresponds to one or more vehicles being filled; during these events the buffer pressure falls from the upper bound toward the lower bound of the design window. Once the immediate demand is satisfied, the combination of pump and compressor restores the buffer to its upper setpoint, producing the rising portion of each tooth. The large number of narrow teeth in the mass and pressure profiles is primarily a consequence of the 5-min time discretization used in the MILP model and each tooth represents a short refueling interval followed by a short recovery period. The upper buffer pressure is kept below 900 bar, while the lower bound is maintained above 820 bar to maintain the required pressure difference with the vehicle tank, which attains a maximum pressure of around 800 bar at full SOC as per the H2Fills tool simulations. Throughout the day, the buffer pressure remains within the prescribed 82-90 MPa window, confirming that the selected buffer volume and the optimized pump and compressor capacities are sufficient to cover all refueling peaks without violating the minimum pressure required to sustain flow into the vehicles.

Figure 21(d) presents the stacked electrical power consumption for each component on the dispensing side, i.e., components starting from the liquefier unit. The liquefier forms a nearly constant base load of about 1 MW over the entire 24 hour horizon, reflecting the fixed mass-flow production decision variable and significant high SEC of 11.9 kWh/kg. This corresponds to more than 87% of the total dispensing energy demand and pump-line vaporizer as the second-largest contributor reflecting the substantial enthalpy required to heat and fully vaporize the cryogenic liquid stream to ambient temperature at high pressure. The main cryogenic pump, booster compressor and main compressor consume relatively lower energy, and the compressor line vaporizer contributes very little, because the optimized compressor flow compared to the pumped flow operates over a smaller fraction of the horizon.

4.6.2 Sensitivity analysis of objective weightage

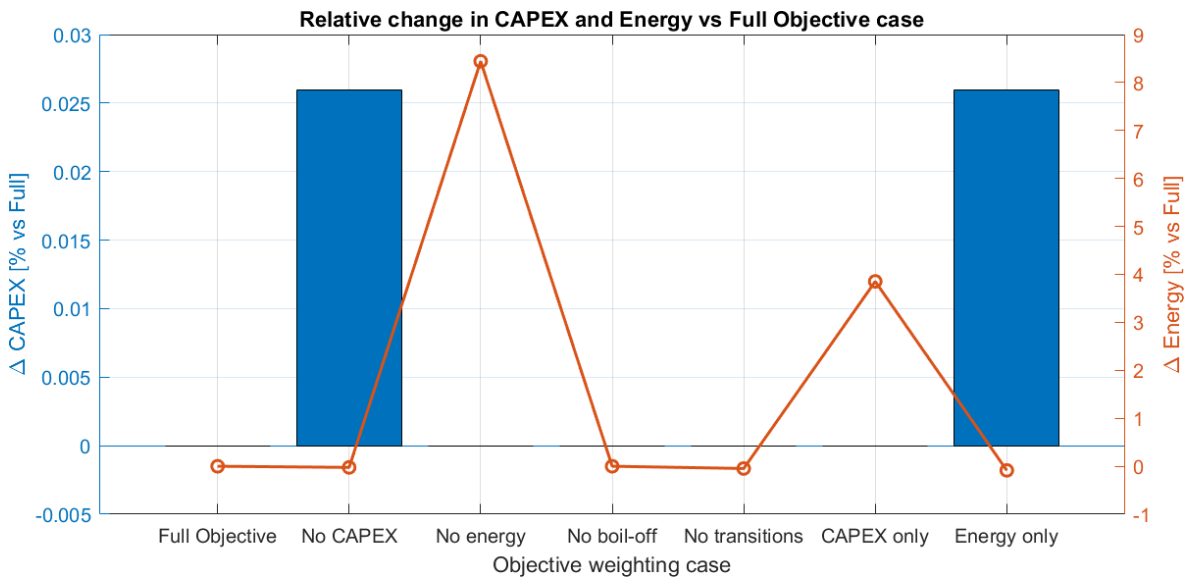


Figure 22. Objective function weight comparison for relative CAPEX and energy demand for case 1.

The sensitivity study is implemented by re-using the same MILP model and constraints and only changing the objective function. The code reconstructs the four objective components as separate expressions for CAPEX, Energy, Boil-off and Transitions. These terms are combined with scalar weights to define generic objectives (e.g. Full [1,1,1,1] or [CAPEX, Energy, Boil-off and Transitions], Energy Only [0,1,0,0]). The results from each optimization case are extracted and normalized with respect to the reference Full [1,1,1,1] case.

The weights for each objective component (i.e., CAPEX, energy consumption, boil-off losses, and transition penalties) were selected heuristically to evaluate their relative influence on the optimization results. The full objective case assigns equal weights of [1,1,1,1], representing equal importance to each objective function. Alternative configurations are created by setting specific

weights to zero, such as [0,1,0,0] for energy-only optimization, to isolate the effect of individual terms. This approach enables a clear interpretation of how prioritizing cost, energy efficiency, or operational penalties impacts the optimal design and dispatch strategy of the station.

Figure 22 shows that across all cases the change in CAPEX is essentially negligible ($<0.03\%$), which means that the optimal equipment sizes (LH₂ tank capacity, GH₂ buffer volume, pump and compressor capacities) are dictated almost entirely by the physical and operational constraints. However, the energy term in the objective function is more sensitive to the weight selection because when the energy term is removed (No energy case), the optimization produces a less efficient schedule, resulting in a daily energy demand increased by about 8% relative to the full objective. A CAPEX-only objective increases energy use by roughly 3.5%, while removing the boil-off penalty has virtually no effect, and removing the transition penalty slightly reduces energy consumption ($\approx 0.5\%$).

4.6.3. With main pump and no main compressor

From Case 1 we noticed that the main compressor is not being used for most of the time and the continuous operation of the main pump is enough to meet most of the station demand. In case 2, we decided to remove the main compressor line completely and added a vent valve in the cryogenic tank to release the vapor mass required to maintain the required pressure constraints. Figure 23(a) shows similar liquid and vapor inventory fluctuations as case 1 with initial increase in liquid mass during low demand and constant liquefier inflow, while the vapor mass remains small. However, whenever thermal boil-off plus liquefier inflow pushes the pressure tank towards the upper limit, during early low demand hours, the optimizer opens the vent valve and removes a small amount of vapor directly to the environment creating rapid pressure drops as shown in Figure 23(b). From a mass-balance perspective, the system now has an explicit loss term, the cumulative vent mass. The vented vapor mass flow rate could be potentially reclaimed and recycled into the system; however, this scenario has not been explored in the current modelling.

Despite the absence of a compressor, Figure 23(c) shows that the 900-bar buffer tank still exhibits a controlled saw-tooth pattern between 82 and 90 MPa. All high-pressure makeup comes from the liquid pump plus booster sequence, and the optimizer chooses similar buffer volume and larger pump capacity with maximum $m\dot{m}_{pp} = 0.12 \text{ kkvv/ss}$ so that, even with only pump-based inflow, the pressure constraints are respected for the entire 24-h horizon.

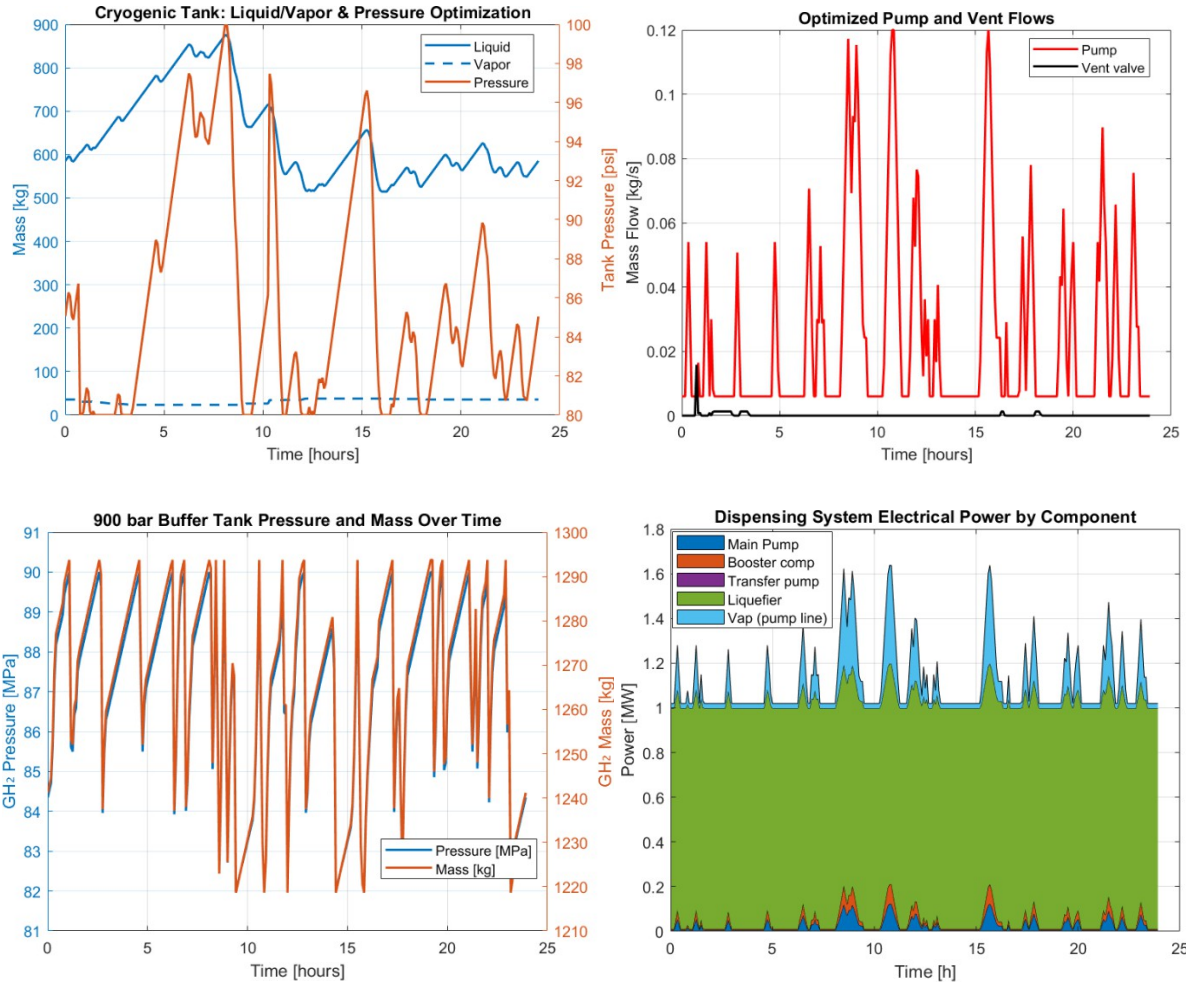


Figure 23. Case 2: (a) Liquid and vapor mass impact on cryogenic tank pressure. (b) Optimized Main pump and vent valve flow rates. (c) 900 bar buffer tank mass and pressure dynamics. (d) Stacked plot showing electrical power demand for each dispensing component.

Figure 23(d) shows the component breakdown electrical energy consumption for case 2 with no main compressor line. As in case 1, the liquefier dominates the dispensing-side power use and appears as a nearly constant base load of about 1 MW over the entire 24 h horizon. The pump-line vaporizer is the second largest contributor, which switches on whenever cryogenic liquid is routed through the main pump and booster to refill the 900-bar buffer after vehicle fills. This is mainly due to the large thermal enthalpy rise and sensible heating for pumping cryogenic liquid at 80-100 psi to ambient temperature of 298 K and 550 bar.

4.6.4. Optimization Results

Key Design Optimization Results

Table 10. Key design optimization results for cases 1 and 2.

Design Parameter	Case 1	Case 2
Liquefier Hydrogen Production	0.02369 kg/s	0.02303 kg/s
Liquefier Unit Size	2.04 TPD	1.98 TPD
Cryogenic tank liquid capacity	950 kg	1200 kg
Main Pump size	324 kg/hour	432 kg/hour
Main Compressor size	72 kg/hour	-
900-bar buffer tank size	30 m ³	27.9 m ³

Table 10 and 11 summarize the key design variables and operational performance results selected by the MILP for both cases. The larger cryogenic liquid tank and pump are needed to supply all vehicle demand via the pump line alone while maintaining the pressure window without the additional compression path. At the same time, the 900-bar buffer volume can be slightly reduced to 27.9 m³ because the pump-only configuration produces a smoother GH₂ inventory profile in the buffer.

Key Operational Optimization Results

Table 11. Key operational optimization results for case 1 and 2.

Operational Parameter	Case 1	Case 2
Main Pump Mass Dispensed (after boil-off)	1865.90 kg	1970.33 kg
Main Comp Mass Dispensed	90.36	0.00 kg
Main Pump Boil off	98.21 kg	103.7 kg
Cryo Tank Boil off vent loss	0 kg	14.6 kg
Net Mass Efficiency (Liquefier production)	95.2%	94.1%
Total Energy Demand	27680.6 kWh/day	26811.4 kWh/day

The mass efficiency of the pump (95%) is reflected in the “pump boil-off” term showing 5% liquid mass being converted into boil off vapor during transfer. Because Case 2 pushes more mass through the pump, the associated boil-off is slightly higher. A key difference is how the tank pressure is controlled: in Case 1, pressure is moderated partly by mass withdrawal through the compressor line, so the optimized solution drives zero venting losses from the cryogenic tank. In Case 2, without the compressor sink, the model instead uses the vent valve; consequently, 14.6 kg/day of hydrogen is vented from the tank to keep the pressure within the allowable window. Despite these additional losses, the total electrical energy demand decreases in Case 2 by around 3.1%. This reduction comes from eliminating the main compressor and its vaporizer energy

consumption. This is a design and operational design tradeoff that needs to be considered; however, the boil-off losses can be reclaimed in the process, this would make case 2 an even better choice over case 1.

The stacked bar chart in Figure 24 shows the breakdown of capital cost for each major component: cryogenic tank, main pump, transfer pump and vaporizers, main compressor, 900 bar buffer tank, booster compressor, and liquefier unit. Case 1 (Pump and Compressor) exhibits a higher overall CAPEX because it includes the main compressor train and its associated vaporizers and auxiliaries. In Case 2 (Pump Only), these items are removed, and although the cryogenic tank and main pump are marginally larger, the net effect is a 7.2% reduction in total station CAPEX.

Overall, optimization indicates that a pump-only architecture with pressure control via venting can achieve comparable hydrogen throughput with slightly lower energy consumption and significantly lower capital cost, at the expense of modestly higher boil off and vented mass.

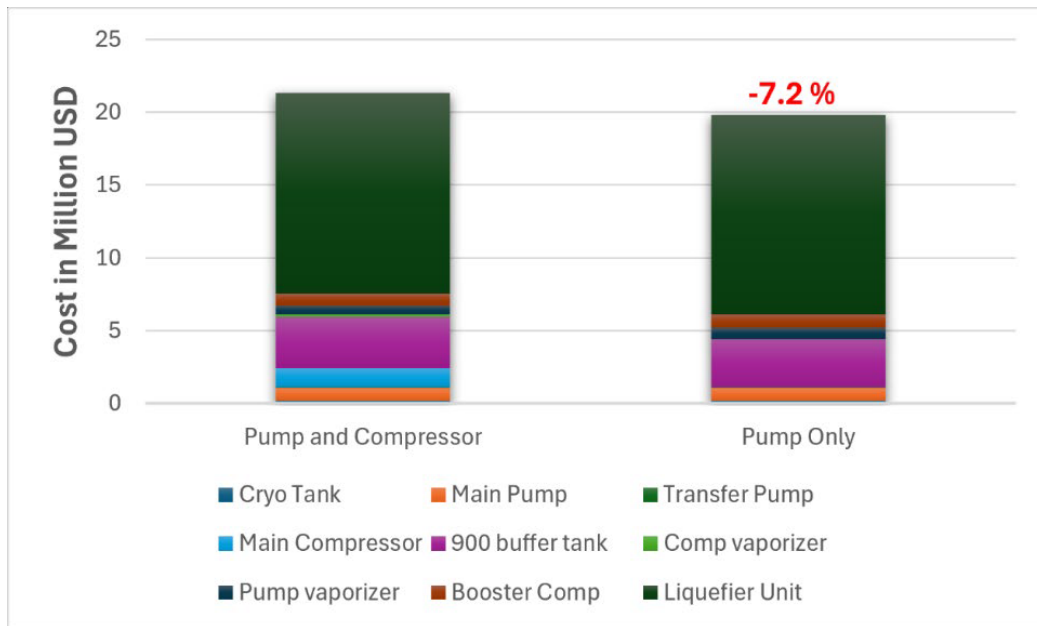


Figure 24. CAPEX contribution of dispensing components and comparison of cases 1 and 2.

4.7. Subsystem 1 and 2 optimization

In this section the electrical energy consumption data from subsystem 1 is gathered and is provided to subsystem 2 to model the complete plant optimization for power generation.

A time-of-use (ToU) electricity tariff was implemented in the model to represent realistic grid prices for Wisconsin. Commercial customer data from We Energies report a standard flat energy charge of 16.659 ¢/kWh, with on peak and off-peak rates of 25.388 and 9.765 ¢/kWh, respectively.[48] The on-peak rate is therefore about 52.4% higher than the flat rate, while the off-peak rate is about 41.4% lower. In parallel, the U.S. Energy Information Administration reports an average industrial electricity price in Wisconsin of 8.54 ¢/kWh for 2024. [49]

In this work, the industrial hydrogen plant is assumed to face the same relative premium and discount over its average industrial price as observed in the commercial ToU structure. Applying a +52.4% multiplier to the industrial average gives an effective on-peak price of 13.01 ¢/kWh, while applying a - 41.4% factor yields an off-peak price of 5.00 ¢/kWh. These two values are then used as the high- and low-price periods in the 24-h dispatch optimization, with the 8.54 ¢/kWh level serving as the reference flat industrial tariff. This approach preserves the relative incentive strength of the utility’s ToU signal while anchoring the absolute prices to industrial-sector averages that are appropriate for a large-scale hydrogen production and refueling facility.

4.7.1 Steady grid with solar

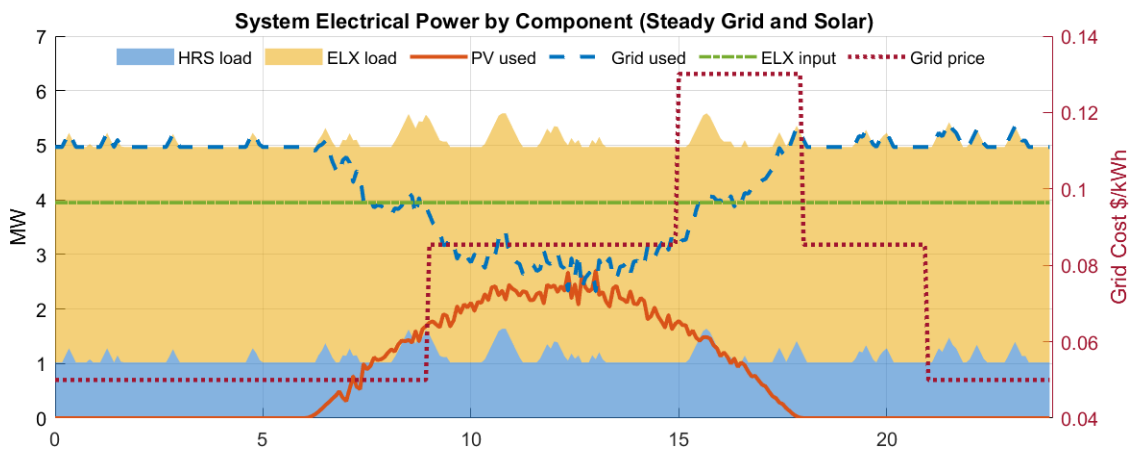


Figure 25. System electrical power supply with intermittent solar supply and steady grid with varying cost.

The power-scheduling result for the steady-grid PV-electrolyzer HRS case is shown in Figure 25. The stacked blue and yellow areas represent the total electrical load, decomposed into the time varying hydrogen refueling station component (liquefier, main pump, booster compressor, and vaporizers) load and the electrolyzer load. The green dashed line corresponds to the PEM electrolyzer power input and is essentially flat at the optimized nameplate capacity ≈ 4 MW.

Because the liquefier inlet mass flow rate is fixed and no 350-bar buffer tank is installed in this case, the electrolyzer must deliver a nearly constant hydrogen production rate, so the optimizer keeps the stack at its design power throughout the day.

The solid orange curve shows the instantaneous solar PV power used by the plant from a fixed PV nameplate of 3 MW. For the winter day with clouds and fast fluctuations considered here, the maximum PV output reaches about 2.66 MW ($\approx 89\%$ of nameplate). In this case, the optimizer uses all available PV at every time step, so there is no PV curtailment. The blue dashed curve is the grid power drawn by the system and simply fills the gap between the total electrical load and the PV production. During nighttime hours, when PV output is zero, the grid supplies almost the entire load (≈ 5 MW). As PV ramps up between roughly 6 h and 18 h, the grid power decreases correspondingly because PV displaces a portion of the demand.

The red dotted line on the secondary axis shows the time-of-use grid price profile, with low-price off-peak periods at night and higher tariffs during the daytime peak window. The reason is that the optimization has essentially no temporal flexibility: PV is modeled as zero-marginal-cost energy and is always used first, the electrolyzer must run at constant power to satisfy the fixed liquefier flow, and the HRS load is determined by the refueling demand. Consequently, the grid simply supplies the residual load at whatever time it occurs, and the plant's instantaneous power profile is dictated by physical and operational constraints rather than by the time-of-use pricing signal.

4.7.2 Grid outage with Solar

Figure 26(a-c) illustrates the optimal operation strategy for the grid-integrated PV–electrolyzer–buffer system under a 1-h grid outage between 13:00–14:00. The electrolyzer nameplate capacity is kept at the optimized value from the steady-grid case (≈ 4 MW), so the system does not rely on oversizing the stack to ride through the disturbance. In Figure 26(a), the green dashed line shows the electrolyzer electrical input. Compared to the no-outage case, the average electrolyzer loading is slightly higher because additional hydrogen must be produced to pre-charge the 350-bar buffer tank. The orange curve is the PV power used by the plant, while the blue dashed curve is the grid power that supplies the shortfall between the total electrical load and the PV production. The shaded band highlights the outage window, during which the grid power drops to zero and the remaining load must be supported entirely by PV and the pre-charged buffer tank.

Figure 26(b) shows the corresponding hydrogen flow rates. For most of the day, the electrolyzer production and the electrolyzer-to-liquefier flow are nearly flat, while a small additional fraction of the electrolyzer output is diverted into the high-pressure buffer tank before the outage. As the outage approaches, the optimizer increases the flow from the electrolyzer to the tank and reduces the tank-to-liquefier contribution, so that the tank inventory is pushed toward its upper bound. During the outage hour, the electrolyzer electrical input dips because only PV power is available; electrolyzer production alone is no longer sufficient to meet the fixed liquefier inlet demand. The

deficit is supplied by withdrawing hydrogen from the buffer tank (tank-to-liquefier flow becomes positive), allowing the liquefier to maintain its target mass flow rate throughout the outage without drawing any power from the grid.

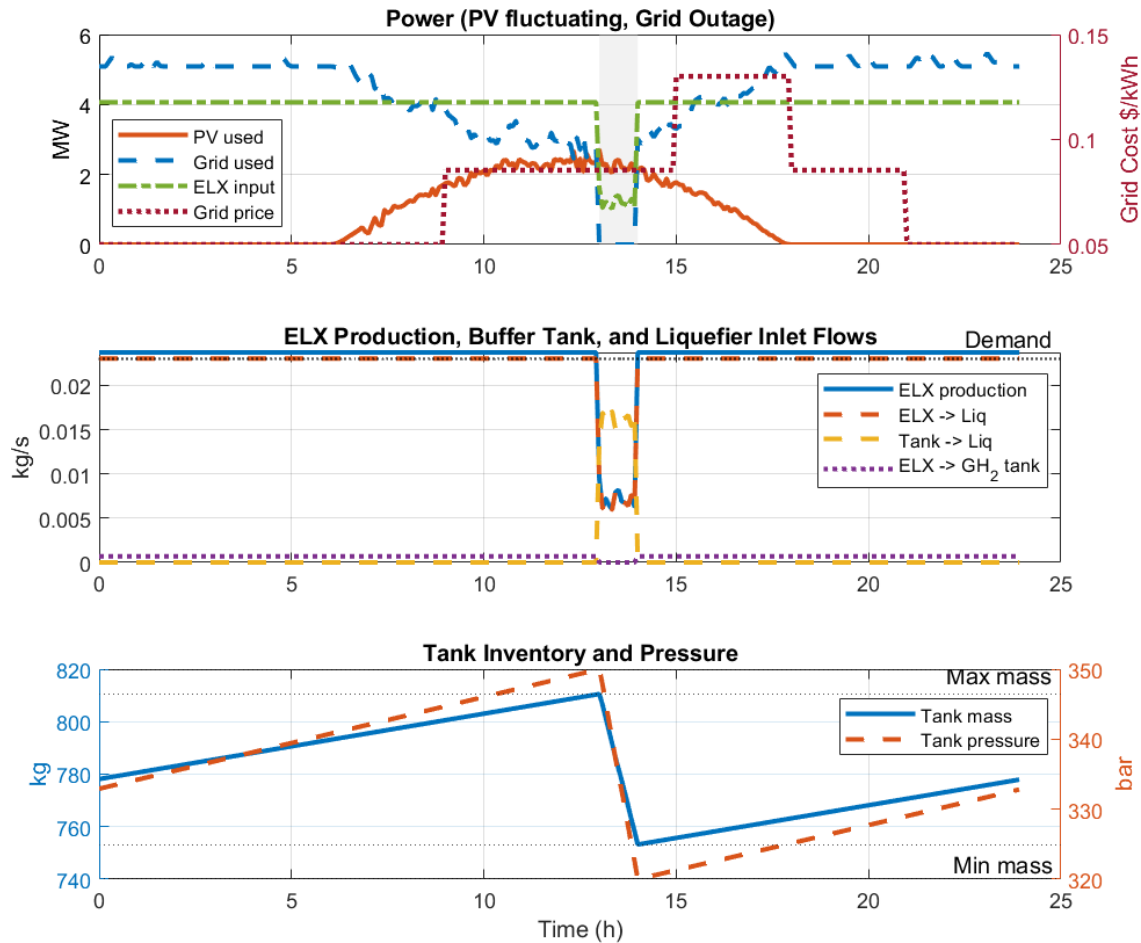


Figure 26. (a) System electrical power supply with intermittent solar supply and 1 hour grid outage with daily varying cost. (b) Electrolyzer mass flow split between 350 bar buffer tank and liquefier. (c) Buffer tank mass and pressure dynamics.

Figure 26(c) shows the resulting evolution of tank inventory and pressure. In the morning and early afternoon, prior to the outage, the tank mass (solid blue line) gradually increases from its initial level (≈ 780 kg) to just above 810 kg, and the corresponding tank pressure (dashed red line) rises but remains within the 320-350 bar operating window. This is the intentional pre-charging phase in anticipation of a possible grid interruption. During the outage, the tank is discharged rapidly to support the liquefier: the mass drops by roughly 60 kg and the pressure falls from near the upper limit toward the lower part of the allowable window. Once grid power is restored after 14:00, the electrolyzer returns to its normal operating level and gradually rebuilds the buffer inventory, so that both tank mass and pressure recover towards their pre-outage values by the end of the 24-h horizon. This behavior demonstrates how a modest sized 350 bar buffer can decouple hydrogen production from short grid disturbances while keeping tank pressure within safe limits.

4.7.3 Optimization Results

Key hydrogen production design optimization results

Table 12. Key hydrogen production design optimization results for steady grid and outage cases.

Parameter	Steady Grid	Grid Outage
Electrolyzer Capacity	3.948 MW	4.043 MW
Electrolyzer Flow rate	0.02303	0.0237 kg/s
Electrolyzer Capacity Factor	100%	97.1%
350-bar Buffer Tank Size	0.00 m ³	34.75 m ³
350-bar Compressor Size	0.00 kg/hour	2.52 kg/hour

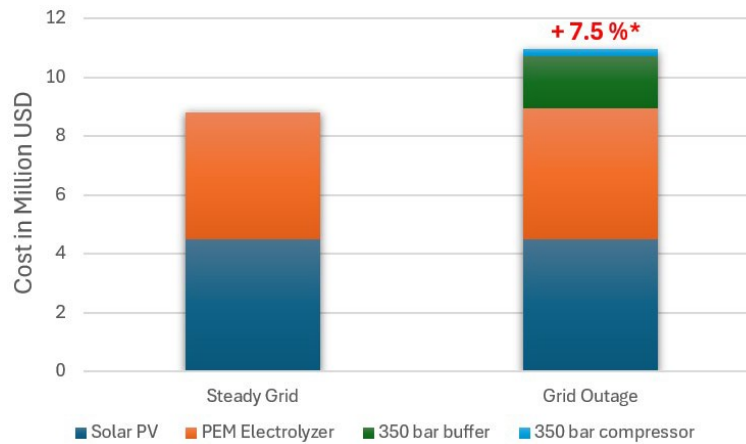


Figure 27. Total Plant CAPEX comparison for (pump-only case) for steady grid and grid outage cases.
*Represents total CAPEX including dispensing subsystem components.

4.8. Economic Analysis

In this thesis, the economic performance of the proposed hydrogen refueling station is evaluated using the Levelized Cost of Hydrogen (LCOH), which represents the long-run average cost of producing and delivering one kilogram of hydrogen over the project lifetime. LCOH is calculated via a discounted cash-flow framework consistent with DOE H2A and related techno-economic studies, in which the upfront capital investment (CAPEX) for the electrolyzer, liquefaction, storage, compression and dispensing equipment is annualized using a capital recovery factor, and then combined with annual operating expenditures (OPEX), dominated by electricity costs but also including non-electric O&M. This total annualized cost is divided by the annual hydrogen dispensed at the station to obtain a cost in \$/kg hydrogen. [50]

The economic assessment of the base case 2 with main pump only and no main compressor is summarized in Figure 27 and Table 12. The LCOH is calculated with a discounted-cash flow approach and capital recovery factor (CRF). For this study, the discount rate is 8% and plant life is considered to be 20 years, which gives $CCCCC \approx 0.102$. The LCOH is then obtained by annualizing the total capital investment and adding the annual operating cost, divided by the annual hydrogen production. Here CAPEX is the total capital cost of the HRS, $CC_{LLee,DDDDyy}$ is the daily electricity cost, the factor 1.20 accounts for additional O&M costs taken as 20% of the electricity cost, and $mm_{HH2,DDDDyy}$ is the daily hydrogen dispensed. The direct installed CAPEX of the HRS (electrolyzer, Solar PV, liquefier, storage tanks, pumps, compressors and vaporizers) is 28.61 million USD. An additional 20% indirect CAPEX (5.72 million USD) is included to represent engineering, controls, electricals, permitting, contingency and other owners' costs, giving a total CAPEX of 34.33 million USD. The daily OPEX consists of 7,337 USD/day for grid electricity and 1,467 USD/day for non-electric O&M (20% of the electricity cost), for a total of 8,804 USD/day. With a hydrogen throughput of 2,000 kg/day (730,000 kg/yr), the resulting base-case levelized cost of hydrogen is 9.34 \$/kg. The donut chart in Figure 28 illustrates the breakdown of this LCOH into capital and operating contributions. Annualized CAPEX contributes 4.87 \$/kg (approximately 52% of the LCOH), while OPEX (electricity plus O&M) contributes 4.47 \$/kg (approximately 48%). This indicates that, for the chosen design and financial assumptions, the cost of hydrogen at the nozzle is almost split between recovering the upfront investment and covering the ongoing operating expenses.

$$CCCCC = \frac{rr(1 + rr)^{NN}}{(1 + rr)^{NN} - 1}$$

$$LLCLLLL = \frac{CCAAPPECC \cdot CCCCC + 1.20 \cdot CC_{LLee,DDDDyy} \cdot 365}{mm_{DLLLLDDDDDD} \cdot 365}$$

Table 13. Economic parameters considered for the LCOH calculations.

Economic Parameter	Value
Direct Installed CAPEX HRS System	\$ 28.61 million
Indirect CAPEX	\$ 5.72 million
Total CAPEX	34.33 million
OPEX Grid Electricity cost	\$ 7,337 /day
OPEX O&M	1467 \$/day
Total OPEX	8804 \$/day
Plant Life, NN	20 years
Discount Rate, rr	8 %
CRF	0.102
Total Mass Dispensed to Vehicles	1968.62 kg/day

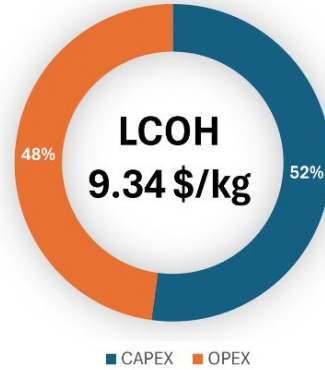


Figure 28. Levelized cost of hydrogen (LCOH) for steady grid case and contribution of CAPEX and OPEX.

Recent DOE and NREL [51] analyses treat the levelized cost of hydrogen (LCOH) as a full (plant to nozzle) metric, including production, liquefaction or compression, delivery, and station CAPEX/OPEX, using discounted-cash-flow methods implemented in HDSAM. NREL's 2024 heavy-duty station study finds that for 2 metric TPD on-site gaseous production stations with 700-bar dispensing, the system LCOH in 2030 spans 6.1-12.6 \$/kg H₂, depending on utilization rate. DOE Program Records for delivery and dispensing alone report 12-13 \$/kg in 2017 with potential to reach 5 \$/kg in a 2025 R&D case, excluding production at stations supplied by liquid hydrogen tank trucks. [52]

When compared against these benchmarks, the present self-sustainable on-site liquid production, storage, and dispensing system, which delivers an LCOH of 9.34 \$/kg H₂ at 2 TPD, appears technically and economically viable within the context of near-term heavy-duty hydrogen infrastructure. The modeled LCOH falls inside the NREL cost range for similar-scale stations and is broadly consistent with DOE projections once both production and transportation/dispensing costs are included, while also eliminating reliance on external liquid hydrogen deliveries. This integrated architecture reduces exposure to tanker logistics and delivered-LH₂ price volatility, improves operational resilience, and creates a pathway to further cost reduction as electrolyzer and liquefier CAPEX decline, utilization increases, and low-carbon electricity becomes cheaper. As such, the base-case LCOH should be interpreted as a realistic near-term value for a first-generation, self-sufficient liquid hydrogen truck refueling hub, with clear upside potential through technology learning, higher station throughput, and supportive policy incentives.

To provide an intuitive metric for comparing hydrogen fuel costs with conventional energy carriers, the Levelized Cost of Hydrogen (LCOH) can be expressed in terms of cost per unit energy and cost per mile for representative heavy-duty fuel cell truck. The lower heating value (LHV) of hydrogen is approximately 120,000 kJ/kg (33.3 kWh/kg) as noted in Section 1.3. Using the optimized station LCOH of \$9.34/kg, the cost per unit energy is around 7.78×10^{-5} \$/kJ.

For the Hyundai XCIENT truck, which stores 68.6 kg of hydrogen at 700 bar and achieves an all electric range of approximately 450 miles (Section 1.4), the specific range is around 6.56 miles/kg.

Combining this with LCOH, cost comes to 1.42 \$/mile. At \$1.42 per mile, hydrogen fuel for heavy-duty trucks is currently higher than diesel on a pure fuel-cost basis but offers zero tailpipe emissions and rapid refueling advantages. These figures highlight the importance of reducing both liquefaction energy intensity and electrolyzer CAPEX and OPEX to make hydrogen competitive in long-haul freight applications.

Chapter 5. Conclusions

This thesis developed and analyzed a techno-economic optimization framework for a fully integrated liquid hydrogen refueling station (HRS) designed for heavy-duty transportation applications. The proposed architecture combines on-site renewable hydrogen production via PEM electrolysis, liquefaction, cryogenic storage, and 700-bar dispensing into a unified system optimized for both technical performance and economic viability.

Key findings from this research are summarized below:

1. *Integrated System Feasibility*

The study demonstrates that a self-sustaining HRS capable of producing, storing, and dispensing liquid hydrogen on-site is technically feasible and can meet the stringent requirements of heavy-duty fuel cell electric vehicles (FCEVs). By co-locating electrolyzer, liquefier, cryogenic storage, and dispensing subsystems, the design eliminates reliance on external liquid hydrogen deliveries, reducing logistical complexity and exposure to supply-chain disruptions.

2. *Optimization Insights*

The mixed-integer linear programming (MILP) model successfully identified optimal sizing and scheduling strategies for major components under realistic operational constraints. Results indicate that a pump-only dispensing configuration, supported by controlled venting for pressure management, achieves comparable hydrogen throughput with 7.2% lower CAPEX and 3.1% lower energy consumption compared to a pump plus compressor architecture. This trade-off highlights the importance of balancing equipment complexity, energy efficiency, and boil-off losses in station design.

3. *Energy and Cost Performance*

After PEM electrolyzer, the liquefaction remains the dominant energy consumer, accounting for over 85% of dispensing-side power demand, underscoring the need for continued improvements in liquefier efficiency. The optimized station delivers a Levelized Cost of Hydrogen (LCOH) of \$9.34/kg at a throughput of 2 metric tons per day, which falls within the range projected by DOE and NREL for near-term heavy-duty hydrogen infrastructure. Approximately 52% of LCOH is attributed to capital recovery and 48% to operating costs, indicating that both CAPEX reduction and low-cost electricity are critical for competitiveness.

4. *Capacity Factor Performance*

The optimized electrolyzer design operates at a near-constant load to meet liquefier demand, achieving a capacity factor of 97.1% with grid outage case, which is critical for reducing hydrogen production cost and improving utilization. Liquefier is modeled as a base load unit with fixed flow, the liquefier runs continuously at its design point, resulting in a capacity factor of ~100%. The pump operates intermittently but with extended ON

periods to minimize boil-off losses and avoid frequent start-stop cycles. Across the 24-hour horizon, the pump achieves an effective lower capacity factor, depending on demand peaks and optimization constraints. The next step for the future work is to minimize the capacity factor of these components and add them to the objective function.

5. *Operational Resilience*

The integrated PV-electrolyzer-buffer system effectively mitigates short-term grid outages through strategic pre-charging of the 350-bar buffer tank, ensuring uninterrupted liquefier operation during disturbances. This capability enhances station reliability and supports continuous heavy-duty vehicle refueling even under variable renewable generation and grid constraints.

6. Future Work

6.1 Variable Vehicle SOC modelling

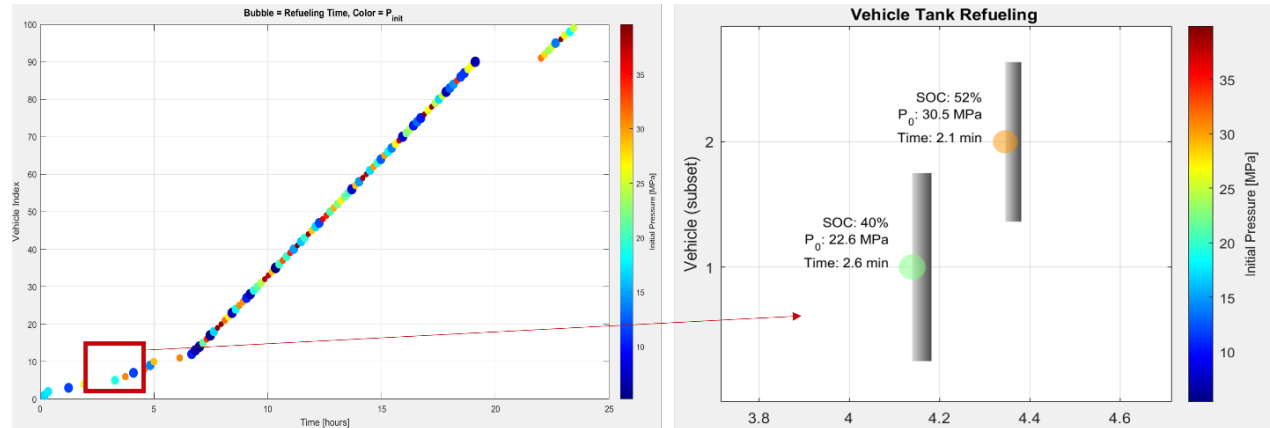


Figure 29. Variable initial vehicle tank pressure and SOC modelling.

In the present work, all refueling events are initialized from the same vehicle tank state-of-charge (SOC) and corresponding initial pressure. This deterministic assumption simplifies the analysis and allows clear comparison between operating cases, but it does not fully represent real-world station usage, where vehicles arrive with a broad distribution of initial SOC. As future work, the refueling demand model can be extended to a stochastic vehicle arrival and SOC framework, in which each vehicle arrival is sampled from probability distributions for arrival time, initial SOC (or tank pressure), and tank size as shown in Figure 29. These distributions data will be then coupled to the existing H2Fills to generate time-varying mass, pressure, and temperature profiles for each individual fill.

6.2 Multi-stage Buffer storage

A second important extension is the introduction of a multi-stage buffer storage system with low, mid, and high-pressure vessels upstream of the dispenser. Instead of relying on a single high-pressure buffer and frequent compressor cycling, the station could dynamically route hydrogen between multiple pressure levels based on real-time demand, tank SOC, and electricity price. Such a cascade storage configuration would allow more of the refueling work to be supplied by pressure equalization from higher-pressure buffers, reducing the incremental work required from the compressor during each fill. By co-optimizing the capacities and operating policies of the low/mid/high-pressure buffers with the stochastic demand model, future studies can quantify potential reductions in compressor power, start-stop cycling, and overall energy cost, while still meeting heavy-duty FCEV refueling requirements and maintaining fast-fill performance.

6.3 Data driven Convex Optimization- Cryogenic tank

In this thesis, the MILP uses a single linear mapping between liquid mass, vapor mass and tank pressure to enforce the 80-100 psi operating window. While this gives clear insights, it cannot capture the cross-dependence of tank pressure on both liquid inventory, pump outflow, and liquefier inlet. As a result, feasibility and control decisions around varying pump mass flow rate operation can be conservative. The next step is to replace this surrogate with a data-driven 2-D convex interpolation (SOS2) built from thermodynamic correlation table 14 that are precomputed over a grid of liquid inventory and pump outflow. At each grid node, the thermodynamic model would provide MM_{VDDpp} $ccnndd$ PP_{tank} and the MILP would reconstruct the operating point using convex weights that sum to one and are SOS2 restricted along each axis so only neighboring breakpoints are blended. This preserves linearity while allowing continuous set-points for flow and mass and reduces infeasibility near partial-load boundaries, yielding a smoother and more realistic mapping of $PP_{tank}(MM_{EELLLL}, MM_{VDDpp}, \dot{m}_{pp}, \cdot)$.

A generic equation is shown below to compute $dd(xx)$ as a weighted average of prefit functions $oo_{LL}(xx)$ where λ_{LL} are non-negative and sum to 1 (a convex combo). The SOS2 condition means only two adjacent λ_{LL} can be non-zero and we interpolate between those neighbors, i.e., piecewise linear model.

$$dd(xx) = \sum_{NN} \lambda_{LL} oo_{LL}(xx), \quad \sum_{NN} \lambda_{LL} = 1, \lambda_{LL} \geq 0, \lambda \in SOS2$$

Table 14. Multilinear regression relations for vapor mass and pressure with change in liquid mass and inlet/outlet flow rates.

Case	Inlet (kg/s)	Outlet (kg/s)	Vapor mass (MM_{VVVVV})	Cryogenic Tank Pressure (PP_{tank})
1	0.02	0.01	$0.012417 * MM_{EELLLL} + 55.597257$	$18.322755 + -0.040887 * MM_{VDDpp} + 0.321467 * MM_{EELLLL}$
2	0.025	0.01	$-0.013059 * MM_{EELLLL} + 60.505231$	$-31.286090 + 0.851696 * MM_{VDDpp} + 0.301391 * MM_{EELLLL}$
3	0.03	0.01	$-0.021906 * MM_{EELLLL} + 62.307581$	$31.876149 + -0.192740 * MM_{VDDpp} + 0.282980 * MM_{EELLLL}$
4	0.02	0.025	$-0.155939 * MM_{EELLLL} + 78.635715$	$41.120235 + 0.533510 * MM_{VDDpp} - 0.039365 * MM_{EELLLL}$
5	0.025	0.025	$-1.000000 * MM_{EELLLL} + 200.000000$	$0.000000 + 1.695566 * MM_{VDDpp} - 0.217044 * MM_{EELLLL}$
6	0.03	0.025	$0.160418 * MM_{EELLLL} + 34.485260$	$-48.171847 + 0.709382 * MM_{VDDpp} + 0.503730 * MM_{EELLLL}$
7	0.02	0.05	$1.000000 * MM_{EELLLL} - 0.000000$	$58.074926 + 0.059417 * MM_{VDDpp} + 0.000000 * MM_{EELLLL}$
8	0.025	0.05	$-0.049258 * MM_{EELLLL} + 64.606164$	$-39.518011 + 1.547402 * MM_{VDDpp} + 0.118230 * MM_{EELLLL}$
9	0.03	0.05	$-0.066708 * MM_{EELLLL} + 66.955540$	$-20.283639 + 1.251149 * MM_{VDDpp} + 0.105885 * MM_{EELLLL}$
10	0.025	0	$-0.032761 * MM_{EELLLL} + 63.663005$	$99.473158 + -1.271477 * MM_{VDDpp} + 0.231324 * MM_{EELLLL}$
11	0.025	0.03	$-0.175450 * MM_{EELLLL} + 81.674683$	$44.039056 + 0.537317 * MM_{VDDpp} - 0.060170 * MM_{EELLLL}$
12	0.025	0.09	$-0.024918 * MM_{EELLLL} + 49.989883$	$-84.105925 + 2.549348 * MM_{VDDpp} + 0.113087 * MM_{EELLLL}$

References

- [1] “REN21. 2023. Renewables 2023 Global Status Report Collection, Renewables in Energy Demand.”
- [2] “Climate Action Tracker, Decarbonising light-duty vehicle road transport,” Oct. 2024.
- [3] “Net Zero by 2050 – Analysis,” IEA. Accessed: Dec. 02, 2025. [Online]. Available: <https://www.iea.org/reports/net-zero-by-2050>
- [4] “Decarbonising hard-to-abate sectors with renewables,” IRENA, 2024.
- [5] “A Report on actions for medium and heavy-duty vehicle energy and emissions innovation,” 2024.
- [6] S. Z. A. Ghafri *et al.*, “Hydrogen liquefaction: a review of the fundamental physics, engineering practice and future opportunities,” *Energy Environ. Sci.*, vol. 15, no. 7, pp. 2690–2731, July 2022, doi: 10.1039/D2EE00099G.
- [7] T. Zhang, J. Uratani, Y. Huang, L. Xu, S. Griffiths, and Y. Ding, “Hydrogen liquefaction and storage: Recent progress and perspectives,” *Renewable and Sustainable Energy Reviews*, vol. 176, p. 113204, Apr. 2023, doi: 10.1016/j.rser.2023.113204.
- [8] “Oil demand growing at a slower pace as post-Covid rebound runs its course – Analysis,” IEA. [Online]. Available: <https://www.iea.org/commentaries/oil-demand-growing-at-a-slower-pace-as-post-covid-rebound-runs-its-course>
- [9] L. Zhao and J. Brouwer, “Dynamic operation and feasibility study of a self-sustainable hydrogen fueling station using renewable energy sources,” *International Journal of Hydrogen Energy*, vol. 40, no. 10, pp. 3822–3837, Mar. 2015, doi: 10.1016/j.ijhydene.2015.01.044.
- [10] “Hyundai Xcient Fuel Cell Truck.” [Online]. Available: ecv.hyundai.com
- [11] “Tesla Electric Semi Truck.” [Online]. Available: www.tesla.com/semi
- [12] S. O. Showers, A. K. Raji, S. O. Showers, and A. K. Raji, “State-of-the-art review of fuel cell hybrid electric vehicle energy management systems,” *AIMSE*, vol. 10, no. 3, pp. 458–485, 2022, doi: 10.3934/energy.2022023.
- [13] “Hydrogen Refueling Process: Theory, Modeling, and In-Force Applications.” [Online]. Available: <https://www.mdpi.com/1996-1073/16/6/2890>

- [14] A. M. Elberry, J. Thakur, and J. Veysey, "Seasonal hydrogen storage for sustainable renewable energy integration in the electricity sector: A case study of Finland," *Journal of Energy Storage*, vol. 44, p. 103474, Dec. 2021, doi: 10.1016/j.est.2021.103474.
- [15] J. Li *et al.*, "Liquid pump-enabled hydrogen refueling system for heavy duty fuel cell vehicles: Pump performance and J2601-compliant fills with precooling," *International Journal of Hydrogen Energy*, vol. 46, no. 42, pp. 22018–22029, June 2021, doi: 10.1016/j.ijhydene.2021.04.043.
- [16] K. Reddi, A. Elgowainy, N. Rustagi, and E. Gupta, "Impact of hydrogen refueling configurations and market parameters on the refueling cost of hydrogen," *International Journal of Hydrogen Energy*, vol. 42, no. 34, pp. 21855–21865, Aug. 2017, doi: 10.1016/j.ijhydene.2017.05.122.
- [17] "Global Hydrogen Review," IEA. [Online]. Available: <https://www.iea.org/energy-system/low-emission-fuels/hydrogen>
- [18] "Deployment of Fuel Cell Vehicles and Hydrogen Refueling Station Infrastructure: A Global Overview and Perspectives." Available: <https://www.mdpi.com/1996-1073/15/14/4975>
- [19] Anonymous, "Over 1,000 Hydrogen Refuelling Stations Worldwide in 2024 - Fuelcellworks." [Online]. Available: <https://fuelcellworks.com/2025/02/12/h2/milestone-reached-over-1-000-hydrogen-refuelling-stations-in-operation-worldwide-in-2024>
- [20] I. A. Hassan, H. S. Ramadan, M. A. Saleh, and D. Hissel, "Hydrogen storage technologies for stationary and mobile applications: Review, analysis and perspectives," *Renewable and Sustainable Energy Reviews*, vol. 149, p. 111311, Oct. 2021, doi: 10.1016/j.rser.2021.111311.
- [21] "The prospects for hydrogen as an energy carrier: an overview of hydrogen energy and hydrogen energy systems | Energy, Ecology and Environment." Available: <https://link.springer.com/article/10.1007/s40974-016-0005-z>
- [22] M. Granovskii, I. Dincer, and M. A. Rosen, "Greenhouse gas emissions reduction by use of wind and solar energies for hydrogen and electricity production: Economic factors," *International Journal of Hydrogen Energy*, vol. 32, no. 8, pp. 927–931, June 2007, doi: 10.1016/j.ijhydene.2006.09.029.
- [23] "Cost Projections for Green Hydrogen Production Using Different Electrolyser Technologies in China | IEEE Conference Publication | IEEE Xplore." [Online]. Available: <https://ieeexplore.ieee.org/document/11116666/>

- [24] S. Krishnan *et al.*, “Present and future cost of alkaline and PEM electrolyser stacks,” *International Journal of Hydrogen Energy*, vol. 48, no. 83, pp. 32313–32330, Oct. 2023, doi: 10.1016/j.ijhydene.2023.05.031.
- [25] M. Benbouzid, L. Bouhachlaf, N. Labjar, M. Dalimi, and S. El Hajjaji, “Global Journey of Green Hydrogen,” in *Green Hydrogen*, John Wiley & Sons, Ltd, 2025, pp. 337–371. doi: 10.1002/9781394356706.ch13.
- [26] Y. Pang, L. Pan, J. Zhang, J. Chen, Y. Dong, and H. Sun, “Integrated sizing and scheduling of an off-grid integrated energy system for an isolated renewable energy hydrogen refueling station,” *Applied Energy*, vol. 323, p. 119573, Oct. 2022, doi: 10.1016/j.apenergy.2022.119573.
- [27] A. M. Ghaithan, M. Kondkari, A. Mohammed, and A. M. Attia, “Optimal design of concentrated solar power-based hydrogen refueling station: Mixed integer linear programming approach,” *International Journal of Hydrogen Energy*, vol. 86, pp. 703–718, Oct. 2024, doi: 10.1016/j.ijhydene.2024.08.451.
- [28] M. R. Shaner, H. A. Atwater, N. S. Lewis, and E. W. McFarland, “A comparative technoeconomic analysis of renewable hydrogen production using solar energy,” *Energy Environ. Sci.*, vol. 9, no. 7, pp. 2354–2371, 2016, doi: 10.1039/c5ee02573g.
- [29] “Tracking Clean Energy Progress 2023 – Analysis,” IEA. Accessed: Dec. 02, 2025. [Online]. Available: <https://www.iea.org/reports/tracking-clean-energy-progress-2023>
- [30] “Hydrogen liquefaction: a review of the fundamental physics, engineering practice and future opportunities - Energy & Environmental Science (RSC Publishing).” [Online]. Available: <https://pubs.rsc.org/en/content/articlelanding/2022/ee/d2ee00099g>
- [31] “PEM Electrolysis System - MATLAB & Simulink.” Accessed: Dec. 10, 2025. [Online]. Available: <https://www.mathworks.com/help/simscape/ug/pem-electrolysis-system.html>
- [32] V. V. Osipov, M. J. Daigle, C. B. Muratov, M. Foygel, V. N. Smelyanskiy, and M. D. Watson, “Dynamical Model of Rocket Propellant Loading with Liquid Hydrogen,” *Journal of Spacecraft and Rockets*, May 2012, doi: 10.2514/1.52587.
- [33] “Model-based diagnostics for propellant loading systems | IEEE Conference Publication | IEEE Xplore.” [Online]. Available: <https://ieeexplore.ieee.org/document/5747596/>
- [34] G. Petitpas, “Simulation of boil-off losses during transfer at a LH2 based hydrogen refueling station,” *International Journal of Hydrogen Energy*, vol. 43, no. 46, pp. 21451–21463, Nov. 2018, doi: 10.1016/j.ijhydene.2018.09.132.

- [35] G. Qiu *et al.*, “Numerical study on the dynamic process of reciprocating liquid hydrogen pumps for hydrogen refueling stations,” *Energy*, vol. 281, p. 128303, Oct. 2023, doi: 10.1016/j.energy.2023.128303.
- [36] G. Qiu, K. Wang, S. Zhu, and L. Qiu, “Hydrogen refueling station synergistically driven by liquid hydrogen pump and thermal compression,” *International Journal of Hydrogen Energy*, vol. 56, pp. 441–451, Feb. 2024, doi: 10.1016/j.ijhydene.2023.12.108.
- [37] N. C. E. & I. G. Group, “Cryogenic pumps,” Nikkiso Clean Energy & Industrial Gases Group. [Online]. Available: <https://www.nikkisoceig.com/products/cryogenic-pumps>
- [38] G. Petitpas, “Boil-off losses along LH2 pathway,” Lawrence Livermore National Laboratory, LLNL-TR-750685, 2018.
- [39] G. Parks, “Hydrogen Station Compression, Storage, and Dispensing Technical Status and Costs,” National Renewable Energy Laboratory, NREL/BK-6A10-58564, 2014.
- [40] “Demonstration of innovative solutions for high-capacity, reliable, flexible, and sustainable hydrogen compression technologies in commercial applications,” Horizon-europe.gouv.fr. Available: <https://www.horizon-europe.gouv.fr/demonstration-innovative-solutions-high-capacity-reliable-flexible-and-sustainable-hydrogen-36558>
- [41] A. Bauer, T. Mayer, M. Gierse, M. A. Guerrero Morales, and J. Wind, “Energetic evaluation of hydrogen refueling stations with liquid or gaseous stored hydrogen,” *International Journal of Hydrogen Energy*, vol. 44, no. 13, pp. 6795–6812, Mar. 2019, doi: 10.1016/j.ijhydene.2019.01.087.
- [42] “Hydrogen Delivery Scenario Analysis Model.” [Online]. Available: <https://hdsam.es.anl.gov/index.php?content=hdsam>
- [43] “U.S. construction costs rose slightly for solar and wind, dropped for natural gas in 2022 - U.S. Energy Information Administration (EIA).” [Online]. Available: <https://www.eia.gov/todayinenergy/detail.php?id=63485>
- [44] H2-View, “ITM unveils 5MW PEM electrolyser plant with a price tag of £4.35m,” H2 View. Available: <https://www.h2-view.com/story/itm-unveils-5mw-pem-electrolyser-plant-with-a-price-tag-of-4-35m/2109922.article/>
- [45] “The Plug EX-425D,” Plug Power Inc.
- [46] “H2FillS: Hydrogen Filling Simulation | Hydrogen and Fuel Cells | NREL.” [Online]. Available: <https://www.nrel.gov/hydrogen/h2fills>

- [47] C. Gupta, S. Kumar, S. Poonia, and K. Pareek, "Refueling analysis of Type IV composite tank as per SAEJ2601 with refueling station configuration," *International Journal of Hydrogen Energy*, vol. 78, pp. 970–983, Aug. 2024, doi: 10.1016/j.ijhydene.2024.06.300.
- [48] "Wisconsin Time-of-Use | We Energies." [Online]. Available: <https://www.we-energies.com/services/time-of-use-wi>
- [49] "SAS Output." [Online]. Available: https://www.eia.gov/electricity/annual/html/epa_02_10.html
- [50] S. Devkota *et al.*, "Techno-economic and environmental assessment of hydrogen production through ammonia decomposition," *Applied Energy*, vol. 358, p. 122605, Mar. 2024, doi: 10.1016/j.apenergy.2023.122605.
- [51] J. Bracci, "Levelized Cost of Dispensed Hydrogen for Heavy-Duty Vehicles," National Renewable Energy Laboratory, NREL/TP-5400-88818, Mar. 2024.
- [52] N. Rustagi, "Current Status of Hydrogen Delivery and Dispensing Costs and Pathways to Future Cost Reductions," DOE Hydrogen and Fuel Cells Program Record, 18003, 2018.
- [53] "CEPCI." [Online]. Available: <https://www.training.itservices.manchester.ac.uk/public/gced/CEPCI.html?reactors/CEPCI/index.html>
- [54] K. Reddi, A. Elgowainy, N. Rustagi, and E. Gupta, "Impact of hydrogen SAE J2601 fueling methods on fueling time of light-duty fuel cell electric vehicles," *International Journal of Hydrogen Energy*, vol. 42, no. 26, pp. 16675–16685, June 2017, doi: 10.1016/j.ijhydene.2017.04.233.

Appendix

Appendix A: Chemical Engineering Plant Cost Index (CEPCI) Trend

Figure 30 shows the long-term evolution of the Chemical Engineering Plant Cost Index (CEPCI), a widely used metric for adjusting historical equipment and plant capital costs to present-day values. [53] In this thesis, CEPCI-based cost escalation is applied to normalize historical capital-cost correlations from literature (e.g., 2007, 2010, 2013, 2014 datasets) to a consistent 2024 cost basis for comparison and optimization of hydrogen refueling station components.

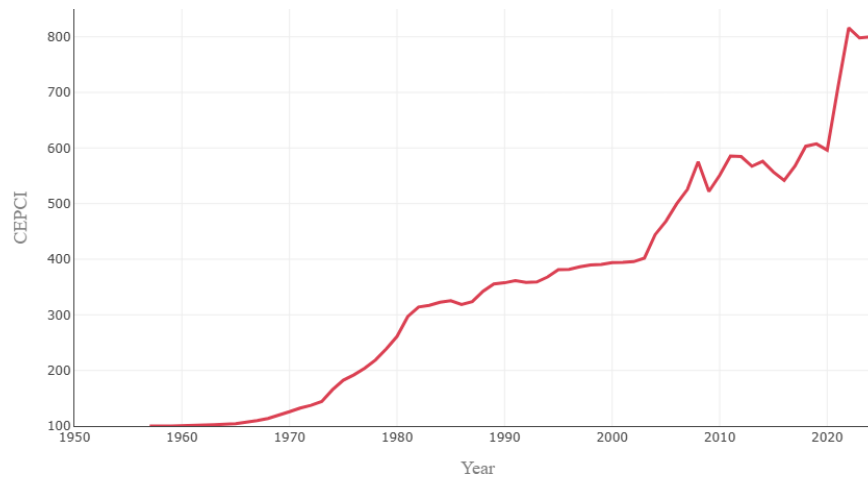


Figure 30. CEPCI values change with time.

Appendix B: Lookup table for 700 bar vehicles refueling T40 HRS

		Top-Off Fueling Parameters				Target Pressure, P _{target} [MPa]														
		APRR [MPa/min]	Target Pressure P _{target} [MPa]	Target Pressure Top-Off [MPa]	Top-Off APRR [MPa/min]	Initial Tank Pressure, P ₀ [MPa]														
						0.5-5 (no interpolation)														
						0.5	2	5	10	15	20	30	40	50	60	70	>70			
Ambient Temperature, T _{amb} [°C]	>50	No Fueling				No Fueling														
	50	5.1	78.2	87.5	2.6	80.8	85.7	86.8	86.5	85.8	85.0	84.0	82.7	81.1	No Fueling					
	45	8.1	76.3	87.5	4.0	81.1	86.9	86.6	86.2	85.3	84.3	83.0	81.6	79.7	No Fueling					
	40	11.5	73.2	87.5	5.4	81.1	86.9	86.4	85.9	84.7	83.5	82.0	80.3	78.3	No Fueling					
	35	12.4	72.9	87.5	5.6	Top-Off Fueling	81.2	86.9	86.4	85.9	84.7	83.4	81.9	80.2	78.2	No Fueling				
	30	15.3	70.6	87.5	6.6		81.0	86.8	86.3	85.6	84.3	82.8	81.2	79.4	77.2	No Fueling				
	25	18.5	69.0	87.4	7.2	81.0	86.8	86.1	85.4	83.8	82.2	80.4	78.5	76.1	No Fueling					
	20	21.8	67.9	87.4	7.6	81.2	86.8	85.9	85.1	83.3	81.5	79.6	77.5	75.1	No Fueling					
	10	28.0	66.3	87.4	9.0	81.2	86.8	85.7	84.7	82.6	80.5	78.3	76.1	73.4	No Fueling					
	0	28.5	No Top-Off Fueling				78.4	84.6	86.8	85.6	84.4	83.1	80.6	78.1	75.6	73.1	No Fueling			
	-10	28.5	No Top-Off Fueling				82.2	87.1	86.4	85.2	84.0	82.8	80.4	77.9	75.4	72.9	No Fueling			
	-20	28.5	No Top-Off Fueling				86.0	86.8	86.1	84.9	83.7	82.4	80.0	77.6	75.1	72.7	No Fueling			
	-30	28.5	No Top-Off Fueling				86.8	86.5	85.7	84.5	83.3	82.1	79.6	77.2	74.9	72.5	No Fueling			
-40	28.5	No Top-Off Fueling				86.5	86.2	85.4	84.2	83.0	81.8	79.3	77.0	74.6	72.3	No Fueling				
<-40		No Fueling																		

Figure 31. SAE protocol lookup table for vehicle refueling pressure ramp rate. [54]